

SEARCH FOR LONG-DURATION TRANSIENT GRAVITATIONAL WAVES
ASSOCIATED WITH MAGNETAR BURSTS DURING LIGO'S SIXTH SCIENCE
RUN

by

RYAN QUITZOW-JAMES

A DISSERTATION

Presented to the Department of Physics
and the Graduate School of the University of Oregon
in partial fulfillment of the requirements
for the degree of
Doctor of Philosophy

March 2016

DISSERTATION APPROVAL PAGE

Student: Ryan Quitzow-James

Title: Search for Long-Duration Transient Gravitational Waves Associated with Magnetar Bursts during LIGO's Sixth Science Run

This dissertation has been accepted and approved in partial fulfillment of the requirements for the Doctor of Philosophy degree in the Department of Physics by:

James E. Brau	Chair
Raymond E. Frey	Advisor
Timothy Cohen	Core Member
Daniel A. Steck	Core Member
James A. Isenberg	Institutional Representative

and

Scott L. Pratt	Dean of the Graduate School
----------------	-----------------------------

Original approval signatures are on file with the University of Oregon Graduate School.

Degree awarded March 2016

© 2016 Ryan Quitzow-James
This work is licensed under a Creative Commons
Attribution-NonCommercial-NoDerivs (United States) License.

DISSERTATION ABSTRACT

Ryan Quitzow-James

Doctor of Philosophy

Department of Physics

March 2016

Title: Search for Long-Duration Transient Gravitational Waves Associated with Magnetar Bursts during LIGO's Sixth Science Run

Soft gamma repeaters (SGRs) and anomalous X-ray pulsars are thought to be neutron stars with strong magnetic fields, called magnetars, which emit intermittent bursts of hard X-rays and soft gamma rays. Three highly energetic bursts, known as giant flares, have been observed originating from three different SGRs, the latest and most energetic of which occurred on December 27, 2004, from the SGR with the largest estimated magnetic field, SGR 1806-20. Modulations in the X-ray tails of giant flares may be caused by global seismic oscillations. Non-radial oscillations of the dense neutron star matter could emit gravitational waves powered by the magnetar's magnetic energy reservoir. This analysis searched for long-duration transient gravitational waves associated with three magnetar bursts that occurred during LIGO's sixth science run, from July 7, 2009 to October 20, 2010. The search results were consistent with the calculated background, and 90% confidence upper limits on the possible undetected gravitational wave energy were found.

CURRICULUM VITAE

NAME OF AUTHOR: Ryan Quitzow-James

GRADUATE AND UNDERGRADUATE SCHOOLS ATTENDED:

University of Oregon, Eugene, OR
Sonoma State University, Rohnert Park, CA

DEGREES AWARDED:

Doctor of Philosophy, Physics, 2016, University of Oregon
Master of Science, Physics, 2008, University of Oregon
Bachelor of Science, Physics, 2005, Sonoma State University

AREAS OF SPECIAL INTEREST:

Gravitational Waves, General Relativity, Magnetars

PROFESSIONAL EXPERIENCE:

Graduate Research Assistant, University of Oregon, 2009–2016
Graduate Teaching Fellow, University of Oregon, 2006–2009, 2016

GRANTS, AWARDS AND HONORS:

LIGO Student Fellowship, 2011–2012
Physics and Astronomy Scholarship, Sonoma State University, 2004–2005

PUBLICATIONS:

J. Aasi et al. Characterization of the LIGO detectors during their sixth science run. *Classical and Quantum Gravity*, 32:115012, 2015.

ACKNOWLEDGEMENTS

This work would not have been possible without the many people who have helped me along the way, either in becoming a better scientist, or a better human being. Words cannot adequately express my thanks to all who have helped and supported me.

I would like to thank my advisor, Raymond Frey, for his guidance and support and the opportunity to work with LIGO. I would also like to thank James Brau for many helpful discussions. I would like to thank my committee members Daniel Steck, Timothy Cohen and James Isenberg.

I owe special thanks to Dipongkar Talukder who took the time to help me learn the ropes of high throughput computing and running analyses with LIGO data. Michael Coughlin provided invaluable support in learning to run STAMP. I would also like to thank Robert Schofield for help in understanding noise sources in the LIGO detectors. Thanks to Vincent Roma for reading an advance copy of this dissertation.

I am grateful to the National Science Foundation and the LIGO Scientific Collaboration for the funding, resources and data to support my research. I want to express my sincere thanks to James Clark, Eric Thrane, Scott Coughlin, Gregory Mendell, Daniel Sigg, Richard Savage and the many other members of LIGO Scientific Collaboration and the Virgo Collaboration.

I have received help from many friends. Ryan Hopkins, André Soileau and Mary Robinson have been there for me over many years. I am grateful to Sue Kamalo, Norma Santiago, Maria Artel and Julia Everta for the love and kindness they showed my mom. Thanks to my brother's good friend, McKenzie Anderson, for her kindness and support. Wayne Manselle helped me learn to program at the beginning of my

research. I have enjoyed my time with my friends and martial arts teachers, Matthew Lowes and Kaizen Taki, who have helped me stay active and sane. I want to express my sincere thanks to Paul Crowley who provided invaluable counsel and support.

Finally, thanks to my family, whose love and support have helped me find my path. Thank you for keeping me sane over these past years. Growing up, I had the benefit of participating in many conversations with my family about scientific topics, which helped foster my interest and curiosity. I had many opportunities to visit my uncle Anthony James' mosquito lab at a young age, and he also provided my first introduction to LIGO over a decade and a half ago. Thank you to my grandparents, Bernard James, Florence Fitzgerald, OEloel Braun, and Edwin Braun; my aunts and uncles, Frank James, Anthony James, Maria James, Newton Lam, Josefa James, Chris James, Philip James, Lisa James, Bea James, David James, Isabel James, Eric Braun and Paula Tanksley; my cousins, James Brandon and Ivan James and the rest of my extended family. My sincere thanks to my aunt, Cynthia French, for providing needed guidance while my mother was ill. I am grateful to Linda James and my sister, Ellie James, for their love and support. I am thankful to my dad, Will James, for his love and kindness and for helping make me who I am. He has provided invaluable support, including many hours reading my thesis and helping with edits. I am sincerely grateful for the friendship and love of my brother, Kainalu Quitzow, who has helped me through hard times and continues to make me a better person. My mom, Bree Quitzow, passed away in 2012. To her, I owe everything.

Thank you all.

DEDICATION

To my parents; my mom, who is no longer here, and my dad, who is still with me.

To my siblings; my brother, whose growth into an adult has amazed me, and my sister, who always makes me smile.

To my family, who is always there for me.

TABLE OF CONTENTS

Chapter	Page
I. GRAVITATIONAL WAVES AND MAGNETARS	1
II. GENERAL RELATIVITY AND GRAVITATIONAL WAVES	7
2.1. Einstein's Equations	7
2.2. Einstein's Equations in Weak Gravitational Fields	10
2.3. Gravitational Wave Propagation	12
2.4. Quadrupole Moment and Gravitational Waves	16
2.5. Effect on Free Test Particles	19
III. INTERFEROMETRIC GRAVITATIONAL WAVE DETECTORS	23
3.1. Detector Design	23
3.2. Noise Limits	35
3.3. Potential Gravitational Wave Sources	39
IV. SEISMIC UPCONVERSION	47
4.1. Monitoring Upconversion	48
4.2. Range Predictor	56
4.3. Correlation with Low-Frequency Low-SNR Glitches	58

Chapter	Page
V. ASTROPHYSICS OF MAGNETARS	61
5.1. Soft Gamma Repeaters and Anomalous X-Ray Pulsars	61
5.2. Electromagnetic Emission from SGRs and AXPs	64
5.3. The Magnetar Model	70
5.4. Gravitational Wave Emission from Magnetars	76
VI. METHODOLOGY	79
6.1. Data Sources	80
6.2. Search Pipeline: STAMP	81
6.3. Data Analysis Procedures	84
VII. RESULTS OF GRAVITATIONAL WAVE SEARCH	100
7.1. Search Results	100
7.2. Upper Limits	108
7.3. Absolute Value SNR Modification	131
VIII. SUMMARY AND CONCLUSIONS	135
APPENDICES	
A. CONVENTIONS AND EQUATIONS	141
A.1. Conventions	141

Chapter	Page
A.2. Definitions	141
A.3. Identities	142
A.4. Linearized Tensors	142
B. DERIVATION OF UPPER LIMITS	147
B.1. Calculating h_{rss}	148
B.2. Calculating E_{GW}	153
B.3. E_{GW} and h_{rss} for a Half Sine-Gaussian	163
B.4. Comparing to Fluence	164
B.5. Comparing to Isotropic Sine-Gaussian Emission	165
C. CALIBRATION ERROR	167
REFERENCES CITED	172

LIST OF FIGURES

Figure	Page
1.1. The parabolic line shows the shift in the periastron from orbital energy loss due to GW radiation as predicted by general relativity. The dots are data points from observations, which agree well with predictions.	2
1.2. The gravitational-wave event GW150914 as observed by the LIGO detectors.	6
2.1. As a GW passes perpendicular to the plane of the paper, a ring of test particles would be deformed. The top row shows the effect of a GW with plus polarization, and the bottom row shows the effect of a GW with cross polarization.	15
3.1. A Michelson interferometer.	25
3.2. The distortion in spacetime from a passing GW affects the arms of a Michelson interferometer differently, allowing probing of the GW amplitude by measuring the change in the difference in arm lengths.	26
3.3. Simplified layout of the LIGO interferometer. The OMC was added for eLIGO in S6.	27
3.4. Modified Michelson Interferometer with Fabry-Perot Cavities.	29
3.5. Power Recycled Modified Michelson Interferometer with Fabry-Perot Cavities.	30
3.6. Schematic of suspension used in LIGO.	35
3.7. A normal strain ASD for H1 and L1 in S6.	36
4.1. Upconversion noise and actuator coil current.	48
4.2. Schematic of the optic suspension.	49
4.3. Test mass actuator coil current BLRMS ² (0.1–0.3 Hz band) versus detector strain BLRMS ² (70–110 Hz band) for a time during S6 with very clear seismic upconversion.	51

Figure	Page
4.4. Minimal bound slopes plotted against frequency. This was a test looking at many bands. Outliers cause the minimal bound fit to produce high slopes.	54
4.5. H1 and L1 weighting functions plotted with a test weighting function calculated for H1 and fit to the grey points. The y-axis is the weighting factor from coil current BLRMS ² to strain BLRMS ² . The outliers were reduced before calculating the minimal bounds by removing a small percentage of the loudest points in the coil current and requiring a minimum of 10 points in each bin.	55
4.6. Weighted coil current is correlated with drops in the BNS range.	57
4.7. Seasonal increase in seismic upconversion due to McNary Dam overflow.	58
4.8. Low-frequency low-SNR glitches and seismic upconversion.	60
5.1. Time series of data of the 2004 giant flare from SGR 1806-20.	67
7.1. The on-source event plotted against the background for SGR trigger 2469.	102
7.2. The on-source event plotted against the background for SGR trigger 2471.	103
7.3. The on-source event plotted against the background for SGR trigger 2475.	104
7.4. FAP vs SNR for 2469 for abs SNR version. For the on-source event, SNR = 6.06 and FAP = 0.679.	105
7.5. FAP vs SNR for 2475 for abs SNR version. For the on-source event, SNR = 6.24 and FAP = 0.378.	106
7.6. FT-map from STAMP for SGR trigger 2475.	106
7.7. Loudest cluster found by STAMP's seedless clustering algorithm, stochtrack, for SGR trigger 2475.	107
7.8. Detection efficiency vs injected strain h_0 for SGR trigger 2469. Waveforms are circularly polarized with $\iota = 0^\circ$ and $\psi = 0^\circ$	124
7.9. Plot of the detection efficiency vs injected strain h_0 for SGR trigger 2471. Waveforms are circularly polarized with $\iota = 0^\circ$ and $\psi = 0^\circ$	125

Figure	Page
7.10. Plot of the detection efficiency vs injected strain h_0 for SGR trigger 2475. Waveforms are circularly polarized with $\iota = 0^\circ$ and $\psi = 0^\circ$	126
7.11. Detection efficiency vs injected strain h_0 for SGR trigger 2469. Waveforms calculated for $\iota = 120^\circ$ and $\psi = 45^\circ$	127
7.12. Plot of the detection efficiency vs injected strain h_0 for SGR trigger 2471. Waveforms calculated for $\iota = 103^\circ$ and $\psi = 45^\circ$	128
7.13. Plot of the detection efficiency vs injected strain h_0 for SGR trigger 2475. Waveforms calculated for $\iota = 120^\circ$ and $\psi = 45^\circ$	129
7.14. SNR response to injected strain h_0	130
7.15. SNR vs $\cos \iota$ for SGR trigger 2475.	132
7.16. SNR vs $\cos \iota$ for SGR trigger 2471.	133
7.17. SNR vs $\cos \iota$ for SGR trigger 2475 with absolute value SNR modification.	134

LIST OF TABLES

Table	Page
4.1. Weighted coil current thresholds chosen for flags and the fraction of time during S6 that is flagged for each threshold.	56
6.1. Information on S6 magnetar burst triggers.	85
6.2. Commands to find science segment times during S6 and save in text files.	86
6.3. Information on S6 magnetar burst source positions and distances from Earth	87
6.4. Information on S6 magnetars burst sources proper motions.	87
6.5. Search window parameters.	90
6.6. On-source windows.	90
6.7. Lines identified and notched for trigger 2469.	92
6.8. Lines identified and notched for trigger 2471.	93
6.9. Lines identified and notched for trigger 2475.	94
7.1. Summary of open-box results	101
7.2. Initial values of τ to test.	110
7.3. Waveform parameters.	111
7.4. Waveform parameters for non-circular polarizations. $\iota = 0^\circ$ and $\psi = 0^\circ$ were used for circular polarizations for all triggers.	112
7.5. Waveform parameters used for non-circular polarizations.	112
7.6. Upper limits for 90% CL for circularly polarized signals with $\iota = 0^\circ$ and $\psi = 0^\circ$	120
7.7. Upper limits for 50% CL for circularly polarized signals with $\iota = 0^\circ$ and $\psi = 0^\circ$	121
7.8. Upper limits for 50% CL for circularly polarized signals with $\iota = 0^\circ$ and $\psi = 0^\circ$ with percentage from calibration error.	122

Table	Page
7.9. Upper limits for 90% CL for signals with polarization described in Table 7.4.	123
7.10. Upper limits for 50% CL for signals with polarization described in Table 7.4.	123
8.1. Summary of best upper limits and comparisons to possible energy sources. $E_{\vec{B} \approx 10^{15} \text{ gauss}}$ is approximated as 10^{47} erg.	138
8.2. Summary of best upper limit and equivalent aLIGO upper limit. Includes comparisons to electromagnetic energy levels of giant flares.	140
C.1. Recommended calibration error for S6.	167
C.2. Recommended calibration error for S6 excluding 3000–4000 Hz in H1. . .	168

CHAPTER I

GRAVITATIONAL WAVES AND MAGNETARS

Albert Einstein's special theory of relativity preferred objects to be in an inertial frame; however, Einstein reasoned that a theory that did not prefer a state of motion would be superior, and thus, he embarked on formulating general relativity [1]. In 1915, Einstein published his general theory of relativity [2]. In 1916, Einstein laid the groundwork for gravitational-wave theory and predicted linearized gravitational waves (GWs) [3, 4]. GWs are tensor waves predicted to travel at the speed of light, stretching and compressing space perpendicular to their direction of travel.

Russell A. Hulse and Joseph H. Taylor Jr. received the 1993 physics Nobel Prize for the first observational evidence supporting the existence of GWs [5]. Discovered by Hulse and Taylor in 1974, PSR B1913+16 is a binary star system containing two neutron stars, one of which is a pulsar. The pulsar is a reliable natural clock and allowed very precise measurement of the orbital period of the system (approximately 7.75 hours) [6]. More than three decades of observations found that the orbital period was decreasing at 0.997 ± 0.002 times the rate predicted by general relativity from energy loss due to gravitational wave emission (see Figure 1.1) [6]. This successful observation is often termed an indirect measurement of GWs because it is an observation of energy loss attributed to GWs rather than an observation of the GWs distortion of spacetime.

On September 14, 2015, at 09:50:45 UTC, the two detectors of the Laser Interferometer Gravitational-Wave observatory (LIGO) directly detected a gravitational wave signal (see Figure 1.2) [7]. This GW event is known as GW150914. The time difference between the event times in each detector was less than the 10 ms light travel time between the detectors. The signal ranged in frequency from 35 Hz to

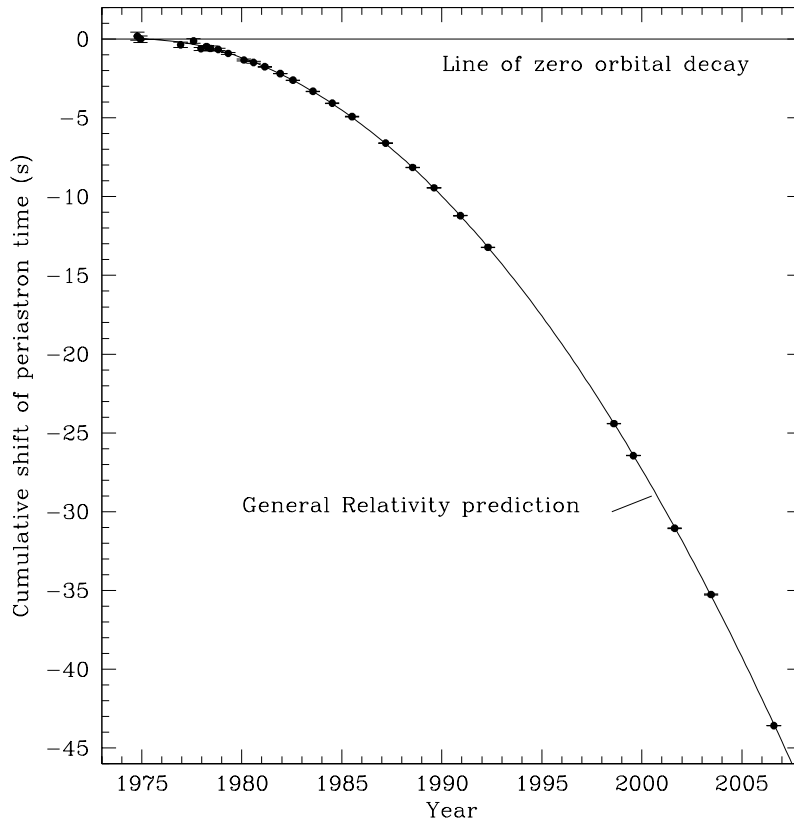


FIGURE 1.1. The parabolic line shows the shift in the periastron from orbital energy loss due to GW radiation as predicted by general relativity. The dots are data points from observations, which agree well with predictions. Figure © AAS. Reproduced with permission from [6].

250 Hz, with a peak GW strain amplitude of 10^{-21} . When recovered with a matched-filter analysis, the signal matched the features of a binary black hole inspiral, merger and ringdown. The masses of the merging black holes were estimated to be $36_{-4}^{+5} M_{\odot}$ and $29_{-4}^{+4} M_{\odot}$, with the resulting black hole mass estimated to be $62_{-4}^{+4} M_{\odot}$. The event emitted $3_{-0.5}^{+0.5} M_{\odot} c^2$ as GW energy. GW150914 is the first direct detection of GWs. GW150914 is also the first observation of a binary black hole system and provided observations of space-time in regions with strong-field gravity and high-velocity objects,

and confirmed “predictions of general relativity for the nonlinear dynamics of highly disturbed black holes” [7].

Additional detections in the future should increase our knowledge of the universe and general relativity. Measuring the polarization properties of GWs could verify general relativity’s prediction of the transverse traceless nature of the waves and the spin-two nature of gravitons [3]. GWs could be compared with optical counterparts to verify whether they travel at the speed of light [8]. GWs are not expected to be significantly affected by most matter and are instead sensitive to coherent motions of large amounts of matter [3, 8]. This weak coupling to low-density matter would allow observations of phenomena unobservable with electromagnetic radiation, such as information from star cores in supernovae, compact star (neutron stars or black holes) mergers or even observations from the early universe before light could travel freely (the earliest electromagnetic observations are of the cosmic microwave background radiation) [3, 8].

The LIGO Scientific Collaboration and Virgo Collaboration use a global network of three interferometer detectors to search for GWs. In 2015, LIGO finished upgrades to its second generation configuration, known as Advanced LIGO (aLIGO), and completed its first observation run from September, 2015, to January, 2015. More tuning will be required, but once aLIGO reaches design sensitivity it is expected to be 10 times as sensitive as initial LIGO and have a search volume 1000 times larger.

Soft gamma repeaters (SGRs) and anomalous X-ray pulsars (AXPs) may emit GWs that could be detectable by the LIGO detector network. SGRs and AXPs emit energetic bursts of X-ray and gamma rays which are thought to be powered by large magnetic fields. Neutron stars which possess extraordinary strong magnetic fields are called magnetars. They have external dipole magnetic fields of $\sim 10^{13}$ – 10^{15} gauss as

inferred by their spin periods and spin-down rates [9]. Two of their largest emissions, called giant flares, have quasiperiodic oscillations (QPOs) visible in the tails following the initial burst. This suggests bursts may cause oscillations which may emit GWs. These oscillations occur in frequencies to which LIGO is sensitive. Two models for burst emission, crust cracking and hydrodynamic deformation, may provide enough energy to power the electromagnetic bursts and GWs of comparable or greater energies [10]. If the GW emission energy is similar to the electromagnetic burst emission energy, magnetars could emit GWs which could be detectable by LIGO. If not, restrictions could be set on the energy content of the mechanisms of excitation.

This search analyzed data from both LIGO detectors to look for long-duration transient GWs which occurred during or just after magnetar bursts. Three magnetar bursts occurred while both of LIGO's detectors were taking data during LIGO's sixth science run (S6), from July 7, 2009 to October 20, 2010. There is much uncertainty in the possible mechanisms behind bursts; therefore, no particular waveform was assumed for this search. The choice of clustering algorithm and search pipeline was motivated by electromagnetic observations. If emitted GWs are related to QPOs, GWs may be long lasting and nearly monochromatic. A cross-correlation search was performed using a seedless clustering algorithm sensitive to long and thin signals which may change in frequency or be nearly monochromatic. The statements made in this thesis are my own; the analysis and results have not been reviewed by the LIGO Scientific Collaboration.

The chapters of this thesis are organized as described below.

Chapter II focuses on general relativity, and the basic linearized theory of GWs, as well as the basic idea of strain which could allow GWs to be detected.

Chapter III focuses on the LIGO detector, noise sources in the detector, and possible sources of GWs in LIGO's sensitive frequency band.

Chapter IV discusses the work done to monitor seismic upconversion in LIGO's sixth science run.

Chapter V discusses magnetars, their history, and some basic observations about them and why they may be good candidates for detection of GW emission.

Chapter VI discusses the search methodology, detailing the chosen pipeline and clustering algorithm and the process of how it was used to search for GWs.

Chapter VII discusses the results, and details the upper limits and the methodology to find the upper limits.

Chapter VIII makes the concluding remarks.

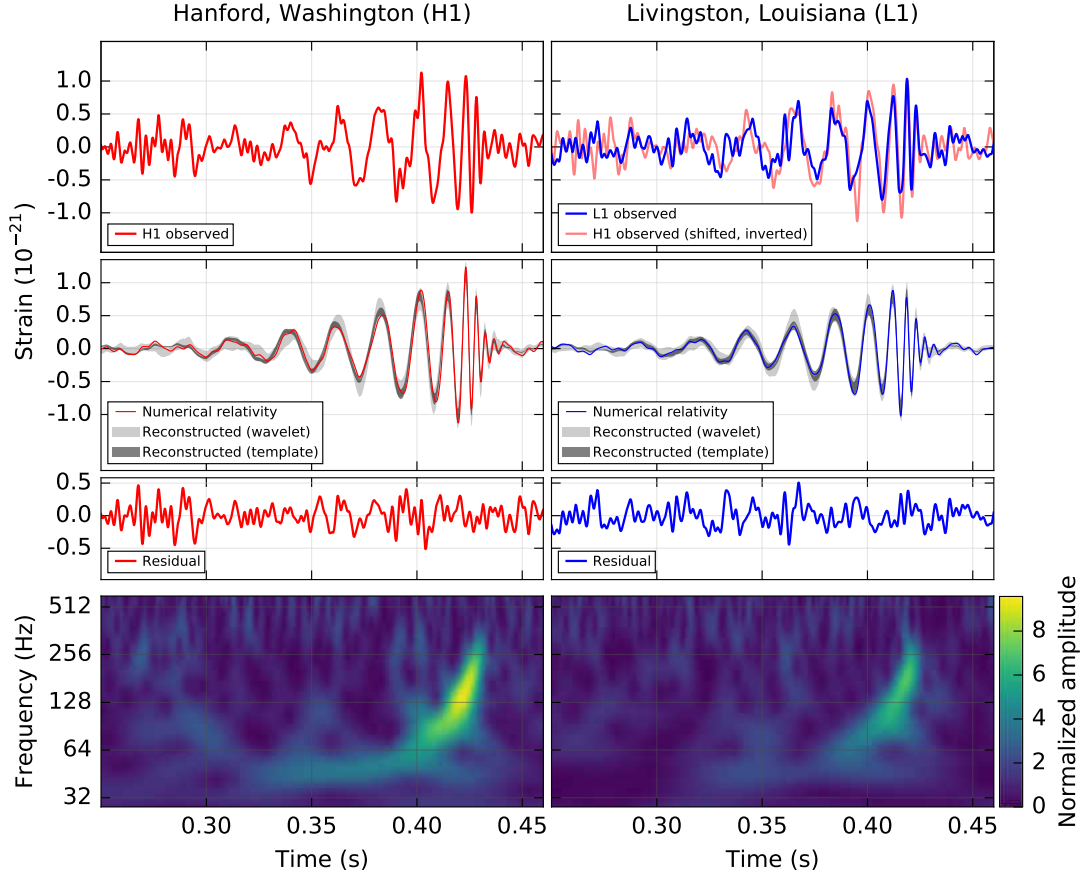


FIGURE 1.2. The gravitational-wave event GW150914 as observed by the LIGO detectors (left is the detector in Hanford, Washington, and right is the detector in Livingston, Louisiana) [7]. The times are relative to September 14, 2015 at 09:50:45 UTC and all time series have been filtered using a 35–350 Hz bandpass filter and additional band-reject filters to remove instrumental spectral lines. Top row: Strain for each detector. Second row: Numerical relativity waveform projected onto each detector. Shaded regions show 90% credible regions using sine-Gaussian wavelets (light gray) and binary black hole template waveforms (dark gray). Third row: Residual strain time series after subtracting filtered numerical relativity waveform. Bottom row: A frequency-time representation of the GW signal. Figure from [7].

CHAPTER II

GENERAL RELATIVITY AND GRAVITATIONAL WAVES

Gravitational wave (GW) emission is predicted by general relativity. Calculating GWs is very complex, requiring numerical relativity in strong fields [3]. The concept can be demonstrated in the weak-field approximation. In this case, flat-space is assumed as the background with a perturbation from distant simple point masses.

For this derivation, Einstein summation convention will be used with Greek letters ranging over 4-dimensional space-time from 0 to 3, with 0 representing the dimension of time. Roman letters will be used to refer specifically to the 3 spatial dimensions ranging from 1 to 3. Upper indices will be contravariant, and lower indices will be covariant. Natural units will often be used to simplify equations. Please see Appendix A.1 for conventions.

2.1. Einstein's Equations

A relativistic description of gravity needs to be coordinate independent. This description should reduce to the Newtonian version in the limit of weak gravity and low-velocity ($v \ll c$ where c is the speed of light and equals 1 in natural units). Newtonian gravity cannot be described in a coordinate independent way because it treats time differently than relativity and assumes all of space shares a well-defined time [11]. In the Newtonian theory of gravity, mass is the source of the gravitational field. Newtonian theory gives the following relation between mass and the gravitational potential:

$$\nabla^2\phi(\vec{\mathbf{r}}) = 4\pi G\rho(\vec{\mathbf{r}}) \tag{2.1}$$

Here G is the gravitational constant, $\phi(\vec{\mathbf{r}})$ is the gravitational potential, and $\rho(\vec{\mathbf{r}})$ is the mass density.

While the “rest mass” of a particle or object is invariant, the density depends on a particular measurement of space and is not conserved between frames. The relativistic generalization of $\rho(\vec{\mathbf{r}})$ is the stress-energy tensor \mathbf{T} [11, 12]. The Laplacian and the gravitational potential $\phi(\vec{\mathbf{r}})$ also treat time and space differently and therefore depend on the coordinates of spacetime. In general relativity, gravity is identified with the curvature of space-time (which can be described by a rank 2 tensor known as the metric, often represented as $g_{\mu\nu}$). The left side of (2.1) can be generalized with a coordinate independent second order differential operator on the metric, $\mathbf{O}(g_{\mu\nu})$ [12]. The stress energy tensor is now related with the curvature of space-time:

$$\mathbf{O}(g_{\mu\nu}) = k\mathbf{T} \tag{2.2}$$

$T^{\mu\nu}$ is a symmetric rank 2 tensor in four dimensions, so there are 10 independent components to this equation. Because $T^{\mu\nu}$ is a 2nd rank tensor, \mathbf{O} must produce a rank 2 tensor when operating on the metric. This means \mathbf{O} should be a second rank tensor consisting of combinations of the metric and first and second derivatives of the metric [12]. The Ricci tensor fits this description, however conservation of energy would require that \mathbf{T} was a constant [11]. More generally, any tensor will satisfy these constraints if it is of the form [12]:

$$\mathbf{O}(g_{\mu\nu}) = O^{\alpha\beta} = R^{\alpha\beta} + \mu g^{\alpha\beta} R + \Lambda g^{\alpha\beta} \tag{2.3}$$

where Λ and μ are constants. $R^{\mu\nu}$ and R are the Ricci tensor and Ricci scalar and are defined as:

$$R_{\mu\nu} = R^{\alpha}{}_{\mu\alpha\nu} = R_{\nu\mu} \quad (2.4)$$

$$R = g^{\mu\nu} R_{\mu\nu} = g^{\mu\nu} g^{\alpha\beta} R_{\alpha\mu\beta\nu} \quad (2.5)$$

$R_{\alpha\mu\beta\nu}$ is the Riemann curvature tensor:

$$R^{\alpha}{}_{\beta\mu\nu} = \partial_{\mu}\Gamma^{\alpha}{}_{\beta\nu} - \partial_{\nu}\Gamma^{\alpha}{}_{\beta\mu} + \Gamma^{\alpha}{}_{\sigma\mu}\Gamma^{\sigma}{}_{\beta\nu} - \Gamma^{\alpha}{}_{\sigma\nu}\Gamma^{\sigma}{}_{\beta\mu} \quad (2.6)$$

$\Gamma^{\mu}{}_{\alpha\beta}$ is the Christoffel symbol:

$$\Gamma^{\mu}{}_{\alpha\beta} = \frac{1}{2}g^{\mu\nu}(\partial_{\beta}g_{\nu\alpha} + \partial_{\alpha}g_{\nu\beta} - \partial_{\nu}g_{\alpha\beta}) \quad (2.7)$$

Lowering the index on $R^{\alpha}{}_{\beta\mu\nu}$ to $R_{\alpha\beta\mu\nu}$ gives:

$$R_{\alpha\beta\mu\nu} = g_{\alpha\lambda}R^{\lambda}{}_{\beta\mu\nu} = \frac{1}{2}(\partial_{\beta}\partial_{\mu}g_{\alpha\nu} - \partial_{\beta}\partial_{\nu}g_{\alpha\mu} + \partial_{\alpha}\partial_{\nu}g_{\beta\mu} - \partial_{\alpha}\partial_{\mu}g_{\beta\nu}) \quad (2.8)$$

Indices can be raised and lowered using $g_{\mu\nu}$:

$$g_{\mu\nu}A^{\nu} = A_{\mu} \quad (2.9)$$

$$g^{\mu\nu}A_{\nu} = A^{\mu} \quad (2.10)$$

Using the Einstein equivalence principle to require local conservation of energy, it can be found that $\mu = -\frac{1}{2}$ [12]. This gives the general form of the Einstein field equations:

$$R^{\mu\nu} - \frac{1}{2}g^{\mu\nu}R + \Lambda g^{\mu\nu} = kT^{\mu\nu} \quad (2.11)$$

The Einstein tensor $G^{\mu\nu}$ is defined as:

$$G^{\mu\nu} = R^{\mu\nu} - \frac{1}{2}g^{\mu\nu}R \quad (2.12)$$

Using the Einstein tensor, (2.11) can be written as:

$$G^{\mu\nu} + \Lambda g^{\mu\nu} = kT^{\mu\nu} \quad (2.13)$$

The constant Λ is known as the cosmological constant. It was added by Einstein to allow static solutions to the overall distribution of matter [13]. Later observations by Edwin Hubble suggesting an expanding universe caused him to remove the term [12, 14]. More recent observations of an accelerating universe suggest the term is small but non-zero [12, 15]. For the following derivations, Λ will be set to zero.

The value of k in (2.13) can be found to be 8π in natural units by requiring the equations accurately describe the behavior of the planets in the solar system [12]. This gives the following equation:

$$G^{\alpha\beta} = 8\pi T^{\alpha\beta} \quad (2.14)$$

Or in SI or CGS units [8]:

$$G^{\alpha\beta} = \frac{8\pi G}{c^4} T^{\alpha\beta} \quad (2.15)$$

2.2. Einstein's Equations in Weak Gravitational Fields

Weak gravitational fields can be represented as a small perturbation ($h_{\mu\nu}$) about a flat-space background (represented with the Minkowski metric: $\eta_{\mu\nu}$):

$$g_{\mu\nu} = \eta_{\mu\nu} + h_{\mu\nu} \quad (2.16)$$

where the Minkowski metric is:

$$\eta_{\mu\nu} = \begin{bmatrix} -1 & 0 & 0 & 0 \\ 0 & 1 & 0 & 0 \\ 0 & 0 & 1 & 0 \\ 0 & 0 & 0 & 1 \end{bmatrix} \quad (2.17)$$

and the elements of the perturbation $h_{\mu\nu}$ are much smaller than 1:

$$|h_{\mu\nu}| \ll 1 \quad (2.18)$$

The first step to get a weak-field version of (2.14) is to get a weak-field version of the Riemann curvature tensor. The Riemann curvature tensor can be represented in terms of just $h_{\mu\nu}$ (see Appendix A.4 for the derivation):

$$R_{\alpha\beta\mu\nu} = \frac{1}{2}(\partial_\beta\partial_\mu h_{\alpha\nu} + \partial_\alpha\partial_\nu h_{\beta\mu} - \partial_\beta\partial_\nu h_{\alpha\mu} - \partial_\alpha\partial_\mu h_{\beta\nu}) \quad (2.19)$$

Using (2.19) with (2.12), we find a weak-field version of $G_{\mu\nu}$ (derivation again in Appendix A.4):

$$G_{\mu\nu} = -\frac{1}{2}(\square\bar{h}_{\mu\nu} - \partial^\gamma\partial_\mu\bar{h}_{\gamma\nu} - \partial_\nu\partial^\gamma\bar{h}_{\mu\gamma} + \eta_{\mu\nu}\partial^\gamma\partial^\beta\bar{h}_{\gamma\beta}) \quad (2.20)$$

where \square is the d'Alembert operator and $\bar{h}_{\mu\nu}$ is the “trace reverse” of $h_{\mu\nu}$:

$$\square = \partial^\mu\partial_\mu = -\frac{1}{c^2}\frac{\partial^2}{\partial t^2} + \nabla^2 \quad (2.21)$$

$$\bar{h}_{\mu\nu} = h_{\mu\nu} - \frac{1}{2}\eta_{\mu\nu}h^\alpha{}_\alpha = h_{\mu\nu} - \frac{1}{2}\eta_{\mu\nu}h \quad (2.22)$$

where h is the trace of $h_{\mu\nu}$:

$$h = h^\mu{}_\mu \quad (2.23)$$

The Lorenz gauge condition is:

$$\partial_\nu \bar{h}^{\mu\nu} = 0 \quad (2.24)$$

Using the Lorenz gauge condition, (2.20) simplifies to:

$$G_{\mu\nu} = -\frac{1}{2}\square\bar{h}_{\mu\nu} \quad (2.25)$$

Plugging (2.25) into (2.14) gives the linear form of the Einstein equations:

$$\square\bar{h}^{\mu\nu} = -16\pi T^{\mu\nu} \quad (2.26)$$

2.3. Gravitational Wave Propagation

In order to more easily look at GW radiation, a region of space far from any matter or energy can be examined. Choosing a region of spacetime such that the stress-energy tensor $T^{\mu\nu} = 0$ gives the following from (2.26):

$$\square\bar{h}^{\mu\nu} = 0 \quad (2.27)$$

Writing out the d'Alembert operator explicitly gives:

$$\left(-\frac{\partial^2}{\partial t^2} + \nabla^2\right)\bar{h}^{\mu\nu} = 0 \quad (2.28)$$

This is the three dimensional wave equation, the solution to which can be shown to be of the form:

$$\bar{h}^{\mu\nu} = A^{\mu\nu} e^{ik_\alpha x^\alpha} \quad (2.29)$$

Applying (2.28) to (2.29) and using the fact that $\partial_\beta e^{ik_\alpha x^\alpha} = ik_\beta e^{ik_\alpha x^\alpha}$ gives the following:

$$\partial^\alpha \partial_\alpha \bar{h}^{\mu\nu} = \partial^\alpha \partial_\alpha A^{\mu\nu} e^{ik_\beta x^\beta} = -k^\alpha k_\alpha \bar{A}^{\mu\nu} e^{ik_\beta x^\beta} = -k^\alpha k_\alpha \bar{h}^{\mu\nu} = 0 \quad (2.30)$$

If $\bar{h}^{\mu\nu}$ is non-zero, the the term in front of it must be zero:

$$k^\alpha k_\alpha = 0 \quad (2.31)$$

A vector k^μ satisfying (2.31) is known as a ‘‘Killing vector’’. Taking the derivative of (2.29) and using the Lorenz gauge condition (2.24) gives the following condition:

$$\partial_\nu \bar{h}^{\mu\nu} = ik_\nu \bar{h}^{\mu\nu} \quad (2.32)$$

$$0 = ik_\nu A^{\mu\nu} e^{ik_\beta x^\beta} \quad (2.33)$$

$$0 = k_\nu A^{\mu\nu} \quad (2.34)$$

(2.34) can only be true if k_ν and $A^{\mu\nu}$ are perpendicular. This solution describes a plane wave. Any solution to (2.24) and (2.28) can be described as a superposition of plane waves.

Two more gauge fixing conditions can be chosen to give two additional constraints on $A_{\mu\nu}$ [12]:

$$A^\mu{}_\mu = 0 \quad (2.35)$$

$$A_{\mu\nu}U^\nu = 0 \quad (2.36)$$

(2.35) and (2.36) along with (2.34) are known as the transverse-traceless gauge conditions. The trace condition means $\bar{h}_{\mu\nu}^{TT} = h_{\mu\nu}^{TT}$.

A Lorentz frame for the background Minkowski metric can be chosen such that the wave is traveling along the z direction ($k^\mu = [\omega, 0, 0, \omega]$) and the vector the transverse traceless gauge is based on is $U^\nu = \delta^\nu_0$. In this frame:

$$A_{\mu\nu}U^\nu = A_{\mu\nu}\delta^\nu_0 = A_{\mu 0} = 0 \quad (2.37)$$

and:

$$k_\nu A^{\mu\nu} = -k_0 A^{\mu 0} + k_z A^{\mu z} = -k_0 \times (0) + k_z A^{\mu z} = \omega A^{\mu z} = 0 \quad (2.38)$$

which gives $A_{\mu z} = 0$. The “transverse” part of the gauge describes the fact that $A_{\mu\nu}$ is transverse to the direction of propagation. This leaves A_{xx} , A_{xy} , A_{yx} and A_{yy} as the only non-zero components. $A^{\mu\nu}$ is related to the stress-energy tensor which is symmetric, so $A_{xy} = A_{yx}$. (2.35) requires $A_{yy} = -A_{xx}$. This gives:

$$A_{\mu\nu}^{TT} = \begin{bmatrix} 0 & 0 & 0 & 0 \\ 0 & A_{xx} & A_{xy} & 0 \\ 0 & A_{xy} & -A_{xx} & 0 \\ 0 & 0 & 0 & 0 \end{bmatrix} \quad (2.39)$$

Plugging this in to (2.29), and using the fact that in the transverse traceless gauge $\bar{h}_{\mu\nu} = h_{\mu\nu}$, gives the following:

$$h_{\mu\nu} = \begin{bmatrix} 0 & 0 & 0 & 0 \\ 0 & h_{xx} & h_{xy} & 0 \\ 0 & h_{xy} & -h_{xx} & 0 \\ 0 & 0 & 0 & 0 \end{bmatrix} \quad (2.40)$$

From this, the canonical polarizations can be derived (+ polarization $A_{xy} = 0$ and \times polarization $A_{xx} = 0$):

$$h_{\mu\nu} = \begin{bmatrix} 0 & 0 & 0 & 0 \\ 0 & h_+ & h_\times & 0 \\ 0 & h_\times & -h_+ & 0 \\ 0 & 0 & 0 & 0 \end{bmatrix} \quad (2.41)$$

The GW polarizations are shown in Figure 2.1.

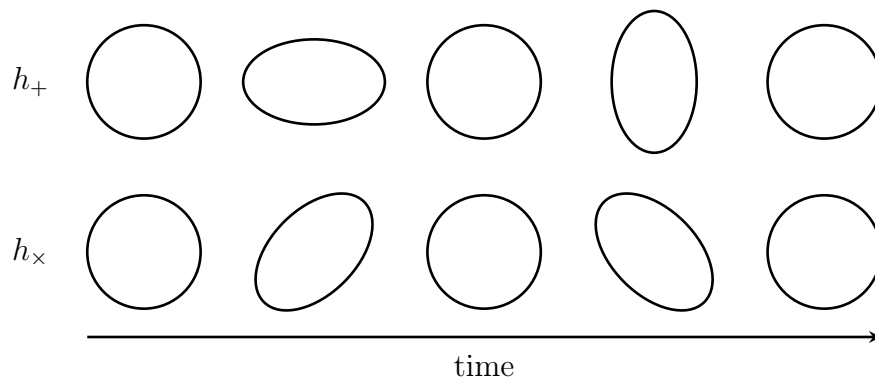


FIGURE 2.1. As a GW passes perpendicular to the plane of the paper, a ring of test particles would be deformed. The top row shows the effect of a GW with plus polarization, and the bottom row shows the effect of a GW with cross polarization.

2.4. Quadrupole Moment and Gravitational Waves

For this section, we will consider the slow motion approximation for a quadrupole moment generating GWs. The assumptions include that the source term is much smaller than the wavelengths of the generated waves, and that the speeds of the involved sources are not relativistic ($v \ll c$). To find the equations for $\bar{h}_{\mu\nu}$ for a GW of frequency $f = \Omega/2\pi$ in the slow motion approximation in a weak-field far from the source at distance r , both sides of (2.26) can be integrated. Assuming $T_{\mu\nu}$ sinusoidally varies in time with a frequency $f = \Omega/2\pi$ and integrating over a spherical volume with radius r [12]:

$$\bar{h}_{\mu\nu} = \frac{4e^{ikr}}{r} \int T_{\mu\nu} d^3x \quad (2.42)$$

where $k = \Omega/c$ ($k = \Omega$ in natural units).

The conservation law $\partial_\mu T^{\mu\nu} = 0$ can be used to show (for $\Omega \neq 0$) [12]:

$$\bar{h}^{\mu 0} = 0 \quad (2.43)$$

Schutz uses the tensor virial theorem to rewrite the spatial components of $\int T_{ij} d^3x$ [12]:

$$\int T_{ij} d^3x = \frac{1}{2} \frac{d^2}{dt^2} \int T_{00} x_i x_j d^3x \quad (2.44)$$

\bar{h}_{ij} can now be approximated as:

$$\bar{h}_{ij} = \frac{-2e^{ikr}}{r} \frac{d^2 I_{ij}}{dt^2} \quad (2.45)$$

where I_{ij} is the quadrupole moment tensor:

$$I_{ij} = \int T_{00} x_i x_j d^3x \quad (2.46)$$

See Schutz's textbook for the details of the derivation of these terms [12]. (2.43) and (2.45) approximate the equations for a GW of frequency $f = \Omega/2\pi$ in the slow-motion weak-field approximation.

If we move to a frame in the transverse traceless gauge with the wave moving in the z direction, the equations further simplify. Let \mathcal{I}_{ij} be the trace reduced quadrupole tensor:

$$\mathcal{I}_{ij} = I_{ij} - \frac{1}{3}\delta_{ij}I^k{}_k \quad (2.47)$$

\bar{h}_{ij} can now be written in the transverse-traceless gauge as:

$$\bar{h}_{zi}^{TT} = 0 \quad (2.48)$$

$$\bar{h}_{xx}^{TT} = -\bar{h}_{yy}^{TT} = -\Omega^2 (\mathcal{I}_{xx} - \mathcal{I}_{yy}) e^{ikr}/r \quad (2.49)$$

$$\bar{h}_{xy}^{TT} = \bar{h}_{yx}^{TT} = -2\Omega^2 \mathcal{I}_{xy} e^{ikr}/r \quad (2.50)$$

An interesting example of a quadrupole moment is the case of a binary neutron star system. Consider a system consisting of two stars of equal mass m and distance apart R . This system will have the following position equations in a coordinate system in which they are rotating in the x - y plane (making $I_{zj} = I_{jz} = 0$):

$$x_1(t) = \frac{1}{2}R \cos(\omega t + \phi_0) \quad (2.51)$$

$$x_2(t) = -x_1(t) \quad (2.52)$$

$$y_1(t) = \frac{1}{2}R \sin(\omega t + \phi_0) \quad (2.53)$$

$$y_2(t) = -y_1(t) \quad (2.54)$$

where $\omega = 2\pi f_{rot}$ and f_{rot} is the rotational frequency of the system and $x_1(t)$ and $x_2(t)$ are the positions of the center of mass of each star. In the slow motion approximation and treating the stars as idealized point particles, the equations for the reduced quadrupole moment tensor are:

$$\mathcal{I}_{xx} = mR^2 \left(\frac{1}{4} \cos(2\omega t + 2\phi_0) - \frac{1}{3} \right) \quad (2.55)$$

$$\mathcal{I}_{yy} = mR^2 \left(-\frac{1}{4} \cos(2\omega t + 2\phi_0) - \frac{1}{3} \right) \quad (2.56)$$

$$\mathcal{I}_{xy} = \mathcal{I}_{yx} = \frac{mR^2}{4} \sin(2\omega t + 2\phi_0) \quad (2.57)$$

From these equations, it is clear that the frequency of the emitted GWs is twice that of the rotational frequency of the system ($f = 2f_{rot}$ or $\Omega = 2\omega$). Using these equations along with (2.43), (2.48), (2.49) and (2.50) allows the computation of $h_{\mu\nu}$. Using the fact that in the transverse-traceless gauge $\bar{h}_{\mu\nu} = h_{\mu\nu}$ and absorbing the phase from e^{ikr} and $2\phi_0$ into a single phase factor ϕ , the non-zero components of $h_{\mu\nu}$ are:

$$h_+ = h_{xx}^{TT} = -h_{yy}^{TT} = \frac{-2\pi^2 f^2 m R^2}{r} \cos(2\pi f t + \phi) \quad (2.58)$$

$$h_\times = h_{xy}^{TT} = h_{yx}^{TT} = \frac{-2\pi^2 f^2 m R^2}{r} \sin(2\pi f t + \phi) \quad (2.59)$$

These equations describe circularly polarized GWs. If the stars had been rotating in a different plane, the polarization would have been different.

In a more general case, the stars are rotating around an axis in the x-z plane which makes an angle ι with the the z-axis. (2.51) and (2.53) become:

$$x_1(t) = \frac{\cos \iota}{2} R \cos(\omega t + \phi_0) \quad (2.60)$$

$$y_1(t) = \frac{1}{2}R \sin(\omega t + \phi_0) \quad (2.61)$$

The equations for the reduced quadrupole moment tensor components with x and y indices are:

$$\mathcal{I}_{xx} = mR^2 \cos^2 \iota \left(\frac{1}{4} \cos(2\omega t + 2\phi_0) - \frac{1}{3} \right) \quad (2.62)$$

$$\mathcal{I}_{yy} = mR^2 \left(-\frac{1}{4} \cos(2\omega t + 2\phi_0) - \frac{1}{3} \right) \quad (2.63)$$

$$\mathcal{I}_{xy} = \mathcal{I}_{yx} = \frac{mR^2 \cos \iota}{4} \sin(2\omega t + 2\phi_0) \quad (2.64)$$

The non-zero components of $h_{\mu\nu}$ are now:

$$h_+ = h_{xx}^{TT} = -h_{yy}^{TT} = \frac{-2\pi^2 f^2 m R^2}{r} \left(\frac{\cos^2 \iota + 1}{2} \right) \cos(2\pi f t + \phi) \quad (2.65)$$

$$h_\times = h_{xy}^{TT} = h_{yx}^{TT} = \frac{-2\pi^2 f^2 m R^2}{r} (\cos \iota) \sin(2\pi f t + \phi) \quad (2.66)$$

The angle ι between the axis of rotation and the z-axis affects the polarization and amplitude, describing circularly polarized GWs for $\iota = 0$ or $\iota = \pi$, and linearly polarized GWs for $\iota = \pi/2$.

2.5. Effect on Free Test Particles

A passing GW will change the proper distances between coordinates, changing the distance between two freely falling particles. One way to measure this would be to measure the distance between them with light. The square of the line element will first be considered:

$$ds^2 = g_{\mu\nu} dx^\mu dx^\nu \quad (2.67)$$

In transverse-traceless gauge:

$$ds^2 = -dt^2 + (1 + h_+)dx^2 + 2h_\times dx dy + (1 - h_+)dy^2 + dz^2 \quad (2.68)$$

For light this becomes:

$$ds^2 = 0 = -dt^2 + (1 + h_+)dx^2 + 2h_\times dx dy + (1 - h_+)dy^2 + dz^2 \quad (2.69)$$

$$dt^2 = (1 + h_+)dx^2 + 2h_\times dx dy + (1 - h_+)dy^2 + dz^2 \quad (2.70)$$

For a photon traveling along the x-axis, tangent to the direction of the plane gravitational wave, $dy = dz = 0$, giving:

$$dt^2 = (1 + h_+)dx^2 \quad (2.71)$$

$$\frac{dx}{dt} = \frac{1}{(1 + h_+)^{1/2}} \quad (2.72)$$

As Schutz notes, this is not equal to one (or c in other unit systems such as SI) [12].

The speed of light in vacuum is always $v = c = 1$, so this means the distance between spatial coordinates has changed. This change is what we want to measure.

Suppose there are two particles: one at $x = 0$ and one at $x = L$. The time it takes a photon to travel between the two coordinates is:

$$\int_{t_0}^t dt = \int_0^L (1 + h_+)^{1/2} dx \quad (2.73)$$

$$t - t_0 = \int_0^L (1 + h_+)^{1/2} dx \quad (2.74)$$

Since the value of $h_{\mu\nu}$ is small, the integrand can be expanded and all terms above linear order can be ignored:

$$t - t_0 = L + \int_0^L \frac{1}{2} h_+(t(x)) dx \quad (2.75)$$

In the case where the wavelength of a passing GW is long compared to the distance between the particles, $h_{\mu\nu}$ can be treated as constant:

$$t - t_0 = L + \frac{L}{2} h_+ \quad (2.76)$$

L is the distance between the points in their rest frame without a passing GW. The change in the distance ΔL is the remaining term:

$$\Delta L = \frac{L}{2} h_+ \quad (2.77)$$

$$\frac{\Delta L}{L} = \frac{h_+}{2} \quad (2.78)$$

A similar calculation can be done for h_{\times} . h_+ and h_{\times} are known as the gravitational “strains”. From these equations it is apparent that the strain can be measured by measuring the change in proper distance between the two particles. This can be done by measuring the time the photon takes to traverse the coordinates.

As will be discussed in Chapter III, the path difference of photons traveling through different arms of an interferometer can be measured by measuring the change in relative phase when they exit the interferometer. The difference in length between each arm is:

$$L_x - L_y = L + \frac{L}{2} h_+ - L + \frac{L}{2} h_+ \quad (2.79)$$

$$L_x - L_y = \frac{L}{2}h_+ + \frac{L}{2}h_+ \quad (2.80)$$

$$L_x - L_y = \frac{L}{2}h_+ + \frac{L}{2}h_+ \quad (2.81)$$

Dividing by L and putting this in terms of strain gives:

$$\frac{L_x - L_y}{L} = h_+ \quad (2.82)$$

$$\frac{L + \Delta L_x - L - \Delta L_y}{L} = h_+ \quad (2.83)$$

$$\frac{\Delta L_x - \Delta L_y}{L} = h_+ \quad (2.84)$$

This is the basic principle behind using laser interferometry to measure GWs.

CHAPTER III

INTERFEROMETRIC GRAVITATIONAL WAVE DETECTORS

LIGO consists of two observatories: the LIGO Hanford Observatory (LHO) in Hanford, Washington, and the LIGO Livingston Observatory (LLO) in Livingston, Louisiana. Each observatory operates a power-recycled Fabry-Perot Michelson interferometer with 4 km arms, referred to as H1 at LHO and L1 at LLO, which serve as GW detectors.

LIGO's initial detector configuration reached design sensitivity in 2005 during LIGO's fifth science run (S5) [16]. At this time, LHO also operated a second 2 km interferometer known as H2. After the completion of S5, LIGO received several upgrades which increased its sensitivity to higher frequencies (above 150 Hz) and allowed testing of several key systems in preparation for the 2nd generation detectors known as Advanced LIGO (aLIGO) [17, 18]. This upgraded configuration was known as Enhanced LIGO (eLIGO) and was used during LIGO's sixth science run (S6), the last science run before upgrades to the aLIGO configuration commenced [17, 18, 19]. S6 took place from July 7, 2009 to October 20, 2010 [19]. H2 was inactive during LIGO's S6 and the components that were to make up the mirrors of H2 in aLIGO have been put towards LIGO-India, a possible future LIGO detector to be constructed in India.

3.1. Detector Design

The LIGO interferometer design is based on the Michelson interferometer. The Michelson interferometer was originally invented in the late 1800s to confirm the existence of the luminiferous ether, a hypothesized fluid that physicists at that time

believed to be the medium through which light propagated [20]. It was designed to measure the difference in relative speed of light in perpendicular directions caused by the motion of Earth through this ether [20]. To detect this ether, the interferometer was rotated through a 90° angle. This rotation would change the number of wavelengths in each arm in the presence of an ether which would change the interference fringe in the output [20].

This first Michelson interferometer was plagued by noise [20]. It was so sensitive to vibrations that it could only be used at night for brief periods of time. It was eventually moved to a different location in a cellar, but even then, impacts on pavement 100 m away disturbed the apparatus [20]. There were also concerns about changes in the arm lengths due to small temperature differences. The device was returned to the manufacturer to improve the ease of rotation due to concerns that the arms were bending beyond acceptable limits when it was rotated during the experiment.

A few years later, a more sensitive version of the experiment was performed. Known as the Michelson-Morley experiment, it refuted the idea that the Earth moves through a stationary ether [21]. This experiment helped lead to our current concept of light and the understanding that light does not need a medium to propagate.

A Michelson interferometer functions by splitting light (in the case of LIGO, the beam from a laser) down two arms, where the light is reflected back, recombining at the beam splitter. A fraction of the recombined beam is directed onto a photodetector which measures the power of the beam (see Figure 3.1).

In 1969, Rainer Weiss proposed using the Michelson interferometer design as the basis for a GW detector [22]. The aim was to search for GW emissions from pulsars. He set the groundwork for the design of the interferometers used today, including using Fabry-Perot cavities in the arms to increase the effective length of the interferometer.

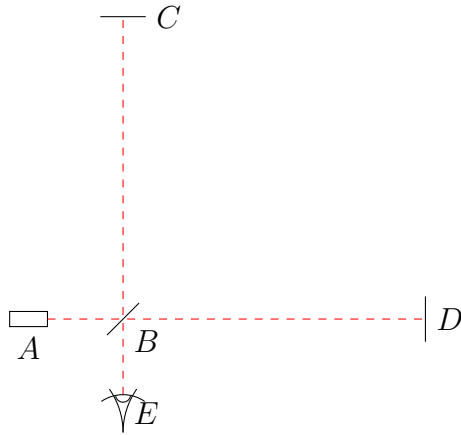


FIGURE 3.1. Pictured: A Michelson interferometer, which consists of (*A*) an input light source (in the Michelson-Morley experiment they used a sodium light for alignment and a white light for measurements), (*B*) a beam splitter, (*C*, *D*) two end mirrors and (*E*) a photodetector to detect the recombined light.

He also mapped out the noise sources that could be of concern and how to deal with them, including the use of a suspension system to isolate the detector from seismic noise.

The Michelson interferometer design was used as the basis for LIGO’s GW detector because the perpendicular arms would respond differently to changes in spacetime from a passing GW in most orientations, giving a direct measure of the induced strain (see Figure 3.2). The output beam intensity can be used as a measure of the difference in length of the interferometer arms: the intensity of the beam as measured by the photodetector is dependent on the relative phase of the two beams, which is dependent on the path length difference through the interferometer arms. A passing GW would alter the length of each arm differently, giving a direct measure of the strain from a passing GW through the path length difference.

The sensitivity of a basic Michelson interferometer can be increased by in several ways. As discussed in Section 2.5, the effect of the strain on the interferometer arms is directly related to their length ($h \propto \delta L/L$); therefore, an interferometer detector

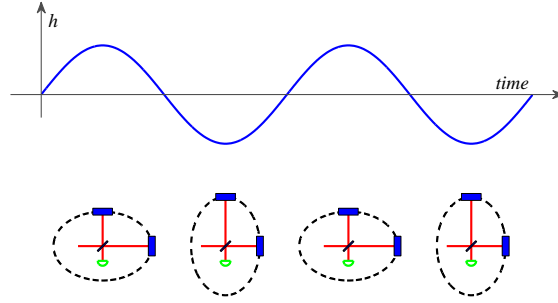


FIGURE 3.2. The distortion in spacetime from a passing GW affects the arms of a Michelson interferometer differently, allowing probing of the GW amplitude by measuring the change in the difference in arm lengths. Figure from [23].

with longer arms will be more sensitive to passing GWs. For this reason, LIGO's interferometer arms were constructed to be 4 km [23]. In addition to increasing the physical length of the arms, the effective arm length can be increased using Fabry-Perot cavities [24]. Increasing the laser power also increases the detector sensitivity. This is due to two reasons: 1) changes in length corresponding to larger changes in the output intensity of the beam and 2) the shot noise (see Section 3.2.3) is proportional to the square root of the power, causing the signal to noise ratio (SNR) to increase with the square root of the power in frequencies where shot noise dominates. The detector sensitivity can be improved by reducing the effect of noise on the detector, both external environmental noise as well as internal noise from the components of the detector itself. The external noise is reduced mainly by isolating the detector from the environment with the suspension. The internal noise is minimized with careful design of the internal parts. This modified detector is known as a power-recycled Fabry-Perot Michelson interferometer (see Figure 3.3). LIGO's targeted strain sensitivity was $\sim 10^{-21}$ [23]. For a distance of 4 km, that translates to 10^{-18} m, approximately 1000 times smaller than the diameter of a proton [23].

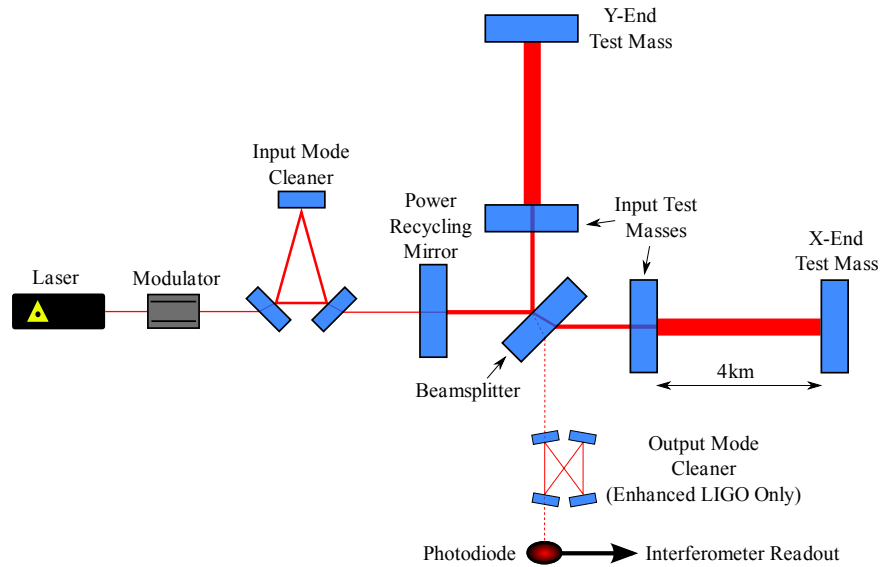


FIGURE 3.3. Simplified layout of the LIGO interferometer. The OMC was added for eLIGO in S6. Figure from [17].

3.1.1. Interferometer Mirrors

The main interferometer mirrors that were used in initial LIGO are made of a fused silica substrate in the form of 10.7 kg cylinders [17, 23]. They are covered with thin films formed of quarter wavelength layers of dielectric materials to control the reflectivity and transparency of the mirrors and other desired properties, controlling the properties of the different cavities such as the finesse of the Fabry-Perot cavities. The mirrors are designed to minimize thermal noise. The mirrors are also known as “test masses” as they are used to probe changes in spacetime due to passing GWs.

3.1.2. Vacuum System

Each of the test masses and the arms are contained in an ultra-high vacuum of $\sim 10^{-9}$ Torr in order to minimize noise from laser scattering from gas in the beam path. The beam paths of the interferometer are enclosed in 4 km welded steel tubes

which function as an ultra-high vacuum system. Each of the test masses, as well as components such as the output mode cleaner, are contained in independently controlled vacuum chambers which can be brought to atmospheric pressure, allowing maintenance and commissioning work, and then pumped back to vacuum again for detector operation.

3.1.3. Fabry-Perot Cavities

The base design of the Michelson interferometer is modified by the addition of a Fabry-Perot cavity in each arm in order to increase the detector sensitivity (see Figure 3.4). The resonance of the cavity is determined by the distance between the two mirrors. Fabry-Perot cavities can be characterized by their finesse (\mathcal{F}), a measure of the sensitivity of the cavity to changes in the cavity length or the wavelength of light [24]. The finesse can be represented in terms of the reflectivities of the input mirror (r_i) and the end mirror (r_o) of the cavity [24]:

$$\mathcal{F} = \frac{\pi\sqrt{r_i r_o}}{1 - r_i r_o} \quad (3.1)$$

Each arm of the LIGO interferometers contain a Fabry-Perot arm cavity which is 3995 m in length [23, 25]. The Fabry-Perot cavities increase the effective interferometer arm length by a factor of ~ 100 for a 100 Hz signal [23]. The finesse of the arm cavities in initial and Enhanced LIGO was 220, and in aLIGO is 450 [23, 26]. The cavity is formed by adding mirrors, the Input Test Masses (ITMs), after the beam splitter and forming a cavity with the mirrors at the ends of the interferometer arms, the End Test Masses (ETMs). The reflectivities of the ITMs and ETMs determine the behavior of

the cavity. Since LIGO’s ETMs have higher reflectivity than its ITMs, the majority of the power is sent back towards the beam splitter [24].

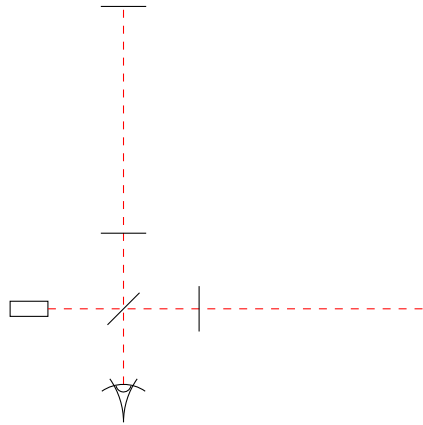


FIGURE 3.4. Modified Michelson Interferometer with Fabry-Perot Cavities.

3.1.4. Laser Power and the Power Recycling Cavity

As laser power increases, output power increases, leading to an improved sensitivity in measuring the difference in arm lengths. Increasing the power also has the effect of reducing the shot noise in comparison to the output signal (see Section 3.2.3 for shot noise). The power in the arm cavities can be increased by directly increasing the power of the laser. An additional method to increase the power is to install a mirror between the beam splitter and input laser to act as a power recycling mirror. When properly positioned, this mirror will return nearly all of the laser power headed back to the laser to the rest of the interferometer (see Figure 3.5). The Power Recycling Cavity (PRC) is the cavity formed by the power recycling mirror and the ITMs.

Initial LIGO used a 10 W 1064 nm Nd:YAG laser [23]. For S6, the laser power was increased to 30–35 W to improve the sensitivity above 150 Hz by lowering the limit from shot noise [17]. The laser power was increased by installing new Master Oscillator/Power Amplifiers (MOPAs) in the 4 km detectors in Hanford and Livingston

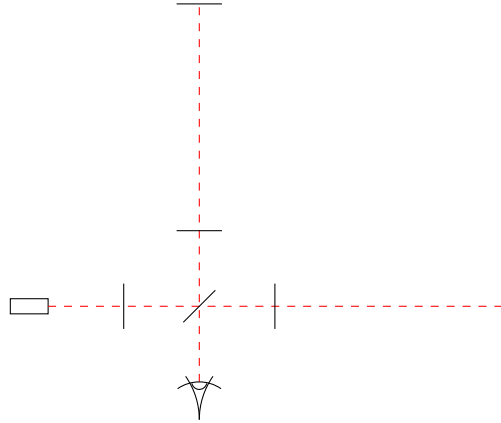


FIGURE 3.5. Power Recycled Modified Michelson Interferometer with Fabry-Perot Cavities.

which provided 30-35 W in the TEM_{00} mode (also referred to as the Gaussian spatial mode) [18]. More robust modulators and Faraday isolators were installed to help handle the higher power [17]. A more powerful CO_2 laser system was used to counteract increased deformation in the test masses due to thermal heating from the more powerful laser (see Section 3.1.8) [17].

3.1.5. Detector Readout

Before S6, an RF readout configuration was used in which the laser was set to destructive interference at the photodetector to make the detector insensitive to changes in laser power and avoid laser power noise from coupling to the output beam [24]. However, in a simple Michelson interferometer, this reduces sensitivity to the strain to second order. In order to get a linear response to the strain, the input laser is modulated to produce RF sidebands [23]. The sidebands from the GW modulation would produce power variations in the RF sidebands [16]. Allowing the sidebands to reach the photodetectors while suppressing the carrier requires a macroscopic difference

in the arm lengths known as the Schnupp asymmetry [24]. Initial and enhanced LIGO had a Schnupp asymmetry of 355 mm [16].

For S6, the detector readout was upgraded to a DC readout configuration in which the carrier is slightly shifted off a dark fringe and changes in DARM result in changes in the laser power at the photodetectors [16, 17]. A potential drawback of the DC readout implementation is that by allowing the carrier through, there is now noise dependent on laser power fluctuations [27]. This requires a laser with low noise. The signal response is not completely linear, as the operating point is on the near-quadratic slope close to the dark fringe [27]. If the mean deviation from this operation point is not too large, this is not a problem. A DC readout configuration provides a fundamental increase in the SNR by a factor of $\sqrt{3/2}$ compared to an RF readout configuration for the same laser power at frequencies limited by shot noise [16]. In the DC readout configuration, the PRC and arm cavities act as a filter and reduce the coupling of noise in the input beam to the detector readout [16].

In eLIGO, the shift off the dark fringe was provided by a small offset of ~ 10 pm in DARM, providing ~ 30 – 100 mW of power [16]. The offset was optimized to remain as small as possible (as noise coupling increases with a larger offset) while still being large enough to exceed the RMS residual arm motion and produce enough power so the contrast defect is negligible, and the shot noise exceeds the electronics noise of the readout [16].

3.1.6. Input Mode Cleaner

After the RF sidebands are added, the input laser passes through the input mode cleaner (IMC) before entering the interferometer. The IMC stabilized the position, pointing and frequency and removed higher order spatial modes of the laser so that

the laser light which entered the interferometer was 1064 nm in a TEM₀₀ Gaussian spatial mode [17]. The IMC is a triangular cavity made from three mirrors, with a total path length of 24 m [17].

3.1.7. Output Mode Cleaner

The output mode cleaner (OMC), which was added in S6 and was a prototype for aLIGO, filters the output signal before it hits the photodetectors. The output mode cleaner is in vacuum to minimize noise and consists of four mirrors in a “bow-tie” configuration [17, 18]. The interferometer is designed to function with a pure gaussian spatial mode; as such, the input mode cleaner reduced higher order modes of the laser before input into the detector [16]. However, imperfections in the detector optics produce additional power in these higher order modes, which provide no information and add additional shot noise [16]. The output mode cleaner was installed to help mitigate these effects by filtering out the higher order spatial modes of the laser after it passes through the interferometer [16]. The OMC also filters out the RF sidebands from the output signal as they are still present to measure degrees of freedom in the detector other than DARM, but would only add noise to the signal [16].

3.1.8. Thermal Compensation System

The Thermal Compensation System (TCS) uses a CO₂ laser system to counteract the thermal lensing of the test masses due to excess heat from the main laser [28]. The power recycling mirror was designed with a radius of curvature to match the effective curvature of the ITMs when they were heated with an input laser power of 6 W; however, the thermal lens of the ITMs is dependent on the absorption in the substrates and coatings, which are “poorly controlled parameters” [28]. H1 reached

the desired operating point at 2.5 W while H2 and L1 did not reach it with the full 6 W. Although the thermal lenses did not affect the main carrier, they did affect the sidebands, diminishing the sensitivity of the detector. To compensate for this effect, CO₂ lasers were directed onto the ITMs. The lasers can be set to a Gaussian mode to increase the lensing or to an annulus or ring mode to decrease the lensing as needed [28].

With the increased laser power used in eLIGO, thermal lensing due to heat absorption from the laser increased [18]. TCS used an 8 W CO₂ laser, which was not powerful enough to compensate for the additional thermal lensing; therefore, TCS was upgraded to use a CO₂ laser capable of 20 W of power to counteract the larger thermal lensing.

3.1.9. Suspension

The suspensions reduce the effect of external environmental noise on the detector. Each of the main mirrors in the beam line were suspended by a loop of steel wire, forming a single pendulum which isolated the mirror by a factor of f^{-2} (nearly 2×10^4 at 100 Hz along the beam direction) [23]. Four electromagnetic actuators controlled the orientation and position for each of the main optics, which further isolated the detector output from external noise and kept the detector at a stable operating point [17, 23]. The actuators consisted of a permanent magnet attached to the mirror and an electromagnetic coil attached to a support structure [23]. Optical sensors in the actuators measured the mirror's position with respect to the support structure [23]. The pendulums were mounted to a four layer mass-spring stack which reduced the noise by approximately f^{-8} above ~ 10 Hz (isolating by $\sim 10^8$ at 10 Hz) [23]. The single pendulum and passive isolation stack were in vacuum and attached to tubes which

exit the vacuum and connected to an external active seismic isolation system [29]. Feed-forward signals from external seismometers were sent to the external actuation system to reduce noise due to ground motion [29]. See Figure 3.6 for an overview schematic of the suspensions.

Due to the higher than expected noise at LLO, the development of the external active isolation system was sped up [30]. LLO had higher microseismic and anthropogenic noise than LHO in the 0.1–0.5 Hz and 1–10 Hz bands. Resonances in the passive isolation stack amplified external noise in the 1–3 Hz band which caused problems for Livingston [30]. A piezoelectric actuation system, called piezoelectric pre-isolation (PEPI), was used in both Livingston and Hanford and could actuate in the beam direction up to $\pm 90 \mu\text{m}$ [30]. Between the third and fourth science runs, LLO was upgraded with a hydraulic actuation system called hydraulic external pre-isolation (HEPI), that could actuate in 6 degrees of freedom with a larger actuation range of $\pm 700 \mu\text{m}$ [29].

In S6, the feed-forward subtraction scheme was improved by using the signals from multiple seismometers along with Weiner filtering in the noise subtraction process [29]. The active isolation system was effective at reducing the detector coupling to low frequency ground motion, with a reduction in the microseismic peaks up to a factor of ~ 5 and an overall reduction in the RMS motion by a factor of ~ 2 [29].

The suspension of the output mode cleaner consisted of a double pendulum and a one-stage active isolation system, both of which were prototypes for aLIGO subsystems [17].

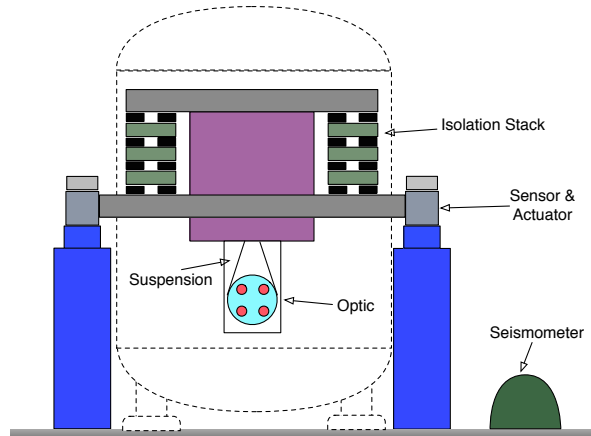


FIGURE 3.6. Schematic of suspension used in LIGO. The optic is suspended by a steel wire from a passive isolation stack. Four electromagnetic actuators control the orientation and position of the optic. Feed-forward signals from external seismometers are applied using the external actuators (HEPI at LLO and PEPI at LHO) to counteract some of the low frequency ground motion. The vacuum chamber is the dashed line. Figure is from [29].

3.2. Noise Limits

The sensitivity of LIGO is limited by contamination of the data by noise. Figure 3.7 shows “typical” amplitude spectral densities (ASDs) for the Hanford and Livingston LIGO detectors during S6 [19]. The major contribution to noise below 40 Hz in LIGO during S6 was seismic noise from sources such as earthquakes and anthropogenic noise such as highway traffic and construction [19]. Noise in the 50–150 Hz band had significant contributions from Brownian motion, thermally excited motion in the suspensions and test masses [19]. Photon shot noise was the main noise source above 150 Hz [19, 24].

In addition to these broadband sources, narrow band noise peaks and short duration transient noise events known as glitches affected GW searches by lowering their sensitivity [19]. Glitches affected short duration searches for GW bursts and

compact binary coalescences, while spectral lines and other long term noise artifacts affected the longer duration stochastic and continuous wave searches [19].

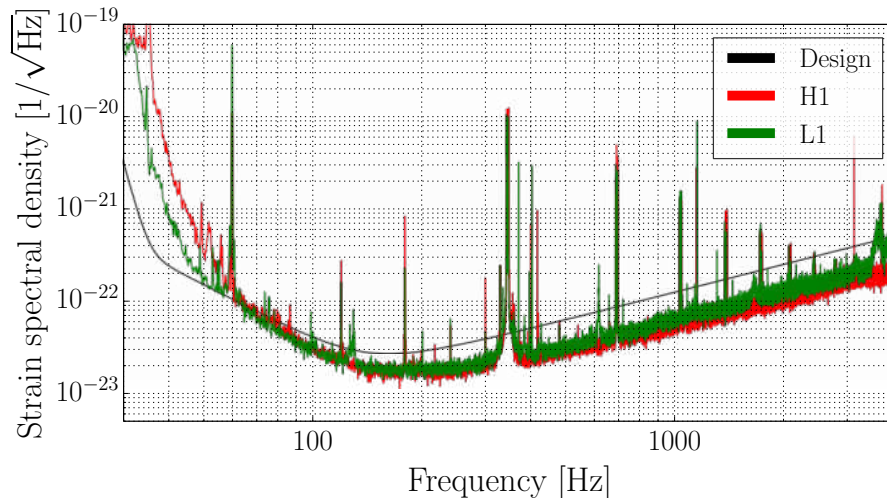


FIGURE 3.7. A normal strain ASD for H1 and L1 in S6. Figure from [19].

3.2.1. Seismic Noise

LIGO was limited below 40 Hz by seismic noise [19, 31]. This included ground motion caused by earthquakes, wind, ocean waves and anthropogenic noise. Earthquakes contributed noise in the 0.03–0.1 Hz band, and in higher frequencies the closer they were to a detector [31]. Noise from wind contributed mostly to the 0.5–15 Hz band and could knock the detector out of lock when wind speeds were above 10–20 miles per hour due to the induced swaying of the buildings housing the detectors [31]. Noise from human related activity varied significantly between day and night and included logging, construction and ground and air traffic [31]. Vehicular traffic from highways produced noise in the 2–15 Hz band [31]. Ocean waves contributed to seismic noise in the 0.07–0.7 Hz band; with the highest contribution at twice their propagation frequency [31]. They contributed a problematic large peak at 0.1–0.3 Hz

[29]. The noise due to ocean activity can vary up to two orders of magnitude in just a few days [31]. The passive isolation systems are not effective at attenuating the noise at these lower frequencies, requiring an active feed-forward system to reduce the lower frequency noise as described in Section 3.1.9 [31].

In addition to limiting the sensitivity below 40 Hz, seismic noise was also upconverted into broadband noise in higher frequencies, causing drops in sensitivity in LIGO’s most sensitive band [19]. High seismic noise was linked to increases in noise in the 40–200 Hz band [19]. This noise was termed seismic upconversion and thought to be due to Barkhausen noise (see Chapter IV).

3.2.2. Thermal Noise

Noise in the 50–150 Hz band had major contributions from Brownian motion from thermal excitations in the test masses and the suspensions [19]. Some noise sources in this band were never identified [19]. The suspensions and the test masses were designed so that the resonances were outside of the LIGO sensitivity band “as much as possible” [23]. This mitigated most of the thermal noise that would otherwise limit the detector sensitivity; however, there was still some thermal noise in the detection band which was dependent on the mechanical dissipation of the components [23].

The fused silica substrate of the test masses had a very low mechanical loss and contributed very little thermal noise outside of its resonant frequencies [23]. The main contribution of thermal noise from the test masses came from the thin films, which had a relatively high mechanical loss. This concentrated the dissipation on the mirror surface interacting with the laser [23]. The thermal noise in the suspension wires is proportional to the radius of the wire to the fourth power [23]. The wires were constructed of steel and fabricated with a small radius to minimize the thermal noise

while still retaining enough strength to support the test masses. A diameter of 300 μm allowed the steel loops to support the 10 kg test masses at 30% of their breaking stress [23].

3.2.3. Shot Noise

Shot noise, described by Poisson statistics, is a statistical effect caused by the quantum nature of light and is the dominant noise source above 150 Hz [19, 23]. The ideal limit to the strain spectral density due to shot noise for the LIGO interferometers is [23]:

$$\tilde{h}(f) = \sqrt{\frac{\pi \hbar \lambda}{\eta P_{\text{BS}} c} \frac{\sqrt{1 + (4\pi f \tau_s)^2}}{4\pi \tau_s}} \quad (3.2)$$

In this equation c is the speed of light, \hbar is the reduced Planck constant, η is the quantum efficiency of the photodetector, τ_s is arm cavity storage time, P_{BS} is the power incident on the beam splitter and f is the frequency of a passing GW.

Shot noise is proportional to the square root of the power of the laser. As the power of a laser rises, the shot noise will rise as the square root of that power; therefore, the SNR improves with the square root of the power. While this would seem to support making the laser as powerful as possible, radiation pressure becomes a limiting factor with higher power. Larger test masses could be used to help mitigate noise from radiation pressure. aLIGO is using 40 kg test masses which can cope with the increased radiation pressure from higher laser power [8, 26].

3.2.4. Spectral Lines

LIGO's sensitivity was limited in specific frequency ranges by narrow band noise structures. The United States power grid and the electronics in the observatories produced large spectral lines at 60 Hz, and at some of the 60 Hz harmonics [19]. The

60 Hz line is close to the frequency of possible continuous GWs from the Crab pulsar, which would be emitted at 59.6 Hz [31]. Fluctuations in the current broadened the width of the 60 Hz line, limiting the detector sensitivity to the Crab pulsar [31].

3.3. Potential Gravitational Wave Sources

LIGO is potentially sensitive to four main types of sources: 1) short lived and known (compact binary coalescences); 2) short lived and unknown (GW bursts); 3) long lived and known (continuous waves); and 4) long lived and unknown (stochastic) [8]. Compact binary coalescences (CBCs) include binary neutron stars (BNSs), neutron star black hole binaries (NSBHs) and binary black holes (BBHs). GW bursts could come from events such as core-collapse supernovae, gamma ray bursts (GRBs) or non-radial modes in neutron stars. LIGO is expected to be sensitive to continuous waves (CWs) emitted from rapidly spinning neutron stars. A stochastic GW background could come from sources such as mergers of very distant neutron stars, cosmic strings and primordial waves from the Big Bang.

3.3.1. Compact Binary Coalescences

GWs from CBCs can be considered the best case scenario for detection by LIGO. A binary system is effectively a large mass quadrupole, which is ideal for GW emission.

CBCs consist of three stages: the inspiral, the merger and the ringdown [8]. The inspiral is expected to be well described by post-Newtonian calculations. The merger stage is considered to begin after the “innermost stable circular orbit” after which the two objects “plunge together” to form a black hole [8]. Numerical relativity is required to calculate the waveform during the merger stage due to strong effects from general relativity [8]. In the S6 high mass search, the merger stage was approximated

with analytic effective one body solutions guided by numerical relativity simulations [32, 33]. In the ringdown, oscillations of the resulting black hole emit GWs whose frequency and damping time are determined by the black hole’s mass and angular momentum [8].

Since inspirals and ringdowns are thought to be well described by calculated waveforms, matched filtering is the optimal search method [23]. Waveforms covering the desired parameter space of mass combinations are generated in frequency space and used in a “template bank” [23]. Each waveform in the template bank is used to filter the data in frequency space using a noise weighted convolution of the waveform with a time segment of the detector data stream [34]:

$$z(t) = 4 \int_0^\infty \frac{\tilde{h}(f)^* \tilde{s}(f)}{S_n(f)} e^{2\pi i f t} df \quad (3.3)$$

$$\sigma^2 = 4 \int_0^\infty \frac{\tilde{h}(f)^* \tilde{h}(f)}{S_n(f)} df \quad (3.4)$$

$\tilde{h}(f)$ is the Fourier transform of the template waveform, $\tilde{s}(f)$ is the Fourier transform of the data and S_n is the noise power spectral density. The SNR (ρ) is defined as $\rho(t) = |z(t)| / \sigma$.

If a waveform in the template bank returns an SNR above a given threshold, it is categorized as a trigger and is checked for coincidence with triggers in the other active detectors [34]. At least one other detector must be active and the triggers must be within the light speed travel time of the involved detectors (≤ 10 ms for H1 and L1). The mass components of the triggered waveforms must agree within a certain allowable difference. Having more templates ensures a higher probability of recovering the signal with less loss of SNR. The computational cost of additional templates must be balanced against the SNR loss for using less templates [23]. Templates are

chosen at discrete points in the mass range such that the maximum loss of SNR is 3% [23, 32, 35].

Both BNS and NSBH inspirals could be the central engines powering short GRBs [8, 36]. GWs associated with GRBs could provide information on the GRB trigger mechanism.

GWs from CBCs involving neutron stars could provide information on the neutron star equation of state [8]. In NSBH binaries, tidal disruption of the neutron star in the final stages of collapse could provide detailed information on the neutron star equation of state and structure [36].

GWs from CBCs offer a potential “standard candle” independent of Type 1A supernovae with which cosmological distances could be determined and verified [8]. The waveform could determine the distance to the source, thus providing an independent measure of the Hubble constant. The redshift of the GW can affect the distance estimate through its affect on the GW waveform. This can be compensated for with estimates of the redshift of the host galaxy, or if the CBC involves a neutron star the tidal disruption may help determine the redshift through determination of the stellar mass in its local frame.

During S6, LIGO’s range for GWs from BNS inspirals averaged over sky position and orientation was ~ 20 Mpc for LHO and LLO [19]. aLIGO’s range is expected to be ~ 200 Mpc at design sensitivity [37]. In aLIGO, a two detector network will have a sky localization of thousands of square degrees in some directions. Three detectors of similar sensitivity provide a sky localization of ~ 5 – 20 square degrees for many directions, and the planned LIGO-India detector would improve the localization to an order of a few square degrees [37].

aLIGO is projected to reach a sensitivity similar to design sensitivity after 2019, with Advanced Virgo to follow a few years later, with an expected detection rate of BNS inspirals of 0.2–200 per year [37]. During or after 2022, LIGO-India may be incorporated into the detector network, improving the expected detection rate to 0.4–400 BNS inspirals per year.

3.3.2. Gravitational Wave Bursts

GW bursts are short-duration transient GWs thought to be generated from violent astrophysical events. Possible astrophysical sources of bursts include core-collapse supernovae, cosmic string cusps, magnetars, pulsar glitches and GRBs [38]. GWs can only be emitted from events that are not perfectly spherically symmetric. For example, observations of many pulsars with high speeds relative to their neighbors lead to speculation that some supernovae have a substantial non-spherical component which could emit GWs [8].

The expected waveforms for GW bursts are often poorly constrained or completely unknown; therefore, search methods other than matched filtering are used. One is the excess power method [39]:

$$\mathcal{E} = 4 \sum_{k_1 \leq k \leq k_2} |\tilde{h}_k|^2 / S_k \quad (3.5)$$

In this equation, $|\tilde{h}_k|^2$ is summed over a given frequency band and time duration and is weighted by an averaged noise spectral density S_k . This statistic adds up the excess power for a given frequency band and time duration. Thresholds are set choosing a false alarm rate based on the background calculated by analyzing time shifted data. Other search methods include cross correlation or cross coherence [23].

In addition to combining the search data in a given time and frequency band, clustering algorithms can be used to combine the data in different ways, often based

on rules of grouping together values for specific time frequency combinations above a determined threshold.

Burst searches are either all-sky or targeted. All-sky searches use multiple time shifts to target different points throughout the sky. Targeted searches use information from electromagnetic observations to provide a specific sky direction to search for a GW, increasing their sensitivity over all-sky searches [23]. Targeted searches can be used to search for GWs coincident with supernovae, GRBs or other electromagnetically observed events.

3.3.3. Continuous Waves

LIGO is sensitive to frequencies in which rapidly rotating neutron stars are thought to generate continuous waves. Possible mechanisms which could generate GWs include non-axisymmetry due to residual deformation of the crust, non-axisymmetric magnetic field energy, normal oscillation modes such as r-modes (where the emission is due to quadrupole mass currents) and non-isotropic accretion in a binary system with a neutron star [8, 40]. In a neutron star with a strong magnetic field, the magnetic axis may not be aligned with the rotation axis, causing magnetic pressure distortions making the neutron star asymmetric [41]. A neutron star's rotation axis may not align with the moment of inertia tensor's principal axis, causing the neutron star to precess and emit GWs [41].

The mass quadrupole of an asymmetric rotating neutron star would generate GWs at twice the rotation frequency [42]. The GWs would be modulated by the Earth's motion (including both its daily rotation and its orbit around the sun) [43, 44]. GWs from a neutron star in a binary system would also be modulated by that system's

rotation. Changes in rotational frequency such as those observed in pulsars over time would also change the GW emission frequency [42].

Known pulsars can be ideal targets [42]. Regular observation with electromagnetic detectors can determine the frequency evolution of the star, allowing GW data to be coherently integrated over months or even years [42]. It should be noted that uncertainties in the electromagnetic and possible GW emission mechanisms leave the possibility open that the the GW frequency is not exactly twice the observed rotation frequency [40]. For example, if the main GW emission mechanism is in the core instead of the crust and the core and crust rotate at different frequencies, then a search assuming a GW frequency from the crust would assume the wrong frequency [40].

Low-mass X-ray binaries (LMXBs) are another interesting source. LMXBs are observed to be clustered in a particular band of frequencies ($270 \text{ Hz} \leq \nu_S \leq 620 \text{ Hz}$) [45]. One possible explanation is that the spin-up from the accretion disk is balanced by the spin-down from GW emission. This allows the GW strength to be estimated by relating the X-ray flux to GW emission ($h \propto (F_X/\nu_S)^{1/2}$ for X-ray flux F_X and spin frequency ν_S). The source known as Scorpius X-1 would be of particular interest as it would be the most luminous GW source of the LMXBs. Electromagnetic observations have been used to estimate an indirect upper limit on the GW emission from Scorpius X-1 of $h_0^{EQ} \approx 3.5 \times 10^{-26} \left(\frac{300 \text{ Hz}}{\nu_S} \right)^{1/2}$.

3.3.4. Stochastic

A stochastic GW background would be generated from the superposition of many unknown cosmological and/or astrophysical sources [8, 23, 46]. Cosmological stochastic GWs are expected to carry the earliest detectable information about the universe

[47]. Cosmological sources of GWs may include vacuum fluctuations amplified during inflation or in “pre-big-bang models” and cosmic strings formed from “phase transitions in the early universe” [23]. The predicted strength of cosmological waves varies greatly [8]. Predictions from standard inflation would be far below the detectable range of aLIGO, although there are some pre-big-bang models which could be probed [8]. Astrophysical sources may dominate the LIGO and Virgo bands and include distant CBCs, supernovae, magnetars and rotating neutron stars [46]. Other possible sources include mergers of supermassive black holes; however, those GWs would be in the frequency range of space based detectors [8].

To find a stochastic signal, data are cross-correlated from two or more detectors [48]. As the integration time grows, a common GW signal would increase with the integration time (T), while uncorrelated noise would increase with \sqrt{T} . This causes the SNR for a common signal to grow with \sqrt{T} , allowing detection of signals buried in the noise for sufficiently long integration times.

This method relies on the assumption of an absence of significant correlated noise between the detectors. Large separations between detectors is integral to removing correlated noise. The Schumann resonance from lightning strikes is an example of a correlated noise source that could still contaminate distant detectors, and may prove a problem in aLIGO (the Schumann resonance was below the detection threshold in initial LIGO). Magnetometers are used to monitor for correlations in this specific case. The detector separation, while reducing the correlated noise, also reduces the sensitivity as “physically-separated detectors respond at different times to GWs from different directions and with differing response amplitudes depending on the relative orientation and (mis)alignment of the detectors” [48]. The loss of sensitivity can be

described by an “overlap reduction function” [23]. The overlap reduction function averaged ~ 0.1 for LHO and LLO in their sensitive frequency band around 100 Hz [23].

CHAPTER IV

SEISMIC UPCONVERSION

In early LIGO science runs, increases in seismic noise below 10 Hz were linked to decreases in detector sensitivity in the 40–200 Hz band, LIGO’s most sensitive band (see Figure 3.7) [19]. This noise, called seismic upconversion, was often a limiting factor of the sensitivity in this frequency band during S6.

Investigations found that reductions in range in this band were more closely correlated with the currents in the test mass actuators than directly with low seismic noise or test mass motion [19]. Upconversion noise bursts were found to occur during times of “high slope in the amplitude of the magnetic actuator current” (see Figure 4.1) [19]. This was evidence that the culprit was Barkhausen noise.

Barkhausen noise comes from fluctuations in the magnetic field from sudden discontinuous jumps in the sizes and orientations of magnetic domains in a ferromagnet as an externally applied magnetic field changes [19]. This can produce avalanching, where a group of nearby domains rearrange and change orientation in quick succession at the influence of neighboring domains.

A succession of experiments has led to the conclusion that it was likely the cold worked steel in the test mass actuators that was the source of seismic upconversion noise [49]. Figure 4.2 is a schematic of the test mass suspension showing the location of the test mass actuators. It was originally thought seismic upconversion was due to Barkhausen noise in the NbFeB magnets attached to the test masses [19, 50]. Switching out the NbFeB magnets with less noisy SmCo magnets was unsuccessful in significantly reducing seismic upconversion noise [19]. Investigations in S6 by Robert Schofield found that parts in the test mass actuators were ferromagnetic and possibly

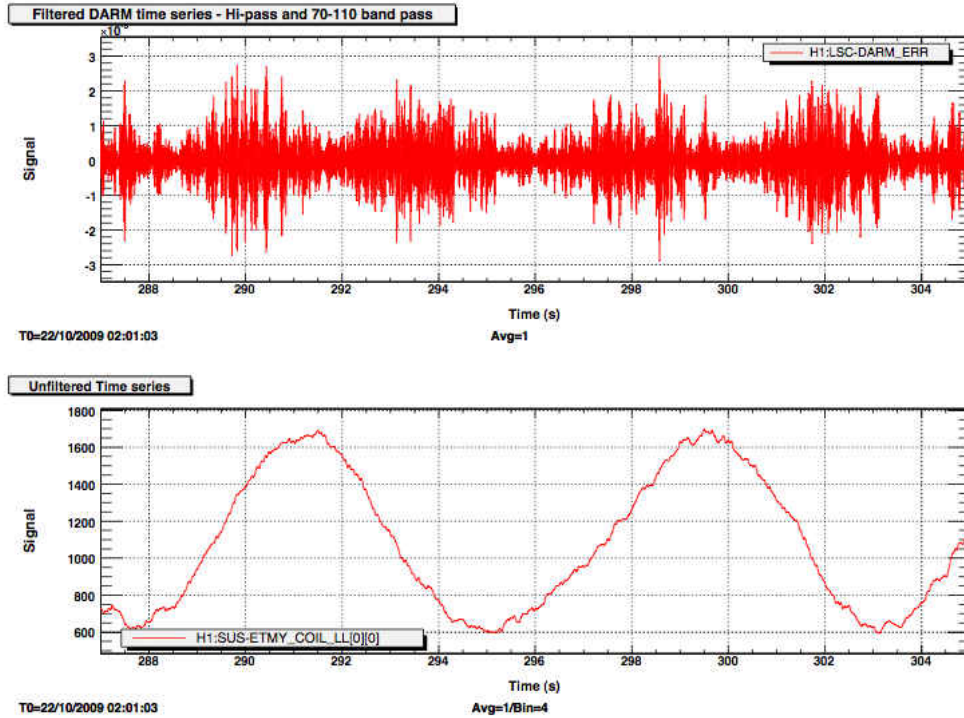


FIGURE 4.1. Upconversion noise and actuator coil current. The top is a plot of the DARM time series in the 70–110 Hz band. The bottom is the coil current amplitude of one of the actuators. The noise in this band of DARM occurs during times of high slope in the amplitude of the magnetic actuator current. Figure from [49].

the source of seismic upconversion due to Barkhausen noise [49]. Parts made of 303 steel in the actuators had become ferromagnetic, likely due to cold working. In aLIGO, the parts in the “most sensitive locations” are made of 316 steel, “which is much less ferromagnetic after cold working”, to help mitigate any possible seismic upconversion [19].

4.1. Monitoring Upconversion

In LIGO’s fifth science run Masahiro Ito, a former UO graduate student, used the current through the electromagnets of the test mass actuators to monitor seismic

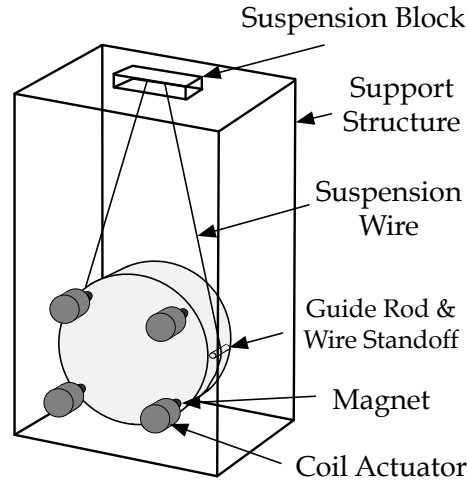


FIGURE 4.2. A schematic of the optic suspension during initial LIGO. The magnetic actuators act on magnets secured to the test mass. Figure from [25].

upconversion noise and predict times when seismic upconversion noise was likely high [51]. He calculated an empirical function to predict the probable seismic upconversion noise in the detector GW signal output (or detector strain).

This work was continued for S6 [52]. The S5 weighting function for the Hanford detector was used to monitor upconversion at LHO, and a new weighting function for the Livingston detector was calculated to monitor upconversion at LLO. These weighting functions were empirically determined and used to predict how noise in the actuator coil current would convert to higher frequency noise in the main detector channel.

4.1.1. Correlating with Noise

To identify seismic upconversion, the band limited root mean square (BLRMS) of a frequency band in the coil current is calculated, squared, and plotted against the square of the BLRMS (BLRMS^2) of a frequency band in the strain to check for a

correlation (see Figure 4.3). If the noise in the coil current is increasing noise in the strain, the strain BLRMS^2 will be proportional to the coil current BLRMS^2 .

LIGO has multiple noise sources, and excess noise from sources other than seismic upconversion will cause points to lie above the correlation line between strain and coil current. In Figure 4.3, this can be seen by the many points in the upper left portion of the plot. To account for this, a “minimal bound” can be constructed by taking the lowest strain noise values for a set of coil current BLRMS^2 values. This minimal bound describes the expected noise due to seismic upconversion if the detector is at its best performance and all other noise sources are relatively quiet (the noise due to upconversion plus other noise at optimal levels). Points above this minimal bound would be due to seismic upconversion plus other excess noise sources.

The procedure to find the minimal bound relating a coil current frequency band to a strain frequency band is the following:

1. Break time series data into time segments of a certain length (in our case we used 40 s intervals) and Fourier transform each segment.
2. Calculate the power spectral density (PSD) and sum the data in each segment that is within the band of interest and take the square root to calculate the BLRMS in that band for that time segment. The start time of each time interval is recorded as the time value for each BLRMS data point.
3. Plot the data with strain BLRMS^2 on the Y axis and coil current BLRMS^2 on the X axis.
4. Bin the X axis (20 equal bins were used) and take the data point with the lowest Y value from each bin. The X value is take as the midpoint of each bin.

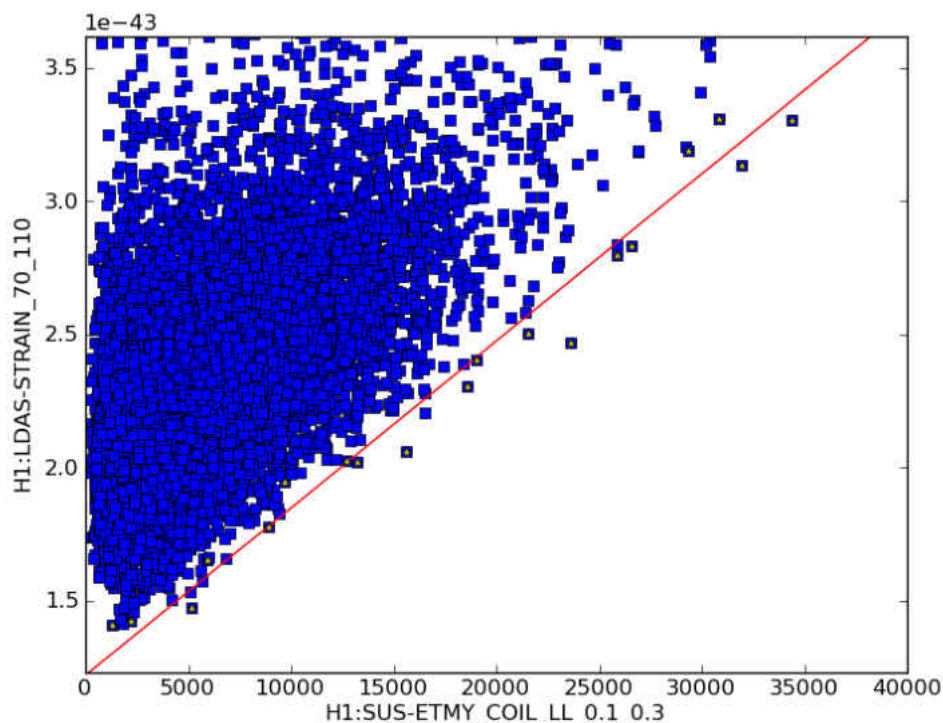


FIGURE 4.3. Test mass actuator coil current BLRMS^2 (0.1–0.3 Hz band) versus detector strain BLRMS^2 (70–110 Hz band) for a time during S6 with very clear seismic upconversion.

5. Fit the minima previously found with a linear line. This line is the minimal bound on the expected strain noise for a given value of the coil current noise.

This same procedure can also be used to find correlations between the strain (or other data output) and other noise sources. If the minimal bound has a significant slope with a good fit, then some kind of upconversion-like noise is likely. A program designed to automate the analysis of multiple bands and channels for upconversion-like noise was originally written by Ryan Quitzow-James and further developed by Vincent Roma. This program has been in use looking at data from aLIGO to monitor upconversion-like noise.

4.1.2. Weighting Functions

The weighting functions were used to predict the noise due to seismic upconversion in the strain. To make a weighting function, the minimal bounds were calculated for bands in the actuator coil current comparing each one to the 70–110 Hz band in the detector strain. The bands of interest in the actuator coil currents were identified by Masahiro Ito during S5 as 0.1–0.3 Hz, 1.0–1.6 Hz, 1.8–2.6 Hz, 5–7 Hz, 10–13 Hz and 17–19 Hz. These same bands were used for S6. The Livingston weighting function was created using the following procedure:

1. Calculate BLRMS^2 for 40 s long non-overlapping time intervals. Plot coil current BLRMS^2 against strain BLRMS^2 for times during S6 when data for both exist.
2. Bin data into 20 equal bins along the coil current axis. Pick the point with the minimum strain BLRMS^2 value in each bin.
3. Find the continuous science segment each minimum point belongs to and calculate the minimal bound for that time interval.
4. Repeat the above steps for each coil current band.
5. Create a plot using the data calculated in the previous steps with the central frequency of each band on the X axis and associated slopes of each minimal bound on the Y axis.
6. Find the weighting function by fitting the points on the plot with a power-law (or fitting sub sets of them as is the case with the Livingston weighting function). Multiple power-law fits can be used for adjacent sets of bands if appropriate.

Masahiro Ito determined that the power-law fit was significantly different above and below 10 Hz when calculating the Hanford weighting function and used two power-

laws, one to fit the points below 10 Hz, and one to fit the points above. This example was followed when calculating the Livingston weighting function.

When calculating the Livingston weighting function, there was a wide variation of slope values, with many clustered near the minimum for each band (similar to Figure 4.4). Outliers in the BLRMS² plots skewed some of the slopes to larger values. Some of the outliers were likely due to excess noise before the detector became unstable and dropped out of science mode.

For each coil current band, a subset of slope values which were grouped together near the minimum slope value was chosen by hand. These were used to fit the power curve. In the future, a programatic and/or statistical method can be used. Some possible methods that have been tested include not counting bins with less than 10 points when calculating the minimal bound, and removing 1–5% of the points with the highest coil current BLRMS² before calculating the minimal bound to remove the outliers. Tests so far have successfully removed the high slope values seen in Figure 4.4, including the points in the middle of the Y axis, and left just the values clustered at the lower Y axis. Figure 4.5 shows a weighting function calculated with this method using Hanford data (and the points used to calculate it) along with the Hanford and Livingston weighting functions.

4.1.3. Flagging Seismic Upconversion

The likely source of seismic upconversion was found during the later part of S6, but it could not be mitigated during the run by changing the hardware [49]. The next best option was to provide lists of times of high upconversion that may impact searches [19]. Times not on this list would likely have low seismic upconversion noise. These lists of times with high upconversion were known as upconversion flags.

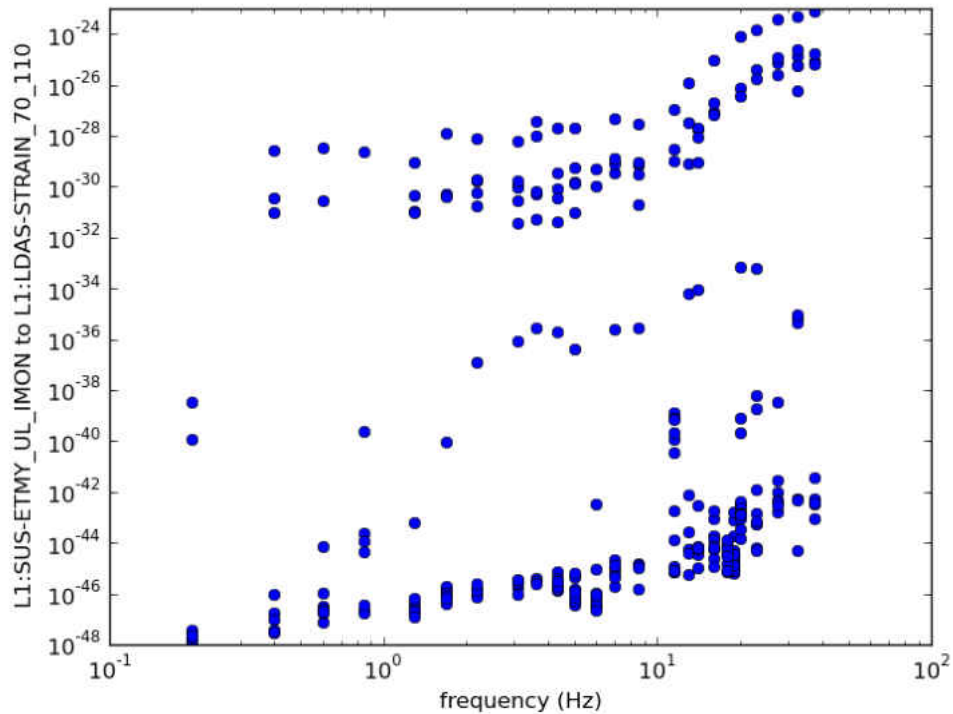


FIGURE 4.4. Minimal bound slopes plotted against frequency. This was a test looking at many bands. Outliers cause the minimal bound fit to produce high slopes.

Flags for S6 were created for H1. Coil current data was not available prior to December 11, 2009, 23:56:19 UTC for the Livingston detector, so flags for S6 were created for L1 from this time onward.

The procedure for creating lists of flags is the following:

1. Calculate the PSD for each consecutive 40 s interval of data and scale by the weighting function before summing between the frequencies of interest (0.1–40 Hz) and taking the square root to get a “weighted” BLRMS for each time.
2. Flag segments of time for which this weighted BLRMS is above the chosen threshold.

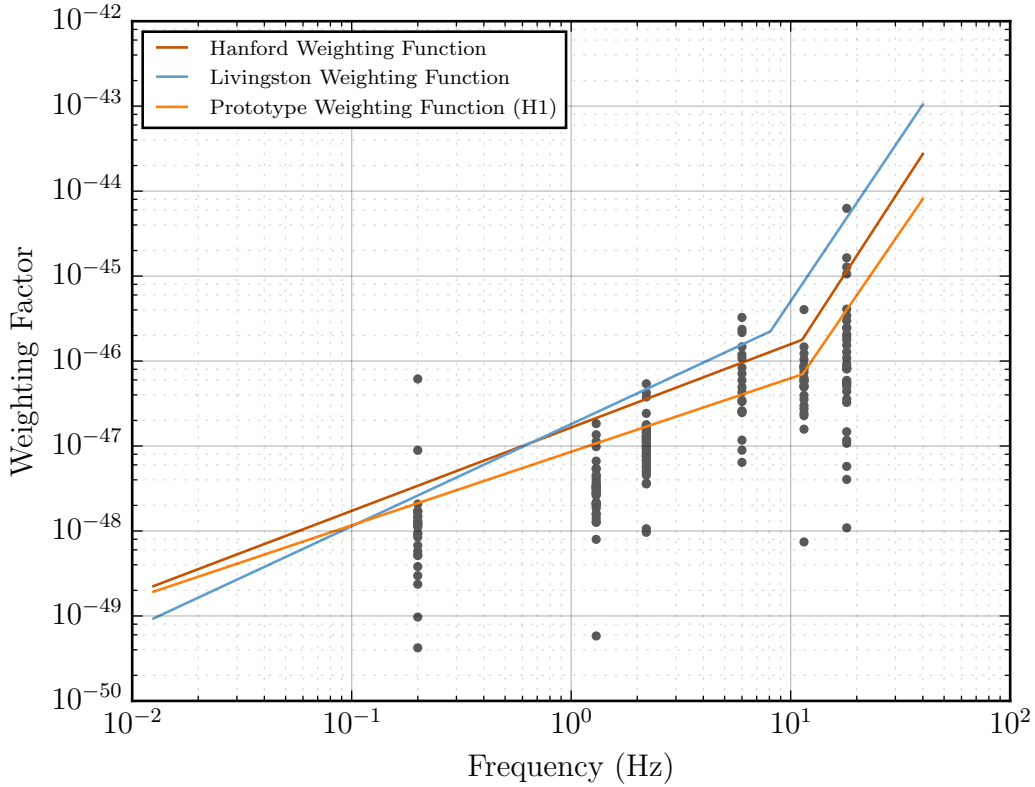


FIGURE 4.5. H1 and L1 weighting functions plotted with a test weighting function calculated for H1 and fit to the grey points. The y-axis is the weighting factor from coil current BLRMS^2 to strain BLRMS^2 . The outliers were reduced before calculating the minimal bounds by removing a small percentage of the loudest points in the coil current and requiring a minimum of 10 points in each bin.

Masahiro’s weighting function was used for H1 during S6, and the weighting function we calculated for Livingston was used for L1 when coil current data was available.

Upconversion flags were calculated for S6 using multiple thresholds, which are summarized in Table 4.1. H1 and L1 flags use the same set of thresholds. Each flag includes all times with predicted seismic upconversion above the associated threshold. The times with the lowest upconversion can be identified by their lack of any upconversion flags.

Threshold	Percent Time Flagged (H1)	Percent Time Flagged (L1)
1.35×10^{-22}	79.59%	75.39%
1.7×10^{-22}	49.36%	40.82%
2.5×10^{-22}	13.84%	14.33%
2.8×10^{-22}	8.43%	11.16%
3.3×10^{-22}	3.9%	5.26%
3.6×10^{-22}	2.59%	2.85%
4.4×10^{-22}	0.99%	0.55%
6.5×10^{-22}	0.11%	0.039%
9×10^{-22}	0.0097%	0.0088%

TABLE 4.1. Weighted coil current thresholds chosen for flags and the fraction of time during S6 that is flagged for each threshold.

The flags constructed from the weighted coil current threshold of 4.4×10^{-22} were chosen by the LIGO Detector Characterization group as a useful flag for data quality¹. A study by Jessica McIver found these flags vetoed a significant amount of low-SNR glitches while flagging less than 1% of observational data [53]. They were classified such that they could be checked against possible GW bursts if found by analysis of the detector output.

4.2. Range Predictor

The inspiral range of the detectors can vary significantly, and sometimes the source of the range drop is unknown. After creating the flags for H1 and L1, a “range predictor” was created to track when decreases in the range of the estimated binary neutron star (BNS) inspiral sensitivity during S6 were likely due to seismic upconversion as opposed to other processes [54]. A range predictor was made for H1 by plotting the average BNS inspiral sensitivity against the weighted coil current. The

¹The coil currents were measured in counts, which the weighting function converts to the unit of strain (which is unitless). Since the weighted coil current is the square root of the sum of the predicted strain noise power within a band, the weighted coil current is also unitless.

laser power was not always in high power mode during S6. The range predictor was made only from data when the laser was in the high power 20 W mode. The range predictor found increased seismic upconversion was correlated with drops in the BNS inspiral range during S6 (see Figure 4.6).

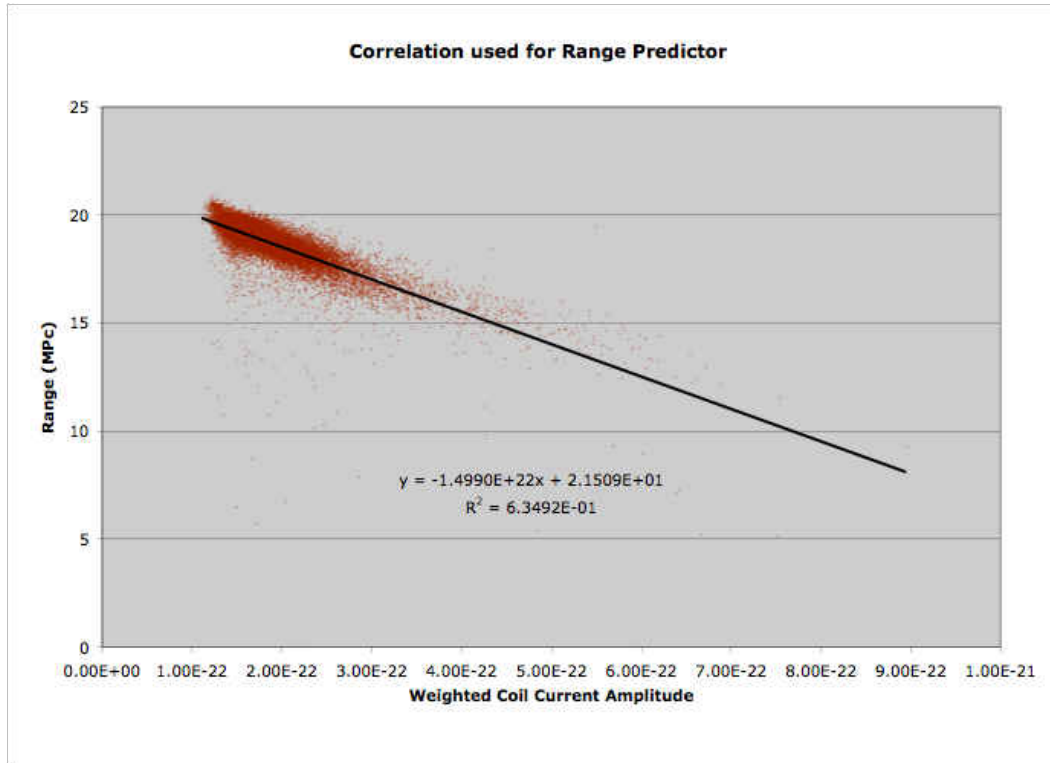


FIGURE 4.6. Weighted coil current is correlated with drops in the BNS range.

The range predictor was also used to verify that upconversion was responsible for a drop in range and not an additional problem with the interferometer. Figure 4.7 plots the predicted and actual BNS inspiral range for H1 from May 29, 2010, through July 11, 2010. The reduction in range matched the predicted range, and was also coincident with an increase in the McNary Dam overflow. This is taken as evidence that the drop in range was due to seismic upconversion caused by the seasonal increase in the McNary Dam overflow.

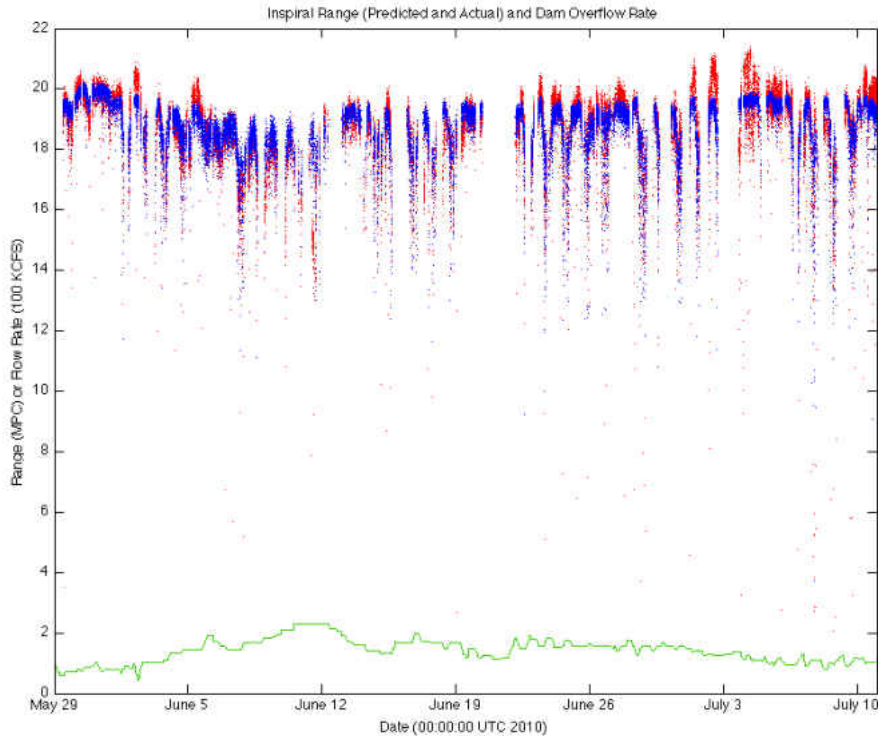


FIGURE 4.7. Seasonal increase in seismic upconversion due to McNary Dam overflow. The predicted (blue points) and actual (red points) BNS inspiral ranges are shown from May 29, 2010, through July 11, 2010. The drop in range matches predictions, as well as an increase in the McNary Dam overflow (green line). This is taken as evidence that the drop in range was due to seismic upconversion, which itself was increased by the seasonal increase in the McNary Dam overflow. Figure from [54].

4.3. Correlation with Low-Frequency Low-SNR Glitches

This study broke S6 into 40s time intervals and compared the number short duration transient noise events (glitches) in each interval to the weighted coil current BLRMS of that interval. The number of glitches was correlated with the weighted coil current amplitude. Glitches were then broken down into groups based on SNR and central frequency of their most significant time-frequency pixel to find which glitches were related to seismic upconversion.

For glitches at all frequencies with $\text{SNR} > 10$, there was no correlation with seismic upconversion [55, 56]. Similarly, when compared to glitches of all SNR with frequencies above the expected seismic upconversion band, frequencies above 200 Hz, there was no correlation. For glitches with $\text{SNR} < 10$ and frequencies of 0–70 Hz there was a correlation with weighted coil current. This is not surprising since the main noise source below 40 Hz is seismic noise. In the 110–200 Hz band, glitches with $\text{SNR} < 10$ were also correlated with seismic upconversion. The strongest correlation was to glitches in the 70–110 Hz band with $\text{SNR} < 10$ (see Figure 4.8).

All glitches in this study had a minimum SNR of 4.5. Subgroups of the 4.5–10 SNR group suggest there may be stronger correlations for the lower SNR glitches within that group. It is possible that glitches with even lower SNR could have had similar or even stronger correlations with seismic upconversion [55]. Initial results show the louder glitches in the 4.5–10 SNR group are less strongly correlated (but still correlated) than the middle and lower SNR glitches in that group.

This investigation found that low-frequency low-SNR glitches were correlated with seismic upconversion and supports the idea that these glitches were produced by seismic upconversion.

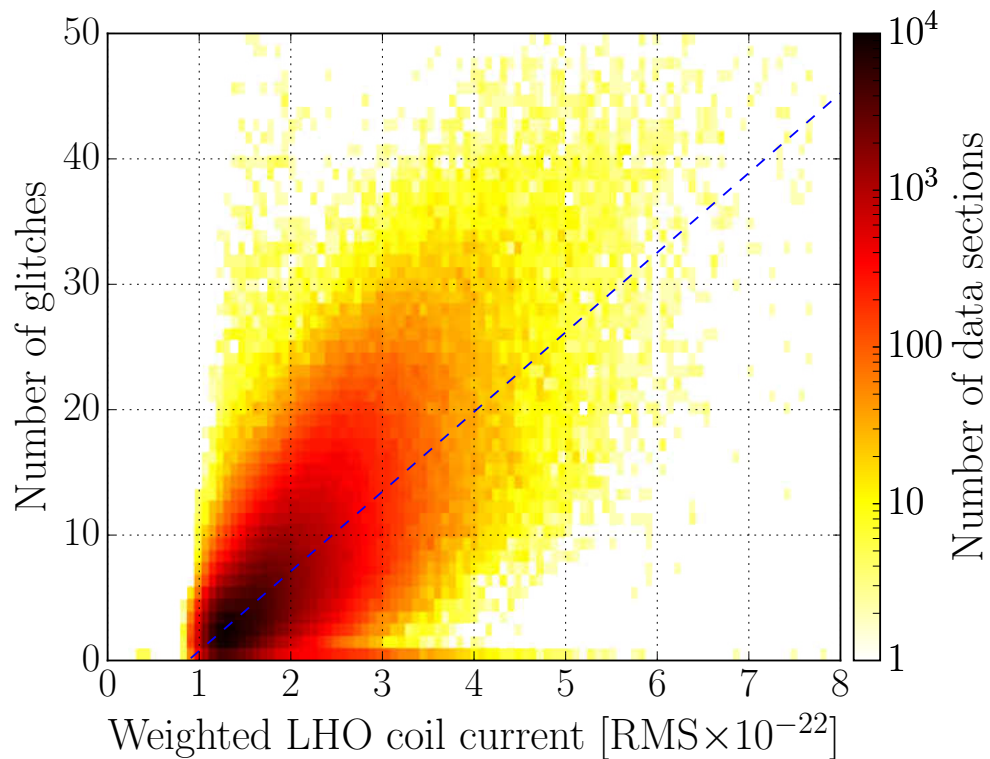


FIGURE 4.8. Low-frequency low-SNR glitches and seismic upconversion. The weighted coil current is correlated with glitches in the GW output with an SNR between 4.5 and 10 and in the 70–110 Hz band. The line represents the correlation through a least-squared fit. Figure from [19].

CHAPTER V

ASTROPHYSICS OF MAGNETARS

Soft gamma repeaters (SGRs) and anomalous X-ray pulsars (AXPs) are astronomical objects that emit intermittent bursts of X-rays and gamma-rays. The slow spin period and lack of partner objects are some of the observations that lead observers to suspect these objects are highly magnetized neutron stars, or magnetars, whose very strong magnetic field powers these bursts. The magnetic fields of magnetars are much stronger than the quantum critical value at which the energy separating Landau levels is equal to the rest mass of electrons ($B_{QED} = \frac{m^2 c^2}{\hbar e} = 4.4 \times 10^{13}$ gauss) [57]. These strong magnetic fields may provide an energy reservoir than can power GWs during and immediately after bursts and giant flares. Searches for GWs from magnetars were performed on S5 data as well as data surrounding the 2004 giant flare [58, 59].

5.1. Soft Gamma Repeaters and Anomalous X-Ray Pulsars

5.1.1. Soft Gamma Repeaters

On January 7, 1979, satellites observed the first detected SGR burst [60]. The burst was emitted from SGR 1806-20 in the Sagittarius constellation [60]. Two months later, on March 5, 1979, a much more powerful burst was detected from SGR 0526-66 [59, 60]. It was the most luminous extra-solar burst of gamma-rays detected at the time and the first giant flare observed [60]. More detections of SGR bursts would follow, including three more starting just nine days later from a third source object, leading to the realization of a new class of astronomical event [60].

Initially, these bursts could not be definitively differentiated from GRBs [61]. In 1987, these repeating bursts were recognized as a distinct class of event from GRBs [60]. The source objects were called soft gamma repeaters (SGRs), named for the sporadically repeating nature of the bursts and the spectrally soft photons when compared with GRBs [9, 60].

SGRs are astronomical objects which release intermittent bursts of hard X-rays and soft gamma rays. Hard X-rays have energies above 10 keV [57]. The burst emissions extend up into the “few hundred keV energy band” which consists of hard X-rays/soft gamma rays [62]. These bursts can be classified into three general types: short bursts (with isotropic energies up to 10^{41} erg), intermediate bursts (with isotropic energies of 10^{41} – 10^{43} erg) and rarer, more energetic bursts known as giant flares (with isotropic energies of 10^{44} – 10^{46} erg) [62]. Isotropic energy is the estimated energy assuming uniform energy emission in all directions.

5.1.2. Anomalous X-Ray Pulsars

When first observed, AXPs were originally thought to be X-ray pulsars. X-ray pulsars are a subclass of X-ray binaries, which are made up of a donor object and a white dwarf, neutron star or black hole. In an X-ray binary, matter from the donor object accretes onto the compact object, emitting X-ray radiation as a result of the accreting matter’s gravitational energy converting into kinetic energy [63]. In the case of a neutron star with a strong magnetic field ($\sim 10^{12}$ gauss), the accreting matter is guided by the magnetic field lines into matter columns falling onto the magnetic poles [63]. If the magnetic field axis and rotational field axis are not aligned, there is a pulsation in the X-ray radiation at the rotation frequency of the neutron star, and the X-ray binary appears as an X-ray pulsar [63].

Several characteristics of AXPs were observed that did not fit with the X-ray pulsar model [57]. The distribution of the spin periods was recognized to be narrow (2–12 s as opposed to a range of milliseconds to hours in X-ray pulsars), leading to the recognition of the existence of a different type of object. The periodic pulsations of AXPs allowed searches for orbital Doppler modulation, the lack of which put stringent upper limits on the size of potential companion stars.

Optical and infrared searches found counterparts for approximately one third of SGRs and AXPs, and candidate counterparts for a few of the other SGRs and AXPs [9]. The counterparts and candidate counterparts were very faint, excluding the presence of bright companion stars and ruling out accretion in a binary system as the source of the X-ray radiation [57]. The lack of partner object distinguished these objects from the normal X-ray pulsars and led to these objects being classified as “anomalous” X-ray pulsars (AXPs), astronomical objects which emit persistent periodically varying X-rays, but lack the partner object associated with X-ray pulsars.

When persistent X-ray emission was discovered from SGRs, the emission shared properties with those seen from AXPs; similar periods, period derivatives and X-ray luminosities (but with harder spectra) were observed pointing to a possible link between these objects [57]. The magnetar model, originally designed to explain the observations from SGRs, was applied to AXPs, explaining the persistent X-ray luminosity that could not be powered by rotational energy loss or accretion from a binary [57]. The discovery of short bursts from AXPs confirmed the connection to SGRs and supported the application of the magnetar model to AXPs [57].

5.1.3. Transient Magnetars

Transient magnetars are magnetars whose X-ray luminosity is usually at a much fainter quiescent level, and have outbursts lasting weeks or months where their luminosity increases to the level of “constant” magnetars [9]. During such outbursts they will emit short bursts like other magnetars. No bursts have been seen from transient magnetars during quiescent luminosity levels. Transient magnetars are a clear example that there may be more undetected magnetars, showing that the magnetar birthrate may be higher than previously thought.

5.2. Electromagnetic Emission from SGRs and AXPs

Electromagnetic emissions from SGRs and AXPs have been observed at many wavelengths and include both long term persistent emission and shorter sudden bursts of hard X-rays and soft gamma-rays. Persistent X-ray emission has been seen in both SGRs and AXPs and is too luminous to be powered by the rotational energy loss which powers radio pulsars [57, 62]. Optical and infrared observations of SGRs and AXPs have ruled out accretion from a binary companion as a possible energy source [57, 62]. Originally thought to be radio silent, radio emissions were detected from transient magnetars [62]. The radio emissions were highly variable, possibly associated with outbursts, with properties very different from those seen from radio pulsars [62].

5.2.1. Short Bursts

Short bursts have been observed in both SGRs and AXPs, usually lasting $\sim 0.1\text{--}1$ s with energies up to 10^{41} erg and peak luminosities that can reach 10^{41} erg/s assuming isotropic energy emission [62]. The burst luminosities are often above the classical Eddington limit ($\sim 2 \times 10^{38}$ erg/s for a neutron star without a magnetic field) [62, 64].

The Eddington limit is the maximum luminosity a star can have before photon pressure is expected to overcome the gravitational potential and start pushing mass off of the star.

Observations have found that both the wait times between bursts and the intensities of individual bursts have log-normal distributions, and the bursts are not correlated with any particular phase of the magnetar's rotation [57]. There is no correlation between the wait time before a burst and the burst's intensity [57]. Burst durations are correlated with fluence (the total energy emitted per surface area at the point of observation) [62]. A few bursts have shown tails that lasted $\sim 100\text{--}1000$ s [62]. Wait times between bursts can be years, although there may be bursts just under the detection threshold during quiet times as bursts intensities are detected right up to the threshold [62]. Burst wait times can also be very short, with some remarkable events known as burst storms in which tens to hundreds of bursts occur within a few hours in rapid succession with a rise in emission [62].

5.2.2. Intermediate Bursts

Intermediate bursts have energies in the range $10^{41}\text{--}10^{43}$ erg, with peak luminosities of $10^{41}\text{--}10^{43}$ erg/s, well above the Eddington limit [62]. They last $\sim 1\text{--}40$ s and have been seen in both AXPs and SGRs. The initial burst seems to be a brighter, longer version of short bursts, and are often, but not always, followed by a long tail (containing less than 2% of the energy in the initial spike) which is modulated at the neutron star's rotation period and can last up to several thousand seconds [62]. The strongest intermediate burst occurred on April 18, 2001, from SGR 1900+14 [64]. It had no initial peak and a slow rise time of ~ 10 s, lasting ~ 40 s with pulsations at the

neutron star’s rotational frequency [57, 62]. Some intermediate bursts have precursors, and short bursts have been detected during some of the tails [62].

5.2.3. Giant Flares

In addition to the regular and intermediate bursts, three bursts with estimated isotropic energies greater than 10^{44} erg known as giant flares have been observed from SGRs. The first of these rare events was detected on March 5, 1979, from SGR 0526-66, the same year SGRs were first detected [59, 60]. It had a total estimated isotropic energy of $\sim 1.2 \times 10^{44} \left(\frac{d}{15 \text{ kpc}}\right)^2$ erg ($\sim 1.5 \times 10^{45}$ erg at the estimated distance of 53.6 kpc) [59, 65]. The second giant flare was detected on August 27, 1998 from SGR 1900+14 and had a total estimated isotropic energy of $\sim 4.3 \times 10^{44} \left(\frac{d}{15 \text{ kpc}}\right)^2$ erg ($\sim 3 \times 10^{44}$ erg at the estimated distance of 12.5 kpc) [59, 64, 65]. The third giant flare was detected on December 27, 2004, from SGR 1806-20 (see Figure 5.1 for a plot of the time series data from the event) [57, 66]. It had a total estimated isotropic energy of $\sim 5 \times 10^{46} \left(\frac{d}{15 \text{ kpc}}\right)^2$ erg ($\sim 1.7 \times 10^{46}$ erg at the estimated distance of 8.7 kpc) [59, 65]. The sources for these giant flares are the three SGRs with the strongest estimated magnetic fields [65].

Giant flares are characterized by an initial spike with luminosities up to 10^{47} erg/s lasting less than a second, followed by an afterglow lasting several hundred seconds [62]. Turolla et al. pointed out that none of the giant flares were “caught during pointed observations”; this means the detector sensitivity to the giant flare tails was much lower than for some of the intermediate flares, and that this constraint should be considered when “comparing the apparent durations” [62]. In all three cases, the tail was present and was modulated by the rotation period of the neutron star [57].

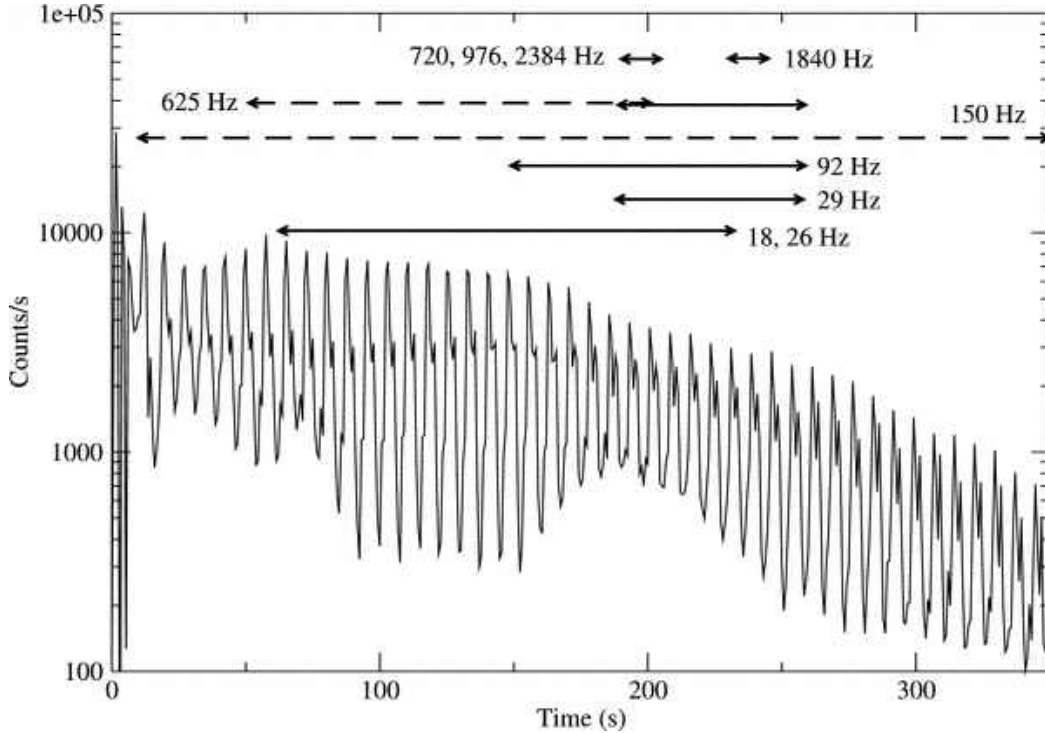


FIGURE 5.1. Time series of data of the 2004 giant flare from SGR 1806-20. Initial peak followed by X-ray tail. Large modulations in the tail are due to the magnetar’s rotation. Solid lines and dashed lines indicate detection of QPOs at different phases of the rotation. Figure from [67].

It is thought that a giant flare stems from a sudden release of energy, with the initial spike coming from an escaping relativistically expanding electron-positron plasma and the long tail coming from energy radiating from an electron-positron pair fireball trapped in the magnetosphere [57]. The energy content of the tails for all three flares was similar ($\sim 10^{44}$ erg) [62]. If the tail is due to a fireball trapped by a magnetic field, this requires a magnetic field of $\sim 10^{14}$ gauss [57].

In the giant flare from SGR 1806-20, an increase in hard X-rays was observed after the end of the pulsating tail, peaking ~ 700 s after the giant flare’s start and lasting about one hour [57]. Radio afterglows were detected after the giant flares from both SGR 1900+14 and SGR 1806-20 [62]. This is thought to come from expanding

magnetic fields and shocked plasma which were ejected from the magnetar during the burst, the linear polarization suggesting electron synchrotron emission [62]. In these two giant flares, higher frequency components known as quasiperiodic oscillations (QPOs) were detected (see Section 5.2.5) [57].

Precursors to the 1998 and 2004 giant flares were observed [62]. A precursor resembling a short burst occurred less than a second before the onset of the 1998 giant flare [62]. If there was a similar precursor to the 1979 giant flare, it would not have been detectable by instruments at the time [62]. The precursor to the 2004 giant flare was in the energy range of an intermediate burst and occurred 142 s before the flare [62].

It is possible that some gamma-ray bursts may be giant flares from distant magnetars outside our galaxy. The energetic initial peak of a giant flare could appear as a short GRB [62]. It has been suggested that giant flares with 10^{44} erg could be detected from a few Mpc, and giant flares of 10^{46} erg could be detected from as far away as the Virgo cluster [62]. So far, no evidence of excess GRBs has been detected in the direction of nearby galaxies or the Virgo cluster [62]. This means at most $\sim 8\%$ of the short GRBs observed by BATSE could be giant flares outside our galaxy [62].

Two events that may have been extragalactic giant flares are GRB 070201 and GRB 051103. GRB 070201 was coincident with the spiral arms of the Andromeda galaxy (M31) [68]. At the distance of 0.77 Mpc, observations with the LIGO detectors ruled out a BNS or NSBH merger with greater than 99% confidence [68]. If the source object was at this distance, the estimated isotropic electromagnetic energy was 10^{45} erg, consistent with the energy of a magnetar giant flare [68]. GRB 051103 was coincident with the M81 spiral galaxy at a distance of 3.6 Mpc [69]. At this distance, observations from the LIGO detectors excluded BNS mergers with 98% confidence

and NSBH mergers with greater than 99% confidence [69]. If the source was in M81, the isotropic electromagnetic energy was $\sim 3.6 \times 10^{46}$ erg, the same order of the energy in the 2004 giant flare. This would be the furthest SGR observed as of 2012 [69].

5.2.4. Persistent X-Ray Emission

Originally seen in AXPs, persistent X-ray emission has been detected in some SGRs as well. The X-ray luminosities are more than what can be powered by rotational energy loss from the spin-down, with typical luminosities for AXPs of 10^{34-36} erg/s depending on the distance estimates [57, 62]. It is thought the X-ray luminosity is powered by twists in the magnetosphere, created from the transfer of helicity from a strong internal field with toroidal components to the external field (possibly cracking and twisting the neutron star crust in the process) [62].

The X-ray emission spectra from AXPs are generally fit by a combination of thermal blackbody and power-law, and in a few specific cases are fit equally well with two blackbodies or other combinations of two spectral components [57]. There appear to be blackbody components in the X-ray emission spectra of SGRs when high quality spectra are available [57]. The tails could be due to resonant cyclotron scattering which distorts the thermal spectrum: in a strong magnetic field with local variations permeated by electrons, resonant scattering would give rise to a hard tail instead of narrow lines [62]. However, Mereghetti et al. caution this may instead reflect a more complex thermal model rather than a distinct physical process [9].

5.2.5. Quasiperiodic Oscillations

Quasiperiodic oscillations (QPOs) were first observed in the tail of the giant flare from SGR 1806-20 (see Figure 5.1) [57]. One was detected at 92.5 Hz for a 50 s interval,

and two other oscillations were detected at 18 Hz and 30 Hz with less significance [57]. Further analysis and observations from additional satellites confirmed the 92.5 Hz and 18 Hz QPOs and revealed additional QPOs up to 1,840 Hz, with lower significance QPOs as high as 2,384 Hz [57]. Data from the giant flare from SGR 1900+14 was analyzed and QPOs were found at 28 Hz, 54 Hz, 84 Hz, and 155 Hz [57]. Mereghetti speculates that “hint for a 43 Hz periodicity” in the giant flare from SGR 0526-66 in 1979 was likely a QPO as well [57]. More recently it is thought that analysis of at least one burst event has revealed the probable existence of QPOs in a non-giant flare burst, showing that QPOs are not limited to giant flares. A common property of QPOs is they each occur at a particular phase of the rotation [57].

Robert C. Duncan predicted that magnetars may experience global seismic oscillations from crustquakes driving the bursts [70]. He hypothesized that such an oscillation could have caused the 43 Hz oscillation in the 1979 giant flare peak [70]. Torsional modes would likely be the easiest oscillations to excite as they are purely shear deformations and wouldn't change the shape of the star, while other modes would involve compression and vertical motion of the dense matter which would require much more energy [70]. Global seismic oscillations from crustquakes are still the most plausible explanation for QPOs, and would mean QPOs could help constrain properties of magnetars, including the strength of the interior field and possibly even the equation of state [62].

5.3. The Magnetar Model

When first proposed, the magnetar model was created to explain the observations from SGRs, and was specifically motivated to explain the unique observations of the March 5, 1979 giant flare [71]. An emission line consistent with a redshifted

pair-annihilation line from a neutron star surface observed in the spectrum of the giant flare combined with a sky position suggesting an association with a supernova remnant in the Large Magellanic Cloud were taken as evidence for a neutron star [71]. The X-ray tail of this giant flare was modulated with a period of ~ 8 s [71]. This was most easily explained as the rotation of the source object, and taken with the previous evidence suggested the presence of a slowly rotating neutron star.

The age of the supernova remnant ($\sim 10^4$ yr) was used to estimate the SGR spin-down rate ($\dot{P} \approx 1.27 \times 10^{-12}/t_4$ where $0.6 < t_4 < 1.6$) [71]. If the spin-down is due to magnetic dipole radiation, the surface magnetic dipole field strength would be approximately $6 \times 10^{14}/\sqrt{t_4}$ G for the rotation period of ~ 8 s [71]. This object was also estimated to have a large recoil velocity if it was connected with supernova remnant N49 [71]. This was taken as evidence for an isolated neutron star as it's doubtful it would have remained in a binary system with such a large recoil velocity [71]. Additionally, there are several “kick” mechanisms which could impart a large recoil velocity to the magnetar, most of which would be ineffective for pulsars with weaker magnetic fields [71]. The slow rotation speed, large recoil velocity and bursting behavior can all be explained with the magnetar model [71].

It should be noted that many of the past associations of SGRs with supernova remnants are no longer considered significant [57]. As such, large recoil velocities are no longer considered a characteristic of magnetars.

SGRs and AXPs are thought to be magnetars, neutron stars with very strong magnetic fields that power persistent X-ray emission and intermittent bursts of hard X-rays and soft gamma-rays. Since the persistent X-ray luminosity is greater than what can be powered by the rotational energy loss that powers radio pulsars, and optical and IR observations rule out accretion from binary companion objects as the

cause, it is thought the emissions are powered by a strong magnetic field [62]. The typical estimated strength of the external field is 10^{13} – 10^{15} gauss, and it is suspected the internal field is as strong as $\sim 10^{16}$ gauss and dominated by a toroidal component.

Several pieces of evidence point to SGRs and AXPs having large external magnetic fields. The external magnetic dipole field strength is conventionally estimated from the spin-down rate (\dot{P}) and rotation period (P) with the following equation [64]:

$$B_d = 3.2 \times 10^{19} \sqrt{P\dot{P}} \text{ gauss} \quad (5.1)$$

B_d is the magnetic dipole field strength at the magnetic equator on the stars surface; the magnetic field is a factor of two stronger at the magnetic poles [64]. Large rotational spin-down rates of $\sim 10^{-13}$ – 10^{-11} s/s have been measured along with rotational periods of 2–12 s which together are consistent with magnetic dipole braking from magnetic fields of $\sim 10^{14}$ – 10^{15} gauss [62]. These field strengths are sufficient to slow the neutron star’s rotation period to ~ 10 s within 10^3 – 10^4 years, which agrees with the ages of supernova remnants in the cases where they have been associated with a magnetar. These magnetic fields are much higher than the estimated magnetic fields of normal pulsars, which are inferred from the rotation period and spin-down to be $\sim 10^{12}$ gauss [72]. The typically inferred characteristic ages ($\tau_c = P/2\dot{P}$) of pulsars are 10^7 years, which is much older than the $\sim 10^3$ – 10^4 years estimated for the spin-down from magnetic braking in magnetars [72].

The peak luminosities of SGR and AXP bursts above the Eddington limit can be explained by the strong magnetic fields [64]. The strong magnetic fields allow the photon flux to exceed the Eddington limit during bursts by causing electron scattering to become highly anisotropic and dependent on photon polarization [64].

Additionally, as mentioned in Section 5.2.3, the tails of giant flares may be due to a fireball trapped in the magnetosphere of the star. This would require a dipole magnetic field of at least $\sim 10^{14}$ gauss [57].

5.3.1. Magnetar Formation

There are several models for the formation of magnetars. When putting forth the magnetar model, Robert C. Duncan and Christopher Thompson hypothesized that a rapidly rotating neutron star coupled with vigorous convection in the early stages of the neutron star’s formation (~ 30 s) could generate the strong magnetic field with an α - Ω dynamo [71, 73]. An α dynamo is driven by the coupling of convection with rotation, and an Ω dynamo is driven by differential rotation (different depths of the star rotate with different angular velocities) [62]. An α - Ω dynamo is made up of both of these effects and only operates at low Rossby numbers (the ratio of the rotation period to the convective overturn time), which requires a small initial rotation period of $\leq \sim 1$ ms [62, 71].

In this scenario, magnetars would be created from massive stars with rapidly rotating cores [62]. The stellar cores would impart rotational energy through the magnetic field to the ejecta, producing highly energetic supernovae. So far, observations of supernova remnants associated with SGRs and AXPs have not found evidence of highly energetic supernovae. This rotational energy can be radiated away through GWs instead if the interior magnetic field is $\sim 10^{16}$ gauss.

In a formation model known as the fossil field scenario, strong magnetic fields up to 5×10^{15} gauss can result from magnetic flux conservation during the core-collapse supernova of a massive high-field star [9]. This model is “economical” as it does not require a new mechanism to produce the strong fields in magnetars, and population

synthesis calculations find this model accounts for strong-field white dwarfs, however, this model cannot account for the number of magnetars on its own, as there are too few strong-field massive stars to account for the magnetar birthrate as estimated from observations [9].

Magnetars could form during short GRBs from the coalescence of a double-degenerate binary [62]. In long GRBs, magnetars could form from core-collapse supernovae. Plateau phases are observed in a significant fraction of the Swift long GRBs, which could be powered by the initial spin-down of new magnetars.

5.3.2. Emission Mechanisms

Several mechanisms powered by the strong magnetic field have been proposed as possible sources for the persistent X-ray emission. In one, the magnetic field decays, providing internal heating which causes higher surface temperatures than similarly aged neutron stars with smaller magnetic fields [57]. In another, the motion from the magnetic field diffusing out of the neutron star core causes persistent seismic activity in the crust in the form of multiple small-scale fractures which produce Alfvén waves which contribute to the X-ray emission [57]. This mechanism could also explain the short bursts as originating from more powerful less, frequent crust fractures [57]. The persistent emissions could also be powered by magnetospheric twists in the external field induced by a stronger internal magnetic field with a large toroidal component [57]. This would cause an electric field in the magnetosphere, causing charged particles to flow, creating a current which is another source of heating for the surface [57, 62].

Multiple mechanisms have been put forth to explain magnetar bursts and giant flares; more than one of these mechanisms may be responsible, or none at all. One possible mechanism behind giant flares are large scale rearrangements of the magnetic

field caused by the internal magnetic field evolving into unstable configurations [73]. This displaces the magnetic footprints in the crust and injects energy into the magnetosphere in the form of an Alfvén pulse which causes the observed emission [73].

Bursts and giant flares could also be caused by magnetic reconnection which can occur when the magnetic field reaches unstable configurations. Possible causes for unstable configurations include the continual transfer of helicity from the internal magnetic field to the external magnetosphere or by an interchange instability in the neutron star fluid which rearranges the neutron star’s magnetic field [73].

Crust cracking is a third mechanism which could cause both bursts and giant flares. The decay of the interior magnetic field builds up stress in the crust until it breaks. The crust then moves (by rapid plastic deformation instead of fractures and voids due to the intense pressure) and twists the external magnetic field lines, injecting energy into the magnetosphere [62, 74]. Magnetic reconnections can occur depending on the configurations of the evolving magnetic field lines. Crust cracking was originally hypothesized to cause the bursts but not the giant flares, as it was thought the maximum energy this mechanism could generate was 10^{44} erg [10, 73]. Simulations by Horowitz and Kadau suggest that the breaking strain of the neutron star crust is much stronger than previously thought, partly due to the intense pressure suppressing defects [10, 74]. With this increased breaking strain, energies up to $\sim 10^{46}$ erg can be generated, enough to power the observed giant flares [10]. Furthermore, energies up to 10^{49} – 10^{50} erg may be reachable if the neutron star (or just the core) is made up of solid quark matter [10].

A fourth possibility for the cause of bursts and giant flares is hydrodynamic deformation of the star. In this model, much or all of the energy powering bursts and giant flares comes from gravitational potential energy stored in the shape of the star.

In this model, the core has a strong toroidal component which makes the star's shape more prolate [10]. Jumps between equilibrium configurations of the magnetic field release gravitational potential energy to power the bursts by reducing the toroidal component which changes the shape of the star becoming less prolate [10, 75]. This also increases the moment of inertia, increasing the rotation period [10]. First proposed by Ioka as jumps between magnetic field configurations of equal energy, this model was expanded upon by Corsi and Owen to a model which conserved the poloidal magnetic field, thus expending helicity from the magnetar [10, 75]. Corsi and Owen's model could also provide large energy jumps with a smaller internal magnetic field [10]. Hydrodynamic deformation could generate energies up to $\sim 10^{49}$ erg [10]. Corsi and Owen's model could provide this energy with a magnetic field of $\sim 10^{16}$ gauss [10].

Each of these mechanisms is powered by the internal field of the magnetar. It is thought that the internal field is ~ 10 times stronger than the external field and likely has a significant toroidal component [57]. If the 2004 giant flare is not a unique event during the active lifetime of a magnetar, it is estimated that the internal field strength is originally of order $\sim 10^{16}$ gauss [57]. The dynamo formation mechanism could form an internal magnetic field larger than $\sim 10^{16}$ gauss [10, 73]. Analytical and numerical studies have found that any stable configuration for the internal field of magnetars must have both a poloidal and toroidal component, and one model found that a strong toroidal component would form independent of its starting strength [62].

5.4. Gravitational Wave Emission from Magnetars

Magnetars are thought to be good potential sources of detectable GWs for several reasons. Magnetars are relatively close sources, with distances of known magnetars

in the range of 1.6–62.4 kpc, and many with distances close to or within 10 kpc [65]. Their strong magnetic fields provide a large energy reservoir to power electromagnetic emissions and could power detectable GWs if they are of similar energies to the bursts or giant flares. Non-radial modes, such as f-modes, torsional modes and Alfvén modes, may be excited and cause GWs in frequency ranges of interest to LIGO [59, 76, 77]. Well known sky locations and specific times from electromagnetic burst events allow a targeted search which reduces the false alarm rate and increases sensitivity in comparison to all-sky, all-time searches [59].

F-modes have been commonly considered for detections as they are thought to emit most of their energy as GWs [10, 59]. Some more speculative sources suggest low frequency modes may be better candidates for search attempts [76, 77]. This is in part due to the frequencies of the different modes. F-mode frequencies are thought to be on order of thousands of Hz [59] while torsion modes and Alfvén modes are thought to occur around hundreds of Hertz in LIGO’s most sensitive band [70, 76, 77].

Both torsional modes and Alfvén modes have low frequency modes that are hypothesized to be related to QPOs due to the overlap in frequencies [70, 76, 77, 78]. It is speculated that if either of these modes is responsible for QPOs, the modes may emit GWs for longer than the visible QPOs in the electromagnetic spectrum [78]. Some QPOs have been observed lasting 100s of seconds, which could translate to GWs with durations of hundreds to thousands of seconds [67, 78]. If GWs last only as long as QPO signals, durations could be tens to hundreds of seconds. K. Glampedakis and D. I. Jones speculate a wide range for the duration of Alfvén modes that can accommodate observed durations of QPOs, and they also suggest that Alfvén mode frequencies may evolve over time by increasing in frequency [78].

Although the exact mechanisms behind bursts are uncertain, as are the coupling to GWs, energy considerations can be used to estimate the strength of possible GWs. As previously stated in Section 5.3.2, both crust cracking and hydrodynamic deformation could provide sufficient energy to generate GWs with amplitudes comparable to the current sensitivities of the LIGO detectors [10].

CHAPTER VI

METHODOLOGY

The question motivating this search is whether detectable GWs are generated during magnetar bursts. Although there has been much research and simulations of possible GWs, there is no clear model with well predicted waveforms for GW emissions from magnetar bursts. This leads to a search for unmodeled GWs and an excess power type search. The consideration of longer duration signals paired with the uncertainty of the model and frequencies of those GWs requires a pipeline that can search for general signals of varying duration. One pipeline which meets these criteria is known as the Stochastic Transient Analysis Multi-detector Pipeline (STAMP), and was previously used in a search for long duration transients related to GRBs [79].

STAMP calculates the cross-power of two detectors and divides it by an estimated variance calculated from the auto-power of adjacent times to create a detection statistic. STAMP creates spectrograms of this cross-power statistic which is then analyzed for possible signals. In a targeted search such as this, the strength of possible signals can be compared to an estimated background distribution calculated from off-source data to estimate the significance of possible events. As an additional step to prevent a possible signal from an unknown source to be counted as part of the noise background, the background can be estimated for data that has been time shifted to non-physical times, times longer than the light crossing time of the detectors. When considering longer signals, longer time shifts are required to prevent accidental coherence from the time-shifted signal if the signal is continuous in frequency.

Three main factors differentiate this search from previous searches for GWs related to magnetars. The sixth science run of LIGO (S6) provides new data that has not

been analyzed in a previous search for GWs related to magnetar bursts. This pipeline provides a search for unmodeled waveforms of long duration. This search is also the first search to use STAMP's seedless clustering techniques.

6.1. Data Sources

There are two types of data sources for this search. One is the InterPlanetary Network (IPN), which is a network of spacecraft equipped with gamma ray detectors at different locations in the solar system, including Earth orbit and other planets such as Mercury, Venus and Mars. The network is used to search for extra-solar events emitting gamma rays, namely GRBs, but also SGR bursts. IPN provides information on what SGR and AXP bursts have been observed, and thus provides the triggers, or times of interest for this search. A list of observed SGR and AXPs bursts is available from the IPN master burst list available at <http://www.ssl.berkeley.edu/ipn3/sgrlist.txt> [80].

The second type of data for this search is from the LIGO instruments themselves: the measurements of the LIGO detectors as they search for signs of the strain from passing GWs. The main 16,384 Hz amplitude time-series data is saved at several locations, including both LIGO sites as well as a computing cluster at CalTech. There are tens of thousands of auxiliary channels monitoring data thought to be relevant to the functioning of the detector, including environmental monitors that include sensors to track wind speed, temperature, magnetometers to track the ambient magnetic fields and seismometers tracking ground motion. and channels tracking the state of different internal parts of the detectors. This data is recorded in files known as frame files and saved either on hard drives or tapes and is readily accessible on the different LIGO computing clusters.

6.2. Search Pipeline: STAMP

STAMP calculates a cross-power statistic for two detectors [81]. A spectrogram or map of frequency-time pixels (ft-map) is created in which each pixel has a value calculated from this statistic. To calculate this statistic, a filter function is applied to the cross-power. The filter function includes the sky direction, the polarization of the possible signal, the detector antenna functions and the auto-power of each detector. The filter function is applied in a separate step after the cross-power and auto-power ft-maps are created, allowing multiple directions to be tested without recalculating the initial maps.

After the filter function is applied to the ft-map, pixels are grouped into clusters and analyzed to search for possible signals. This search uses stochtrack, a type of seedless clustering algorithm based on pattern matching, looking for long and thin signals that are monotonic [82]. The advantage to this method is that no pixel or group of pixels need be above a specific threshold to form seeds for clustering. This method will also find clusters that are broken up by cuts in both frequency and time due to notches and glitch cuts. This method focuses on longer lived signals which are monotonic. For shorter duration signals, seeded clustering is likely to be superior.

6.2.1. Single Pixel Statistic

STAMP uses a cross power statistic. For a single time-frequency pixel it is [81]:

$$\hat{Y}(t; f, \hat{\Omega}) \equiv \text{Re} \left[\tilde{Q}_{IJ}(t; f, \hat{\Omega}) C_{IJ}(t; f) \right] \quad (6.1)$$

where the one-sided cross-power spectrum is [81]:

$$C_{IJ}(t; f) \equiv 2\tilde{s}_I^*(t; f)\tilde{s}_J(t; f) \quad (6.2)$$

$\tilde{Q}_{IJ}(t; f, \hat{\Omega})$ is a filter function which accounts for source direction, polarization and the detector antenna functions. For unpolarized sources, the filter function is [81]:

$$\tilde{Q}_{IJ}(t; f, \hat{\Omega}) = \frac{1}{\epsilon_{IJ}(t; \hat{\Omega})} e^{2\pi i f \hat{\Omega} \cdot \Delta \vec{x}_{IJ}/c} \quad (6.3)$$

where the ‘‘pair efficiency’’ $\epsilon_{IJ}(t; \hat{\Omega}) \in [0, 1]$ is [81]:

$$\epsilon_{IJ}(t; \hat{\Omega}) \equiv \frac{1}{2} \sum_A F_I^A(t; \hat{\Omega}) F_J^A(t; \hat{\Omega}) \quad (6.4)$$

where I and J are the detectors, $F_I^A(t; \hat{\Omega})$ is the ‘‘antenna factor’’ for detector I and $\Delta \vec{x}_{IJ} \equiv \vec{x}_I - \vec{x}_J$ is the difference in position vectors of the detectors. A is summed over the GW polarizations.

An estimator for the variance of \hat{Y} is [81]:

$$\hat{\sigma}_Y^2(t; f, \hat{\Omega}) = \frac{1}{2} |\tilde{Q}_{IJ}(t; f, \hat{\Omega})|^2 P_I^{\text{adj}}(t; f) P_J^{\text{adj}}(t; f) \quad (6.5)$$

where $P_I^{\text{adj}}(t; f)$ is the average one-sided auto-power spectrum in neighboring pixels [81]:

$$P_I^{\text{adj}}(t; f) \equiv 2 \langle |\tilde{s}_I(t; f)|^2 \rangle \quad (6.6)$$

The brackets $\langle \rangle$ denote an average over neighboring pixels.

The SNR from STAMP for a single pixel is then defined as [81]:

$$\text{SNR}(t; f, \hat{\Omega}) \equiv \frac{\hat{Y}(t; f, \hat{\Omega})}{\hat{\sigma}_Y(t; f, \hat{\Omega})} = \text{Re} \left[\frac{\tilde{Q}_{IJ}(t; f, \hat{\Omega})}{|\tilde{Q}_{IJ}(t; f, \hat{\Omega})|} \frac{C_{IJ}(t; f)}{\sqrt{\frac{1}{2}P_I^{\text{adj}}(t; f)P_J^{\text{adj}}(t; f)}} \right] \quad (6.7)$$

Note that this SNR of a single ft-pixel does not depend on the polarization properties of the source, as the polarization does not affect the phase of \tilde{Q} , which is the only dependence of this SNR since it doesn't depend on the magnitude of \tilde{Q} [81]. This degeneracy can be broken when combining ft-pixels from multiple times or multiple detector pairs [81].

6.2.2. Multi Pixel Statistic

For a multi-pixel statistic where a transient persists over N pixels in a set of pixels Γ , the SNR of the cluster is calculated by summing the SNR of the individual pixels and dividing by \sqrt{N} :

$$\text{SNR}_{\Gamma}(\hat{\Omega}) = \frac{\sum_{t; f \in \Gamma} \text{SNR}(t; f, \hat{\Omega})}{\sqrt{N}} \quad (6.8)$$

In the case of the clustering algorithm described in Section 6.2.3, when the line defining the cluster overlaps two pixels for the same time (t), the pixels will be weighted and treated as one pixel.

6.2.3. Seedless Clustering

There are two general types of clustering algorithms used by STAMP: seed-based clustering and seedless clustering. Burstegard is an example of the more conventional seed-based clustering approach which is based on using pixels above a given threshold

as seeds to group into larger clusters. Burstegard was used in the search for long transients related to GRBs, and a related algorithm called zebra-gard was used in the STAMP all-sky search [79, 83].

The algorithm called stoch-track is a seedless clustering algorithm that instead relies on creating many curves from quadratic Bezier functions and using those as the potential clusters, compares the SNR of each cluster, keeping the loudest [82]. This gives a loudest cluster statistic for each ft-map it is used on. Constraints to the randomly generated curves include requiring the curves persist for a minimum time t_{min} , as well as fitting to three time-frequency control points: $P_0(t_{start}, f_{start})$, $P_1(t_{mid}, f_{mid})$ and $P_2(t_{end}, f_{end})$. These control points are used to form a curve parameterized by $\xi = [0, 1]$ [82]:

$$\begin{pmatrix} t(\xi) \\ f(\xi) \end{pmatrix} = (1 - \xi)^2 P_0 + 2(1 - \xi)\xi P_1 + \xi^2 P_2 \quad (6.9)$$

Each template is generated using six random numbers. This can be done with GPUs. The number of templates is often $\mathcal{O}(10^5 - 10^8)$, with order 200,000 (or 2×10^5) as typical. This search used 30,000,000 (3×10^7) templates.

6.3. Data Analysis Procedures

The data in this search was analyzed using STAMP with the seedless clustering method as described in Section 6.2.3. First, the triggers that occurred during coincident science times were identified which allowed the on-source and off-source data to be determined for each trigger. Once the source direction was determined and the appropriate spectral lines notched, the background was estimated using the off-source data and the significance of the on-source events could be determined. The off-source data was compared to simulations as well as additional off-source data sets that had

their own constraints. Those constraints were: 1) the power configuration must be the same as the off-source; or 2) the range must be within 5% of the off-source.

6.3.1. Identifying Triggers

The potential triggers for this search were taken from the IPN master burst list [80]. The time given for each trigger is the Universal Time at the satellite when the satellite was triggered, not the time at which the signal crossed the Earth. From the IPN burst list it can be seen that all triggers that occurred during S6 are recorded for times at satellites within one light second of the Earth. The time of each trigger is also truncated to one second accuracy. These two sources of timing error add up to as much as one second, which is within the limits of the on-source window of [-2, 1602] seconds as described in Section 6.3.4.

Triggers from this list were chosen for this search if they occurred when both H1 and L1 were active and in science mode. The FERMI/GBM list was also searched for possible triggers, however no new triggers were found during coincident science times [84]. There were three triggers which satisfied these conditions (see Table 6.1). The chance that a trigger occurred just before the start of coincident science time was also considered. Triggers within 1000 seconds of coincident science times were searched and one trigger was found, however it was disregarded because it was quite far from coincident science time.

Trigger	GPS	UTC (at satellite)	Source	Epoch
2469	940556320	26 OCT 2009 01:38:25	SGR 1806-20	S6B
2471	949827104	26 MAR 2010 20:48:59	SGR 1806-20	S6C
2475	957191879	06 MAY 2010 14:37:44	1E 1841-045	S6C

TABLE 6.1. Information on S6 magnetar burst triggers.

Virgo was also considered as a possible data source, however adding Virgo data provided no new triggers. Virgo was active during the trigger at 940556320 GPS, but the ranges of H1 and L1 were superior. Virgo was not active during S6 C, and thus not active during the other two triggers. The STAMP pipeline is designed to handle two detectors, therefore because Virgo data was either unavailable or available with less sensitivity, H1 and L1 alone were used for this study. The commands used to find the times each detector was in science mode are listed in Table 6.2.

LHO	<pre>ligolw_segment_query --database --query-segments --include-segments 'H1:DMT-SCIENCE:4' --gps-start-time 931035296 --gps-end-time 971622272 ligolw_print -t segment:table -c start_time -c end_time -d " " > H1S6science4.txt</pre>
LLO	<pre>ligolw_segment_query --database --query-segments --include-segments 'L1:DMT-SCIENCE:4' --gps-start-time 931035296 --gps-end-time 971622272 ligolw_print -t segment:table -c start_time -c end_time -d " " > L1S6science4.txt</pre>
Virgo (VSR2)	<pre>ligolw_segment_query --database --query-segments --include-segments 'V1:ITF_SCIENCEMODE:6' --gps-start-time 931035296 --gps-end-time 971622272 ligolw_print -t segment:table -c start_time -c end_time -d " " > V1VSR2science6.txt</pre>
Virgo (VSR3)	<pre>ligolw_segment_query --database --query-segments --include-segments 'V1:ITF_SCIENCEMODE:7' --gps-start-time 931035296 --gps-end-time 971622272 ligolw_print -t segment:table -c start_time -c end_time -d " " > V1VSR3science7.txt</pre>

TABLE 6.2. Commands to find science segment times during S6 and save in text files.

6.3.2. Source Direction

The directions used in the search for GWs for each magnetar burst event were those of the source object. Two sources were identified from the online master burst list: SGR 1806-20 (an SGR) and 1E 1841-045 (an AXP) [80]. The directions of these

objects were provided from the McGill magnetar catalog, available online¹ and in the cited publication [85]. See Table 6.3 for source sky location and distance.

Source	Right Ascension (hrs)	Declination (degrees)	Estimated Distance
SGR 1806-20	18h08m39.337s	-20°24'39.85"	8.7+1.8-1.5 kpc
1E 1841-045	18h41m19.343s	-04°56'11.16"	8.5+1.3-1.0 kpc

TABLE 6.3. Information on S6 magnetar burst source positions and distances from Earth [85].

Since astronomical objects are continually moving through space, their sky positions change over time. If the change in position of the objects is large enough, proper motion must be accounted for to accurately target the source object with the time delay of the detectors. SGR 1806-20 was localized and its counterpart identified in [86] and its proper motion estimated in [87]. 1E 1841-045 was localized in the sky and multiple possible counterparts identified in [88]. A more recent study has proposed a possible near infrared (NIR) counterpart, however the counterpart could not be confirmed [89]. Therefore, studies on the proper motion of 1E 1841-045 are restricted to placing upper limits. The upper limits on both the RA and declination of 1E 1841-045 are currently less than four milliarcseconds per year (mas/yr) [90]. Table 6.4 summarizes the proper motion of both sources.

Source	Proper Motion RA (mas/yr)	Proper Motion Dec (mas/yr)
SGR 1806-20	-4.5	-6.9
1E 1841-045	< 4	< 4

TABLE 6.4. Information on S6 magnetars burst sources proper motions [85, 87, 90].

The resolution of the LIGO-Virgo three detector network is estimated to be ~ 10 square degrees for 90% confidence limits [91]. The possible change in sky position

¹The McGill Online Magnetar Catalog is available at <http://www.physics.mcgill.ca/~pulsar/magnetar/main.html> [65]

for either source over 10 years is much smaller than this resolution (SGR 1806-20: $\Delta\text{RA} = 0\text{hr}0\text{m}0.045\text{s}$ $\Delta\text{dec} = 0^\circ0\text{m}0.069\text{s}$, 1E 1841-045: $\Delta\text{RA} < 0\text{hr}0\text{m}0.040\text{s}$ $\Delta\text{dec} < 0^\circ0\text{m}0.040\text{s}$). The actual difference from measurement time to trigger time is on order of 3–5 years, and the corresponding change in sky position proportionally smaller. Compared to the estimated sky resolution of $\sim 3^\circ$ (0.2 hrs or 0hrs12m), the changes in sky position are negligible for this analysis. Therefore, the sky positions are taken as directly measured.

6.3.3. Data Quality

The cross-power analysis method used by this search requires data from science segments with coincident data from two detectors. A science segment is “defined as time when the interferometer is operating in a nominal state and the spectral sensitivity is deemed acceptable by the operator and scientists on duty” [19]. Data from times marked by CAT1 flags are deemed as having severe data quality issues and are not used in this search. There are also various times with hardware injections, where a fake signal is put into the data. These times are also removed from the analysis as the data is contaminated by the injection. Times with pulsar injections were not removed as they were continuously running, but the pulsar lines were notched if they showed up in the background as described in Section 6.3.6. The times that are left were listed in the job file for the STAMP-AS search. This job file was used as the basis of available times for this search.

6.3.4. Search Window

The search window is defined by two sets of limits: the time window and the frequency window. The time window for this search spans two seconds before the

trigger to 1600 seconds after the trigger, or $[-2, 1600]$ s. The 1600 seconds following the trigger is based on two things: 1) observations that the longest afterglow from a giant flare was about 400 seconds long; and 2) the idea from several papers that GW signals associated with QPOs may last several times longer than the observed QPOs in the EM afterglow of the giant flares. The two seconds preceding the trigger is to ensure the start of the event is in the data and to account for any possible timing errors from the satellites, as well as the difference in time at the satellites and that recorded on Earth.

The pixels in the ft-maps are 4 seconds by 1 Hz due to the combination of computational limits, increased sensitivity with longer pixels, and ability to search for more general waveforms with shorter pixels. The ft-map is calculated with a Hann window and 50% overlap of each pixel in time, making the time resolution two seconds. The resulting 4 s by 0.25 Hz pixels are combined into 4 s by 1 Hz pixels. The 50% overlap adds an additional two seconds on to the end of the time window, making the effective time window $[-2, 1602]$ s.

The end of LHO’s science segment (at 940557107 GPS) is 787 s after the trigger (at 940556320 GPS) [80]. The resolution of the pixel map is 2 s, so the end of this trigger’s on-source window becomes 786 s. After accounting for the 18 s needed for preprocessing at the end of the segment, the on-source window of this event becomes $[-2, 766]$ s ($[-2, 768]$ s with the 50% overlap).

The frequency range of the ft-maps spans 40 Hz to 2500 Hz, or $[40, 2500]$ Hz. The lower bound comes from the seismic wall at lower frequency, and the higher bound is set to include the highest observed QPO frequencies in the EM afterglow, including the QPOs at 1840 Hz and 2384 Hz. The search window parameters are summarized in Table 6.5.

Frequency window	[40, 2500] Hz
Time window (with 50% overlap)	[-2, 1600] ([-2, 1602]) s
Time window for trigger 2469 (with 50% overlap)	[-2, 766] ([-2, 768]) s
Δf	1 Hz
Δt	4 s (2 s time resolution)
FFT window	Hann

TABLE 6.5. Search window parameters.

6.3.5. On-Source Window

The on-source window consists of the data surrounding a trigger. It includes the time required for the search window plus additional data for the preprocessing stage. The on-source window is not time shifted. The on-source window includes 18 seconds before and after the search window. This gives an on-source window of [-20, 1620] s ([-20, 786] for trigger 2469). The 18 seconds includes a 2 second buffer as well as 16 seconds to help estimate the pixel background for the pixels on the beginning and end of the pixel map. The windows are summarized in Table 6.6.

On-source window	[-20, 1620] s
On-source window for trigger 2469	[-20, 786] s

TABLE 6.6. On-source windows.

6.3.6. Notching Lines

The lines notched for each trigger were chosen by running the analysis on data without notches. Initially the window was broken up in frequency into smaller overlapping sub-windows: [40, 70] Hz, [40, 500] Hz, [70, 500] Hz, [250, 750] Hz, [500, 1000] Hz, [750, 1250] Hz, [1000, 1500] Hz, [1250, 1750] Hz, [1500, 2000] Hz, [1750, 2250] Hz and [2000, 2500] Hz. First, tens of sets of time shifted segment-pairs with

1 s \times 1 Hz pixels were run using these sub-windows without setting the clustering seed. These segment-pairs were run with time windows of [-2, 400] s (with an additional half second on the end due to the 50% overlap). Then, tens of sets were run with 4 s \times 1 Hz pixels and the normal time window. The number of templates run in the sub-windows was first 3,000,000 and then 6,000,000. As identifiable lines were found, these segment-pairs were rerun with the identified lines notched to search for additional lines. Next the full 1000 off-source set of segment-pairs was run using the full window, and any qualifying lines found were notched. When running with the full window, 30,000,000 templates were used. Finally, the full set of 1000 off-source segment-pairs was run with the clustering seed used for the analysis and any identified lines were notched.

Lines that appeared with an identified source on the notch list <https://wiki.ligo.org/viewauth/Main/Notchlist> were notched, as well as adjacent lines that appeared on the STAMP-AS list [92]. Lines that showed up this second way were lines adjacent to 60 Hz harmonics which had also showed up and been notched. There were a few additional lines adjacent to identified lines in the off-source data that didn't appear in the STAMP-AS list. These consisted of a line near a 16 Hz harmonic, lines adjacent to 60 Hz harmonics and lines adjacent to pulsar injections. These lines were also notched as they were adjacent to identified lines.

Many other lines showed up; however, they were within the background distribution and didn't show up in either the notch list or the STAMP-AS list. Because they were within the background distribution and not creating a tail and the source was not identified, they were not notched. Notching identified lines and adjacent lines was sufficient to remove the population of high-SNR clusters that deviated largely from the distributions from simulations (see Section 6.3.9).

The lines for each trigger are detailed in Table 6.7, Table 6.8 and Table 6.9.

SGR Trigger 2469	
Line Source	Line(s) [Hz]
60 Hz and surrounding frequencies	57, 58, 59, 60, 61, 62, 63
Second 60 Hz harmonic and surrounding frequencies	119, 120, 121
Third 60 Hz harmonic and surrounding frequencies	178, 179, 180, 181, 182
Fourth 60 Hz harmonic and surrounding frequencies	239, 240, 241
Seventh 60 Hz harmonic and adjacent frequency	420, 421
Ninth 60 Hz harmonic and adjacent frequency	540, 541
Additional 60 Hz harmonics	300, 360, 480, 600, 720, 960, 1080, 1380, 1740, 1800
Pulsar injection and adjacent frequency	53, 54
Pulsar injection nearby	108
16 Hz harmonic and adjacent frequency	223, 224
16 Hz harmonics	64, 320, 368
2 Hz harmonic	372
16 Hz harmonic, Hanford photon calibration line, high coherence notch	400
High coherence notch	1478

TABLE 6.7. Lines identified and notched for trigger 2469. Line sources identified from [92].

6.3.7. Background Estimation

The background for each trigger is estimated with 1000 time-shifted data segment-pairs taken from off-source data (data outside of the on-source window). Each of these sections of data is the same size as the on-source window of the associated trigger. The data sections are made from the off-source data of the STAMP-AS jobs mentioned in Section 6.3.3. The data sections are created such that they occur in both detectors at the same time and do not overlap other sections. The sections are taken from

Trigger 2471	
Line Source	Line(s) [Hz]
60 Hz and surrounding frequencies	57, 58, 59, 60, 61, 62, 63
Second 60 Hz harmonic and surrounding frequencies	118, 119, 120, 121, 122
Third 60 Hz harmonic and surrounding frequencies	179, 180, 181, 182
Fourth 60 Hz harmonic and surrounding frequencies	239, 240, 241
Fifth 60 Hz harmonic and surrounding frequencies	299, 300, 301
Eighth 60 Hz harmonic and adjacent frequency	480, 481
Additional 60 Hz harmonics	360, 420, 720, 960, 1380, 1800
Pulsar injection nearby	108
16 Hz harmonic and high coherence notch	112
16 Hz harmonics	224, 304, 384
2 Hz harmonic	372
16 Hz harmonic, Hanford photon calibration line, high coherence notch	400

TABLE 6.8. Lines identified and notched for trigger 2471. Line sources identified from [92].

data as close to the on-source window as possible. For example, if 2000 seconds of coincident data is available, the closest 1640 seconds are taken to create an off-source data segment. If less continuous data is available than the length of the on-source window, then that data is not included in the analysis. In the case of trigger 2469, after the 1640 second long off-source data segments are formed, the first 806 seconds are used in order to match up with the shortened on-source window.

The 1000 time-shifted data segment-pairs are generated from 33 segments from each detector (66 total). Taking data from completely different times ensures the data is shifted by at least the duration of the on-source window. A monochromatic or near-monochromatic signal could add into the background estimation if the time-shift isn't longer than the signal time. The large time shift from pairing different

SGR Trigger 2475	
Line Source	Line(s) [Hz]
60 Hz and surrounding frequencies	57, 58, 59, 60, 61, 62, 63
Second 60 Hz harmonic and surrounding frequencies	119, 120, 121
Third 60 Hz harmonic and surrounding frequencies	178, 179, 180, 181, 182
Fourth 60 Hz harmonic and surrounding frequencies	239, 240, 241
Additional 60 Hz harmonics	300, 360, 480, 1380, 1560, 1740
Pulsar injection and adjacent frequency	52, 53
Pulsar injection nearby	108
16 Hz harmonic	64
2 Hz harmonic	372
16 Hz harmonic, Hanford photon calibration line, high coherence notch	400
Livingston photon calibration	404
High SNR notch	85

TABLE 6.9. Lines identified and notched for trigger 2475. Line sources identified from [92].

segments together helps prevent this possibility. Shifting by time segments also allows many time-shifted data sets to be generated from a small amount of data close to the on-source time, which is preferable for estimating the noise of the on-source. By pairing different segments from each detector together, 1056 time-shifted segment-pairs can be formed. The thousand segment pairs are chosen such that the sum of the difference between the on-source start time and the off-source pairs segment start times is minimized.

1000 time-shifted segment-pairs was chosen for two reasons. The first was to get a smooth SNR distribution for the background estimation. The second was reduce the probability that the on-source SNR was louder than the background due to noise fluctuations. The probability of any one of the three triggers having a larger SNR

than their loudest respective background SNRs due to random chance is 0.2997001%, making the significance of such an event nearly 3 sigma. This is calculated in 6.10, where $P_{\text{SNR} \geq \text{SNR}_{\text{Threshold}}}$ is the probability for a single trigger that the on-source event is louder than the background due to noise, n is the number of triggers ($n = 3$ in this search), P_{none} is the probability that none of the SNRs of the triggers is above their backgrounds and P_{any} is the probability that any of the on-source SNRs is above their backgrounds :

$$P_{\text{any}} = 1 - P_{\text{none}} = 1 - (1 - P_{\text{SNR} \geq \text{SNR}_{\text{Threshold}}})^n = 1 - (1 - 1/1000)^3 = 0.002997001 \quad (6.10)$$

After the SNR of the loudest cluster of each off-source time-shifted data segment-pair was found, it was then ordered with the rest of the off-source SNRs into an SNR distribution that was used to estimate the false alarm probability (FAP). The probabilities were assigned to the population by the proportion P_{α} of clusters with SNR greater than or equal to the cluster α 's SNR (where $N_{\text{SNR} \geq \text{SNR}_{\alpha}}$ is the number of clusters with SNR greater than or equal to the cluster α 's SNR and N_{Total} is the total number of clusters):

$$P_{\alpha} = N_{\text{SNR} \geq \text{SNR}_{\alpha}} / N_{\text{Total}} \quad (6.11)$$

The cluster with the lowest SNR was assigned a probability of 1, while the cluster with the highest SNR was assigned a probability of 1/1000 or 0.001. This method was used to calculate the SNR distributions in both the time-shifted and simulated sets of data. The FAP of the on-source event was estimated as the proportion of off-source clusters with SNR equal to or greater than that of the on-source event:

$$\text{FAP} = N_{\text{SNR} \geq \text{SNR}_{\alpha}} / N_{\text{Total}} \quad (6.12)$$

If the event turned out to be louder than the loudest of the off-source clusters, then more off-source time-shifts would be needed to properly estimate the SNR of the event.

6.3.8. Horizon Distance and Laser Power

In the process of estimating the background of each trigger, two questions about data quality and how well the off-source data represents the on-source data were raised. The first question was how does the laser power of the detectors affect the background SNR distribution? The second question was does the background SNR distribution change with the current range of the detector? Two additional background estimations were calculated for each trigger to test these questions (with the exception of trigger 2469 where the entire set of off-source segments were in the same power configuration as the on-source window). In order to test whether the laser power affected the SNR distributions, the 33 closest segments with the same power configuration as the on-source were used. In order to test the effect of the range on the SNR distribution, the 33 closest segments in which the horizon distance was within 5% of the on-source average were chosen.

The state of the laser power was determined by querying the segment database to find the times when the different power flags were active. The power flags were H1:DMT-PSL_POWER_LT_10W, H1:DMT-PSL_POWER_LT_14W, L1:DMT-PSL_POWER_LT_10W and L1:DMT-PSL_POWER_LT_14W. The flags were active when the wattage of the power was at or below the number before the W in the flag (e.g. laser power in H1 was at or below 10 Watts when H1:DMT-PSL_POWER_LT_10W was active). To verify the accuracy of these flags, the LIGO electronic logs were consulted, and when the laser power was recorded, they

agreed with the flags. Additionally, the laser power channels H1:PSL-PWR_PWRSET and L1:PSL-PWR_PWRSET were checked for the background and on-source of trigger 2471 and matched up with the flags.

The power flags were used to find time segments with the same power configuration in H1 and L1 as the on-source. First the time segments were broken up in the same fashion as the earlier off-source segments, requiring the times to be within the STAMP-AS jobs. Then the segments were picked individually for each detector such that the laser power configuration matched that of the on-source for that detector. It was not a requirement to choose segments that matched for both detectors, but rather the closest segment was chosen for a specific detector if it matched the laser power.

Data from <https://dcc.ligo.org/LIGO-T1100338/public> was used to find the 33 closest jobs within 5% of the on-source horizon distance [93]. The horizon distance for a binary system in which each object was one solar mass was chosen for this comparison. The horizon distances were calculated for 2048 second long segments (that will be termed “range segments”) that are not always in sync with the segments calculated in this search [93]. If a segment of this search was completely within one of the range segments, then the horizon distance of that range segment was used; otherwise, if the segment overlapped multiple range segments, then the horizon distance was estimated using the average of the horizon distance as calculated by the number of seconds the segment overlaps each range segment. The segments were chosen for restricted range in a similar way as for the restricted power configuration: after initially breaking the coincident data into segments requiring the times to be within the STAMP-AS jobs, the segments closest to the on-source were chosen independently for each detector if they were within 5% of the on-source range for that detector.

For all of the triggers, the effect of restricting either the laser power or the horizon distance did not significantly affect the SNR distributions.

6.3.9. Monte-Carlo Simulations

The background SNR distribution from time-shifted data of each trigger's off-source segments was compared to SNR distributions calculated from Monte-Carlo simulations. 1000 time-shifted simulated segment-pairs were used to generate a single simulated SNR distribution. Ten simulated SNR distributions were generated for each trigger. For each SNR distribution, 33 sets of simulated segments per detector were generated (66 total). All simulated segments, regardless of detector or trigger, used a unique number to seed the random number generator. These 33 segments per detector were used to construct 1000 segment-pairs for each simulated SNR distribution in the same fashion as the time-shifted segment-pairs. Each segment was assigned a detector and time corresponding to one of the off-source segments. The simulated segments were used to construct 1000 segment-pairs using the 1000 closest segment-pairs to the on-source time, just like with the time-shifted data. The Gaussian data from each simulation was colored by the on-source PSD for the appropriate detector. The PSD was estimated using data from the on-source window with Welch's method as implemented by the python library matplotlib (function matplotlib.pyplot.psd) using 50% overlap and 1 second long intervals.

6.3.10. Software Specifics

The version of the STAMP pipeline used in this analysis is stamp2 Rev # 11102 from <https://ligo-vcs.phys.uwm.edu/svn/matapps/packages/stochastic/trunk/stamp2>. Two separate matlab files were used for preprocessing.

The first was “anteproc.m”, which was used for all the data that did not require injections, including the simulated data. The second was “preproc.m”, which was used when injections were used, as well as during initial testing. They are mostly the same, with the main differences being “preproc.m” can inject waveforms and processes data from both detectors and saves them in one “.mat” file. “anteproc.m” has the advantage that it will save the data processed from each detector separately, which lowers the amount of preprocessing and data storage that is needed (66 segments preprocessed vs 1000 with “preproc.m”). When using “anteproc.m” the data can be time-shifted after preprocessing, while “preproc.m” would need to rerun the data each time a different time-shift was needed. Both “preproc.m” and “anteproc.m” read in a parameter file with the settings for the preprocessing stage, a job file defining each of the possible time segments, and a number that determines which time segment will be preprocessed.

The main stage of the analysis used “grand_stochtrack.m”, which is a wrapper for “clustermmap.m”. “clustermmap.m” calculates the cross-power map, the sigma map and the SNR map from the power maps from the preprocessing stage, as well as performs the clustering. “grand_stochtrack.m” is designed for use with configuration files and takes, as input, the configuration file and a number (in this case the segment-pair number out of 1000).

“preproc.m”, “anteproc.m” and “grand_stochtrack.m” were all compiled into Matlab executables to be used on the CalTech cluster using Condor, software that manages the distributed parallelization of tasks on the LIGO clusters. The Matlab version used was Matlab 2013a.

CHAPTER VII

RESULTS OF GRAVITATIONAL WAVE SEARCH

No gravitational wave candidate was identified in this search. The loudest and most significant cluster was from SGR trigger 2475, with $\text{SNR} = 6.24$ and $\text{FAP} = 0.213$. When rerun with the absolute value SNR modification to the clustering algorithm discussed in Section 7.3, the SNR was the same with $\text{FAP} = 0.378$. The lowest upper limit calculated from this search was from this same trigger. The energy upper limit for a 90% confidence level (CL) was calculated as $E_{\text{GW}} = 1.48 \times 10^{46}$ erg for a half sine-Gaussian waveform with central frequency $f_0 = 150$ Hz and characteristic time $\tau = 400$ s for a source at a distance of 8.5 kpc. Accounting for the calibration error, this upper limit becomes $E_{\text{GW}} = 2.03 \times 10^{46}$ erg. The search results for all three triggers are summarized in Table 7.1. See Table 7.6 and Table 7.7 for the full set of calculated upper limits.

7.1. Search Results

SGR 2475 had the most significant cluster with an SNR of 6.24 and an FAP of 0.214 ($\text{FAP} = 0.378$ when rerun with the absolute value SNR modification). The probability of one of the three triggers having $\text{FAP} \leq 0.213$ is slightly more than 51%. The results for all three triggers is summarized in Table 7.1. See Figure 7.1, Figure 7.2 and Figure 7.3 for plots of each of the three open boxes plotted against their respective background and simulated backgrounds. See Figure 7.6 and Figure 7.7 for the FT-map and loudest cluster for SGR trigger 2475.

As it was found that SGR trigger 2469 and SGR trigger 2475 had a negative SNR response to linear polarizations, the background and on-source was rerun for

Trigger	SNR	FAP	abs SNR	abs FAP
2469	5.73	0.929	6.06	0.679
2471	5.79	0.888	N/A	N/A
2475	6.24	0.214	6.24	0.378

TABLE 7.1. Summary of open-box results. SGR trigger 2471 had a positive SNR response to all tested polarizations, so rerunning with the absolute value SNR modification was unnecessary. The other two were rerun, so the SNRs and FAPs can be interpreted for circular and linear polarizations respectively (although the SNR for SGR trigger 2475 did not change, so the positive SNR was louder). The SNR values are rounded to 3 significant figures. The FAP values are exact as calculated from individual backgrounds.

these triggers with the absolute value SNR modification to the clustering algorithm. The new background distributions are plotted and compared to the old background distributions in Figure 7.4 and Figure 7.5 respectively. The simulated backgrounds were not rerun in the interest of saving computational resources and time. SGR trigger 2471 was not rerun because all tested polarizations returned a positive SNR.

The rerun background distributions become somewhat louder. SGR trigger 2469 had a louder cluster when rerun with the absolute value modification. Both the backgrounds and on-source are in line with expectations: if random noise does not favor positive or negative SNRs, each job-pair would have a 50% probability of it's loudest cluster having positive SNR. This means it is likely around half the job-pairs would have a loudest cluster with negative SNR which wouldn't have been counted without the absolute value modification. The magnitudes of these negative SNR clusters should have the same behavior as the positive SNR clusters, so they shouldn't drastically effect the background distribution. The results using the absolute value clustering algorithm are summarized in Table 7.1.

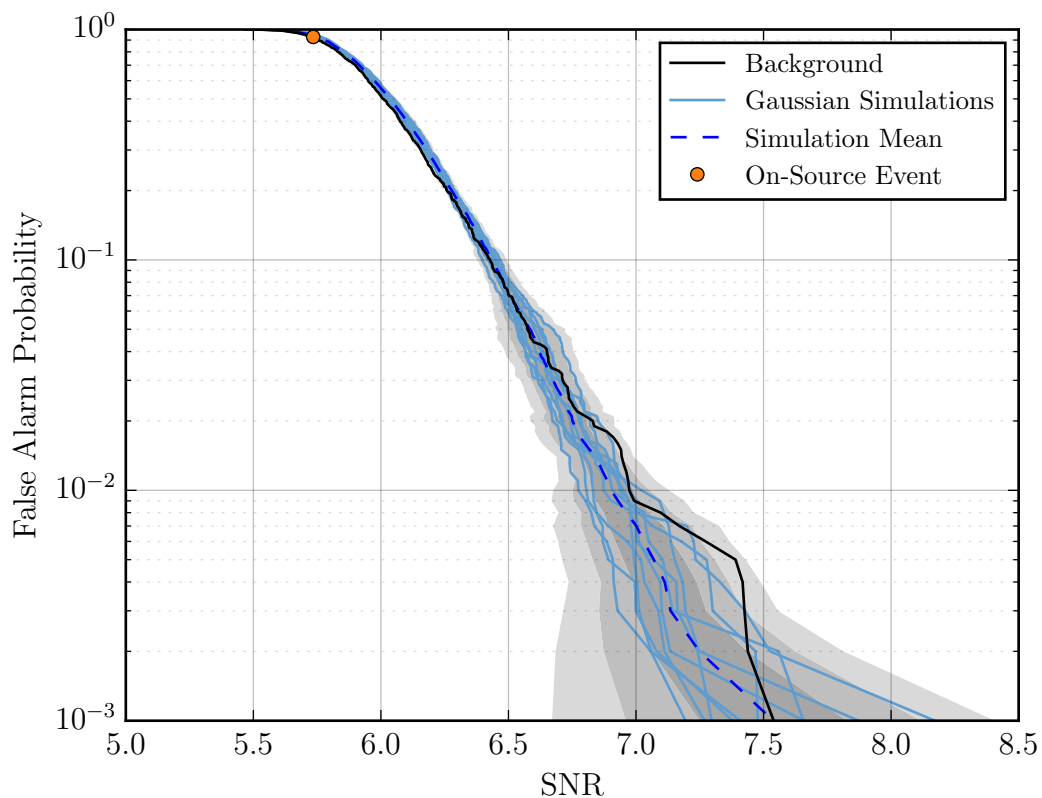


FIGURE 7.1. The on-source event plotted against the background for SGR trigger 2469. The shaded grey areas mark the regions within $\sigma = 1, 2, 3$ thresholds along the x-axis. σ was calculated for each FAP using the SNRs from 10 simulated SNR distributions as described in Section 6.3.9. For the on-source event, SNR = 5.73 and FAP = 0.929.

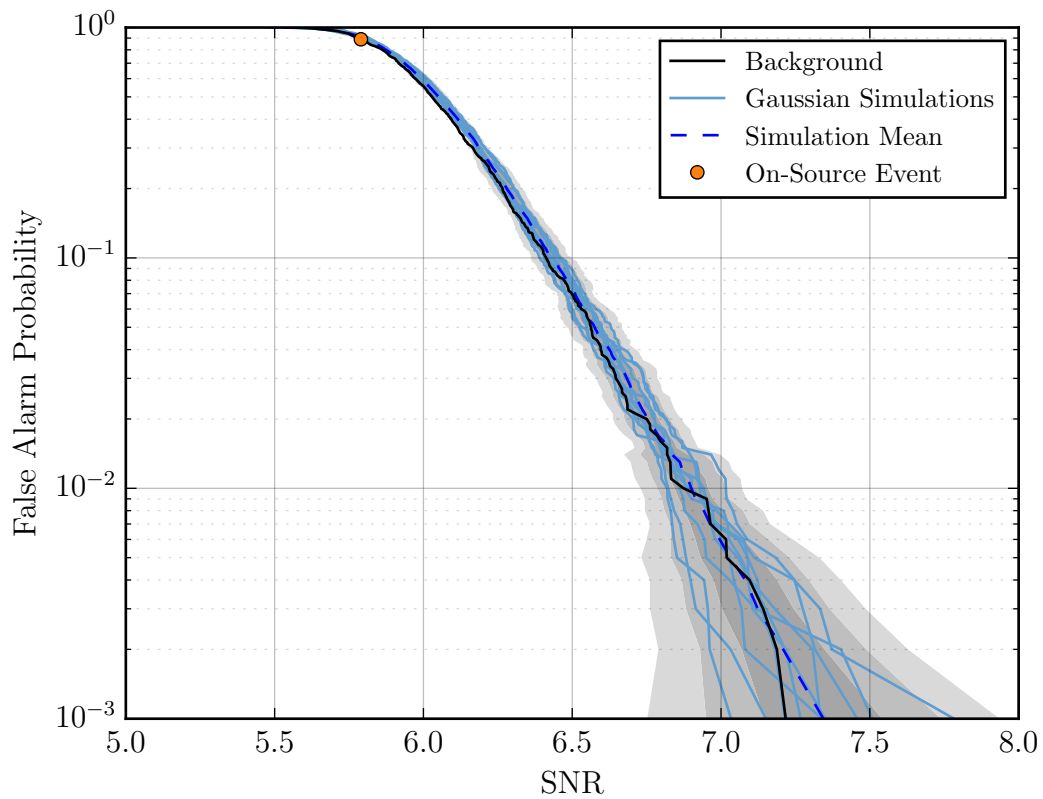


FIGURE 7.2. The on-source event plotted against the background for SGR trigger 2471. The shaded grey areas mark the regions within $\sigma = 1, 2, 3$ thresholds along the x-axis. σ was calculated for each FAP using the SNRs from 10 simulated SNR distributions as described in Section 6.3.9. For the on-source event, $\text{SNR} = 5.79$ and $\text{FAP} = 0.888$.

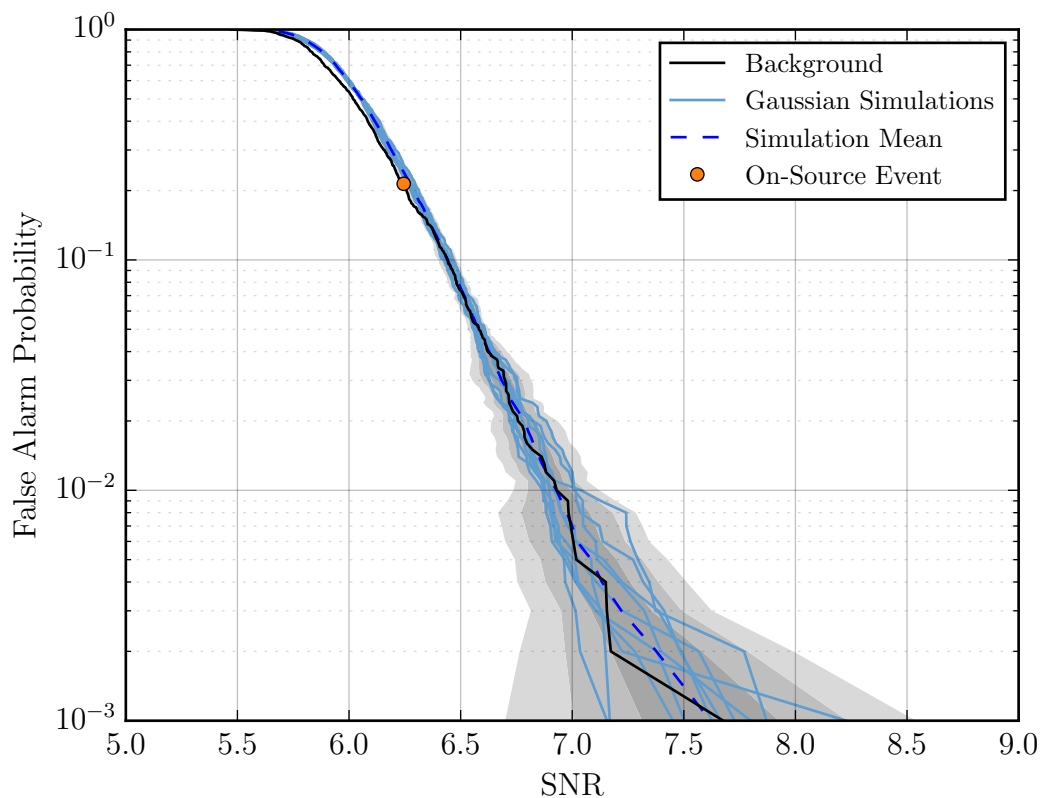


FIGURE 7.3. The on-source event plotted against the background for SGR trigger 2475. The shaded grey areas mark the regions within $\sigma = 1, 2, 3$ thresholds along the x-axis. σ was calculated for each FAP using the SNRs from 10 simulated SNR distributions as described in Section 6.3.9. For the on-source event, $\text{SNR} = 6.24$ and $\text{FAP} = 0.214$.

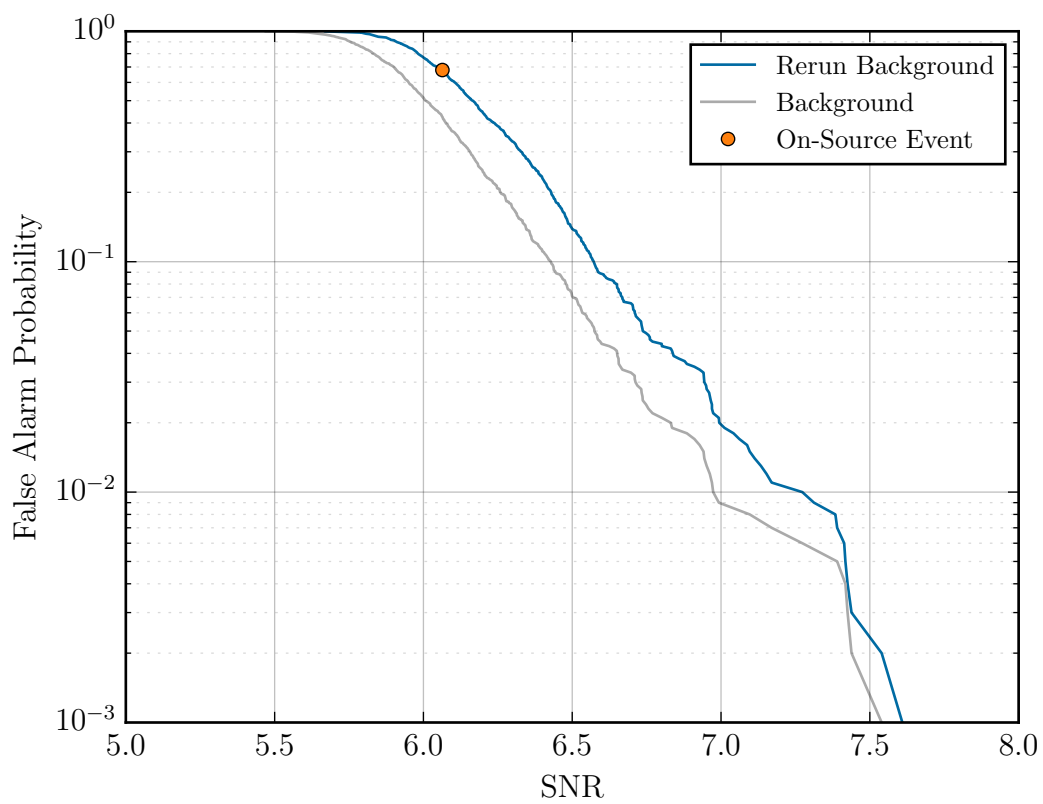


FIGURE 7.4. FAP vs SNR for 2469 for abs SNR version. For the on-source event, SNR = 6.06 and FAP = 0.679.

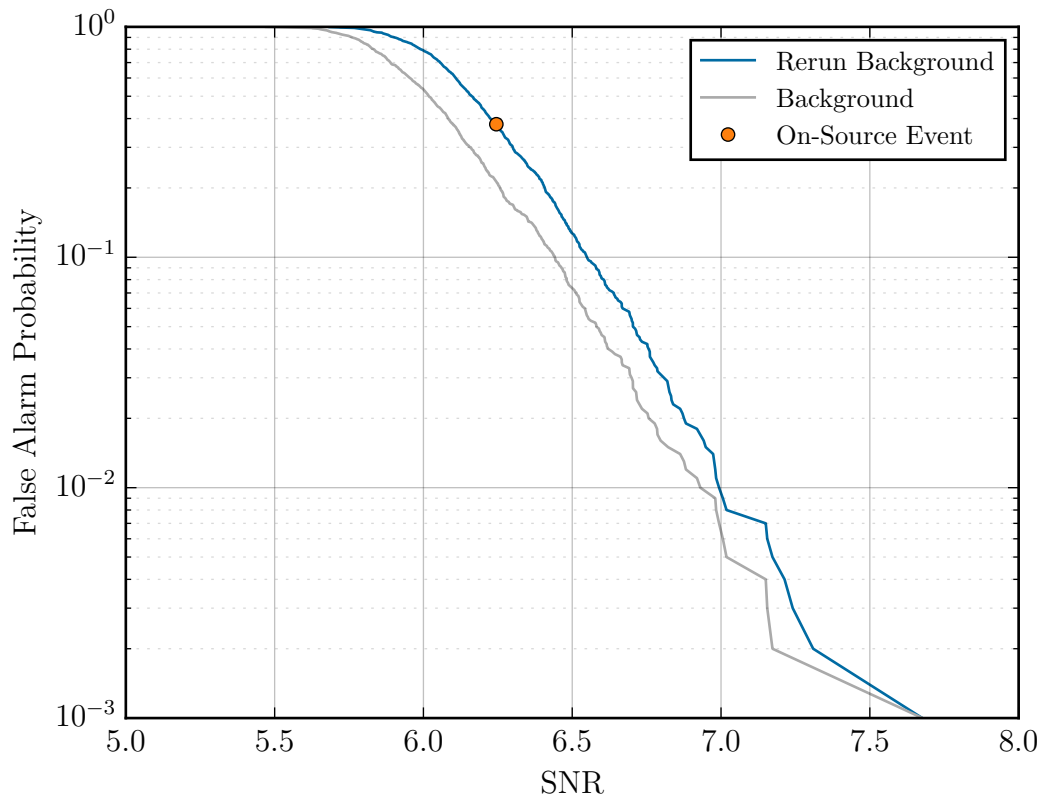


FIGURE 7.5. FAP vs SNR for 2475 for abs SNR version. For the on-source event, SNR = 6.24 and FAP = 0.378.

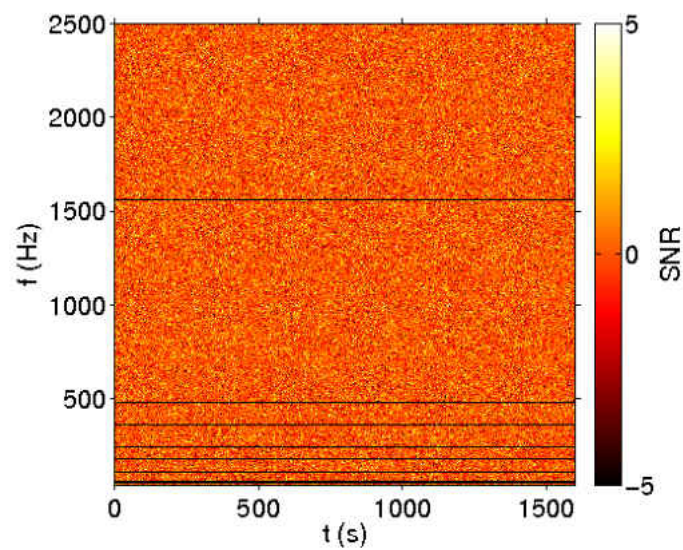


FIGURE 7.6. FT-map from STAMP for SGR trigger 2475.

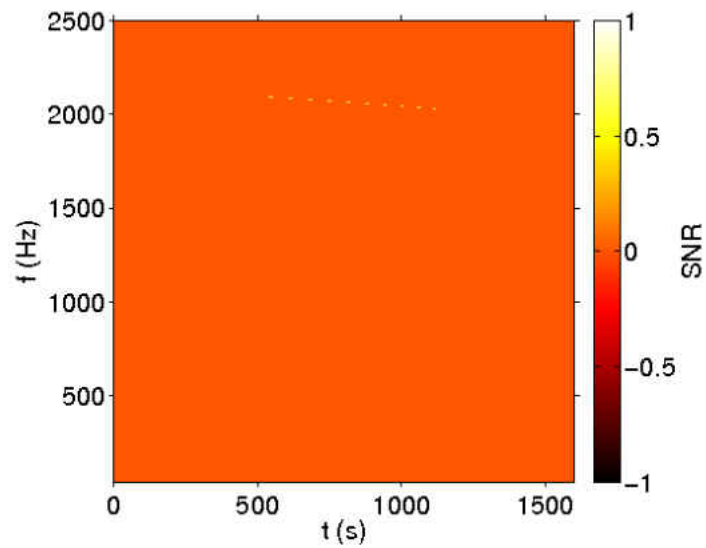


FIGURE 7.7. Loudest cluster found by STAMP's seedless clustering algorithm, stochtrack, for SGR trigger 2475.

7.2. Upper Limits

Upper limits were set on the energy of a GW that could exist without being detected in the data with this search. To find the upper limits, half sine-Gaussians were injected into 40 job-pairs, including the on-source. The 39 off-source job-pairs used had lower SNRs than the on-source. The detection efficiency for a particular injection was found by finding the percentage of injected waveforms that were recovered with SNR greater than the on-source SNR. Upper limits were found for detection efficiencies of 90% and 50%.

It is thought higher frequency QPOs may damp on sub-second timescales [94, 95]. In addition, higher frequency signals would need much more energy to be detectable. Therefore these upper limits focus on low frequencies. It was not assumed that magnetars would have a particular inclination angle during bursts or flares. As such, upper limits were set for a range of polarizations, discussed in more detail in Section 7.2.1.3. While SGR trigger 2471 and SGR trigger 2475 each had a single on-source SNR, SGR trigger 2469 had a different SNR with and without the absolute value SNR modification. For SGR trigger 2469, the on-source SNR of 5.73 (without the absolute value SNR modification) was used to calculate the upper limits with circular polarization and the SNR of 6.06 (with the absolute value SNR modification) was used to calculate the upper limits with the non-circular polarization.

Models for magnetar bursts and giant flares did not provide enough details to construct specific waveforms. As such, ad hoc sine-Gaussian waveforms were constructed with EM QPO observations used as a guide. It should be noted that the sine-Gaussian is a rough approximation, and that actual QPOs can vary more in both frequency and amplitude.

7.2.1. Waveform Parameters

The last half of a sine-Gaussian was used as the waveform type injected into the data. The length of the injected waveforms was equal to 3τ . In addition to the Gaussian envelope, a Hann window was applied to beginning and end of the signal: the beginning had the first half of a 2 second long Hann window applied and the end had the last half of the Hann window applied (making each half Hann window 1 second long).

A sine-Gaussian is of the form:

$$h_{SG}(t + t_0) = h_0 e^{-t^2/\tau^2} \sin(2\pi f_0 t) \quad (7.1)$$

The quality factor Q can be defined as:

$$Q = \sqrt{2} \pi \tau f_0 \quad (7.2)$$

(7.1) can be rewritten in terms of the quality factor in (7.2):

$$h_{SG}(t + t_0) = h_0 e^{-2\pi^2 f_0^2 t^2 / Q^2} \sin(2\pi f_0 t) \quad (7.3)$$

The equations for plus and cross polarizations of a sine-Gaussian waveform generated by a quadrupole are:

$$h_+ = \frac{h_0}{\sqrt{2}} e^{-t^2/\tau^2} \left(\frac{(1 + \cos^2 \iota)}{2} \cos(2\pi f_0 t) \cos 2\psi + (\cos \iota) \sin(2\pi f_0 t) \sin 2\psi \right) \quad (7.4)$$

$$h_\times = \frac{h_0}{\sqrt{2}} e^{-t^2/\tau^2} \left(-\frac{(1 + \cos^2 \iota)}{2} \cos(2\pi f_0 t) \sin 2\psi + (\cos \iota) \sin(2\pi f_0 t) \cos 2\psi \right) \quad (7.5)$$

ι is the inclination angle of the quadrupole and ψ is the polarization angle. The polarization angle is often included in the antenna factors. In such a case, the equations for h_+ and h_\times become:

$$h_+ = h_{+,\psi=0} = \frac{h_0}{\sqrt{2}} e^{-t^2/\tau^2} \frac{(1 + \cos^2 \iota)}{2} \cos(2\pi f_0 t) \quad (7.6)$$

$$h_\times = h_{\times,\psi=0} = \frac{h_0}{\sqrt{2}} e^{-t^2/\tau^2} (\cos \iota) \sin(2\pi f_0 t) \quad (7.7)$$

7.2.1.1. Characteristic Time

The τ in Table 7.2 were tested to determine which combination of τ and h_0 would produce the best (and lowest) energy upper limits. The total energy of the waveform was kept constant while τ and h_0 were varied ($E_{\text{GW}} \propto h_0^2 \times \tau = \text{constant}$). Waveforms with longer τ were recovered at lower energies. Two values of τ were chosen to cover both shorter and longer signals: $\tau = 150$ s and $\tau = 400$ s. Since longer τ were recovered with lower calculated energies, these τ can be thought of as setting rough upper limits for waveforms with longer τ , at least up to about 800 s as that was the longest τ tested. These durations were both on the order of observed EM QPO lengths, with 400 s being the longest observed QPO [57].

τ (s):	50, 100, 150, 200, 300, 400, 800
-------------	----------------------------------

TABLE 7.2. Initial values of τ to test.

7.2.1.2. Central Frequency

From reviewing the literature and discussions with Paul Lasky and James Clark, it was decided to focus on lower frequencies for the upper limits. In addition to much higher energies required for detection at higher frequencies, it is thought that any

high frequency modes will damp on sub-second timescales, which is not within the scope of this search [94, 95]. The frequency of 150 Hz was chosen to cover the most sensitive range of the detectors, and the frequencies of 450 Hz and 750 Hz were chosen to cover the lower-mid frequency range outside of the most sensitive frequency band. A summary of the parameters varied in the injections (besides h_0) can be found in Table 7.3.

τ (s):	150, 400
Frequency (Hz):	150, 450, 750

TABLE 7.3. Waveform parameters.

7.2.1.3. Polarization

The original intent was to put limits on the entire range of possible polarizations. Calculations of the h_{rss} suggest that circularly polarized signals would give the best energy upper limits and that linear polarizations would give energy upper limits approximately 8 times higher (see (B.37) and (B.38) in Appendix B). The actual sensitivity to the strain had much more variability. Upon injecting waveforms with different polarizations, it was found that some polarizations required a much larger strain to be recovered and some could not be recovered at all (discussed in detail in Section 7.3). Therefore, with the exception of SGR trigger 2471, upper limits were found for a subset of polarizations with decent SNR response.

The polarization with the best SNR response was the same for every trigger: $\iota = 0^\circ$ and $\psi = 0^\circ$. This was used to set the best upper limits for each trigger. The other polarizations used varied by trigger. The polarization used for SGR trigger 2471 was found using the data plotted in Figure 7.16. From this data, the minimum SNR response was estimated to occur at $\iota = 103^\circ$ (rounded to 3 significant figures). $\iota = 120^\circ$

($\cos \iota = -0.5$) was used for SGR triggers 2469 and 2475. This provides similar limits as those found for SGR trigger 2471 and covers approximately 2/3 of the polarizations as suggested by Figure 7.17 and an equivalent plot for SGR 2469. $\psi = 45^\circ$ was used for all cases as cross polarizations seem to have slightly smaller SNR responses than plus polarizations. The non-circular polarization angles are summarized in Table 7.4.

The set of values used for the parameters τ and f_0 were reduced when finding the upper limits for non-circular polarizations. As summarized in Table 7.5, only $\tau = 400$ s and $f_0 = 150$ Hz and $f_0 = 750$ Hz were used.

SGR Trigger	2469	2471	2475
ι	120°	103°	120°
ψ	45°	45°	45°

TABLE 7.4. Waveform parameters for non-circular polarizations. $\iota = 0^\circ$ and $\psi = 0^\circ$ were used for circular polarizations for all triggers.

τ (s):	400
Frequency (Hz):	150, 750

TABLE 7.5. Waveform parameters used for non-circular polarizations.

7.2.2. Upper Limit Methodology

The settings used by STAMP to find the upper limits were nearly the same as those described in Chapter VI. The differences are described below.

To avoid contamination from the loudest cluster in each job-pair, code was added to STAMP to set the pixels that made up the cluster to NaN, which are replaced with a value of 0 before calculating the cluster SNR. Once this was done, the SNR values without injected waveforms were much less loud than the threshold for the job-pairs that were used.

A new clustering algorithm known as “singletrack” was written and used for finding the upper limits. Singletrack uses a list of previously defined clusters and calculates the SNR for just those clusters, reducing the computational time of the analysis after the FT-maps are generated from order 30-45 minutes to order 10 seconds. For each trigger, a cluster or multiple clusters were found for each combination of frequency and characteristic time by running stochtrack on the set of 40 job-pairs (with loudest clusters removed) and using the output files for unique clusters which recovered the injected half sine-Gaussian. Singletrack uses a small subset of the clusters used by stochtrack, which guarantees that singletrack will not underestimate the amplitude of the upper limits. Singletrack may not always use the cluster that would recover the waveform at the lowest possible amplitude, but it is likely to at least recover the injection close to the lowest possible amplitude. Singletrack is very fast, but should only be used in cases where the final clusters can be known ahead of time and should not be used as a general algorithm to look for an unknown signal. It is meant for situational use such as recovering known injected waveforms.

As discussed in Section 7.3, some polarizations returned a negative SNR. Therefore singletrack was modified to calculate the absolute value of the SNR of the cluster by default. Singletrack can also be set to find the cluster with the largest magnitude SNR of either positive or negative sign.

In order to reduce any bias that may exist from using the same set of clusters from seeding stochtrack, the injection waveform can be injected into a random time for each individual instance. The injection start time ranges from the beginning of the window at -2 s to as close to the end of the window as possible with the waveform still completely contained within the window ($t_{\text{injection}} \in [t_{\text{start}}, (t_{\text{end}} - t_d)]$) where t_d is the duration of the injected waveform, t_{start} is the window start time, t_{end} is the window

end time and $t_{\text{injection}}$ is the injection start time). The waveforms were injected at 0 s in the window for circular polarization, and were injected at randomized start times as described for the polarizations in Table 7.4. The one exception for this is SGR trigger 2469 for $\tau = 400$ s: the waveform is injected at 0 s in the window because the waveform is longer than the window.

7.2.2.1. Procedure

In each of these steps, the amplitude h_0 is varied at even intervals in log space. The number of variations can change depending on the step. First a small number of jobs is used to quickly scan the parameter space of the amplitude and find where some of the waveforms are recovered. More jobs are added to improve the statistics and get closer to the desired detection efficiency, before finally using the maximum number of jobs to find the desired detection efficiency. Less jobs allow the parameter space to be searched quicker, but more jobs are needed for improved statistics.

The following steps are performed for each combination of parameters in both Table 7.3 and Table 7.5, except where noted:

1. h_0 is varied in log space evenly across 10 different points for two job-pairs, the on-source job-pair and one off-source job-pair. The standard limits for the amplitude in terms of h_0^2 are $[10^{-46}, 10^{-42}]$. In the case of the alternate polarizations, the limits may be adjusted to $[10^{-44}, 10^{-42}]$ or $[10^{-42}, 10^{-40}]$ instead because the recovery amplitude is worse. 20 total SNR values are calculated in this step.
2. The values of h_0 are focused around the values where the recovery switched from 0% to 100% in the previous step. 10 job-pairs, including the on-source, are used in this step for each value of h_0 . Four values of h_0 are spaced evenly in log space.

- 40 SNR values are calculated in this step. This step was adjusted and repeated as necessary to get close to the desired detection efficiencies.
3. h_0 was varied in log space again, this time for all 40 job-pairs, including the on-source job-pair. h_0 was varied around the 90% threshold from the previous step, or the points close to it. Four values for h_0 is standard for the initial implementation of this step (five was sometimes used instead). 160 SNR values are calculated in this step (or 200 if five values are used). This step was sometimes repeated if values surrounding either the 90% or 50% threshold were not found.
 - In the case of the upper limits for waveforms with non-circular polarization, this step was repeated until values above and below 50% and 90% were close enough to linearly interpolate the thresholds in $\log(h_0)$ versus efficiency space (in some cases the 50% and/or 90% thresholds were directly found by chance). The polarizations used are described in Table 7.4. These were done for each trigger for each combination of the parameters in Table 7.5.
 4. This step was used for circularly polarized waveform upper-limits only ($\iota = 0$ and $\psi = 0$ for each combination of parameters in Table 7.3). 40 job-pairs are again used, including the on-source. Nearly identical to the previous step, with the difference that only 2 values of h_0 are used (80 SNR values calculated). This step is repeated until both 50% and 90% of the injections are recovered with SNR greater than the threshold SNR.

7.2.3. Upper limit calculation

These upper limit calculations are for a half sine-Gaussian waveform as presented in (7.4) and (7.5). The half Hann windows applied to the start and end of the

waveforms are ignored, and the duration of the waveform is approximated as infinite instead of 3τ . This leads to upper limits which are an upper bound on the energy in each waveform. The differences should be negligible, on order of 1% at most for the shorter waveforms, and less for the longer waveforms.

The root sum square strain of a signal is:

$$h_{rss} = \sqrt{\int_{-\infty}^{\infty} |h|^2 dt} \quad (7.8)$$

where $|h|^2 = |h_+|^2 + |h_\times|^2$. For the last half of a sine-Gaussian waveform of the form in (7.4) and (7.5), h_{rss} is:

$$h_{rss} = \frac{h_0}{4\pi^{1/4}} \sqrt{\frac{Q}{f_0}} \sqrt{\left(\frac{(1 + \cos^2 \iota)^2}{4} + \cos^2 \iota\right) + \left(\frac{(1 + \cos^2 \iota)^2}{4} - \cos^2 \iota\right) e^{-Q^2}} \quad (7.9)$$

For high Q , this is:

$$h_{rss}^{\text{HQ}} \approx \frac{h_0}{4\pi^{1/4}} \sqrt{\frac{Q}{f_0}} \sqrt{\left(\frac{(1 + \cos^2 \iota)^2}{4} + \cos^2 \iota\right)} \quad (7.10)$$

The GW energy for a half sine-Gaussian is:

$$E_{\text{GW}} = h_0^2 r^2 Q f_0 \frac{c^3 \pi^{3/2}}{20 G} \left[1 + \frac{1}{2Q^2} \left(1 + \frac{1}{6} e^{-Q^2} \right) \right] \quad (7.11)$$

For high Q , (7.11) can be approximated as:

$$E_{\text{GW}}^{\text{HQ}} \approx \frac{c^3 \pi^{3/2}}{20 G} h_0^2 r^2 Q f_0 \quad (7.12)$$

For the h_{rss} and E_{GW} of a full sine-Gaussian waveform, simply multiply (7.9) and (7.10) by $\sqrt{2}$ and multiply (7.11) and (7.12) by 2. (7.9), (7.10), (7.11) and (7.12) are calculated in detail in Appendix B.

7.2.4. Calibration Error

The measured cross-correlated signal $h_{0\text{m}1}h_{0\text{m}2}$ has uncertainties due to calibration error. The detector differential arm lengths are measured in voltage counts. Measurements must be made on different systems within the detector to measure the conversion from these voltage counts to actual strain values. The conversion function is known as the calibration. Errors in the calibration propagate into error in the measured value of the strain. The calibration errors can be grouped into an overall scaling error A , a frequency dependent amplitude error, a frequency dependent phase error δ and a timing error. The timing error is effectively a linear frequency dependent phase error.

The effect of the calibration error on the measured strain value can be estimated with two extremes. The first extreme would be the most sensitive to a potential signal (the scaling error is δA_- , the phase errors of each detector cancel out and the timing error is zero):

$$\frac{h_{01}h_{02}}{h_{0m1}h_{0m2}} = A_1A_2 \left(1 - \sqrt{\delta A_{-1}^2 + \delta A_{-2}^2 + |\Delta h_1(t)|^2 + |\Delta h_2(t)|^2} \right) \quad (7.13)$$

In the other extreme, the calibration error leads to an underestimation of the strength of a potential signal (the scaling error is δA_+ , the phase error of the detectors would be of the same sign with maximum timing error):

$$\frac{h_{01}h_{02}}{h_{0m1}h_{0m2}} = A_1A_2 \frac{1 + \sqrt{\delta A_{+1}^2 + \delta A_{+2}^2 + |\Delta h_1(t)|^2 + |\Delta h_2(t)|^2}}{\cos(2\pi f 45\mu s + \delta_1(t) + \delta_2(t))} \quad (7.14)$$

For detailed derivations of (7.13) and (7.14) and specific numbers on the different calibration errors, see Appendix C. In order to set conservative upper limits, the calibration error in (7.14) was assumed. To account for the calibration error in the energy upper limits, E_{GW} was multiplied by the ratio in (7.14). Similarly, h_{rss} was multiplied by the square root of this ratio.

7.2.5. Summary of Upper Limits

The results for circularly polarized signals (with $\iota = 0^\circ$ and $\psi = 0^\circ$) are summarized in Table 7.6 for a 90% confidence level (CL) and Table 7.7 for 50% CL. The 50% CL results for h_{rss} are shown again in Table 7.8 with the associated calibration error shown as a percentage of h_{rss} . Results for the alternate polarizations listed in Table 7.4 are summarized in Table 7.9 and Table 7.10 for 90% and 50% CL respectively. The limits assume a fixed source distance and are set in terms of h_{rss} and

E_{GW} . The calibration error leads to a 15%–21% increase in the strain upper limits (32%–46% increase in energy upper limits). The tables include the upper limits for h_{rss} and E_{GW} both with and without the calibration error.

The detection efficiency is plotted against the strain h_0 for each combination of τ and f_0 in Figure 7.8, Figure 7.9 and Figure 7.10 for SGR trigger 2469, 2471 and 2475 respectively. The shaded area around each curve is found from calculating the expectation value for Bayesian posterior probability for a Poisson process with 40 trials and taking the $1\text{-}\sigma$ width for the posterior probability.

The same plots are remade for the waveforms using the alternate polarizations with reduced SNR response in Figure 7.11, Figure 7.12 and Figure 7.13. Figure 7.14 shows how the SNR response changes with the strain. The on-source can be seen to be within the distribution of background points on this plot (this was also true for plots made for the other parameter combinations).

From these plots, it can be seen that better upper limits were set for longer τ and frequencies within LIGO’s most sensitive band. It is expected that as the frequency decreases from LIGO’s most sensitive band, the upper limit values will decrease. This is supported by the LIGO noise curve, as well as an upper limit which was run for SGR trigger 2469 for $f_0 = 100\text{ Hz}$ and $\tau = 150\text{ Hz}$ which was recovered at a higher h_0 value than its $f_0 = 150\text{ Hz}$ counterpart with the same τ . As the frequency increases above LIGO’s most sensitive frequency band and as τ decreases, the upper limit values increase.

f_0	τ	h_0	h_{rss}	h_{rss} cal err	Distance	E_{GW}	E_{GW} cal err
Hz	s		$s^{1/2}$	$s^{1/2}$	kpc	erg	erg
SGR trigger 2469							
150		1.07×10^{-22}	2.39×10^{-21}	2.74×10^{-21}	8.7	1.18×10^{46}	1.55×10^{46}
450	400	1.76×10^{-22}	3.95×10^{-21}	4.60×10^{-21}		2.89×10^{47}	3.91×10^{47}
750		2.26×10^{-22}	5.07×10^{-21}	6.02×10^{-21}		1.32×10^{48}	1.86×10^{48}
150		2.85×10^{-22}	3.90×10^{-21}	4.47×10^{-21}		3.13×10^{46}	4.12×10^{46}
450	150	3.87×10^{-22}	5.31×10^{-21}	6.18×10^{-21}		5.22×10^{47}	7.08×10^{47}
750		4.80×10^{-22}	6.58×10^{-21}	7.81×10^{-21}		2.22×10^{48}	3.13×10^{48}
SGR trigger 2471							
150		1.58×10^{-22}	3.53×10^{-21}	4.14×10^{-21}	8.7	2.56×10^{46}	3.52×10^{46}
450	400	3.30×10^{-22}	7.39×10^{-21}	8.79×10^{-21}		1.01×10^{48}	1.43×10^{48}
750		3.87×10^{-22}	8.67×10^{-21}	1.05×10^{-20}		3.87×10^{48}	5.66×10^{48}
150		6.71×10^{-22}	9.20×10^{-21}	1.08×10^{-20}		1.74×10^{47}	2.39×10^{47}
450	150	1.10×10^{-21}	1.50×10^{-20}	1.79×10^{-20}		4.18×10^{48}	5.90×10^{48}
750		1.34×10^{-21}	1.84×10^{-20}	2.23×10^{-20}		1.74×10^{49}	2.55×10^{49}
SGR trigger 2475							
150		8.66×10^{-23}	1.94×10^{-21}	2.27×10^{-21}	8.5	7.38×10^{45}	1.01×10^{46}
450	400	1.41×10^{-22}	3.16×10^{-21}	3.76×10^{-21}		1.77×10^{47}	2.49×10^{47}
750		2.07×10^{-22}	4.64×10^{-21}	5.62×10^{-21}		1.06×10^{48}	1.55×10^{48}
150		3.81×10^{-22}	5.22×10^{-21}	6.12×10^{-21}		5.35×10^{46}	7.36×10^{46}
450	150	4.10×10^{-22}	5.62×10^{-21}	6.68×10^{-21}		5.58×10^{47}	7.89×10^{47}
750		5.87×10^{-22}	8.05×10^{-21}	9.75×10^{-21}		3.18×10^{48}	4.66×10^{48}

TABLE 7.6. Upper limits for 90% CL for circularly polarized signals with $\iota = 0^\circ$ and $\psi = 0^\circ$.

f_0	τ	h_0	h_{rss}	h_{rss} cal err	Distance	E_{GW}	E_{GW} cal err
Hz	s		$s^{1/2}$	$s^{1/2}$	kpc	erg	erg
SGR trigger 2469							
150		9.38×10^{-23}	2.10×10^{-21}	2.41×10^{-21}	8.7	9.07×10^{45}	1.19×10^{46}
450	400	1.50×10^{-22}	3.37×10^{-21}	3.92×10^{-21}		2.10×10^{47}	2.84×10^{47}
750		1.94×10^{-22}	4.35×10^{-21}	5.17×10^{-21}		9.73×10^{47}	1.37×10^{48}
150		2.24×10^{-22}	3.08×10^{-21}	3.53×10^{-21}		1.94×10^{46}	2.56×10^{46}
450	150	3.25×10^{-22}	4.45×10^{-21}	5.18×10^{-21}		3.67×10^{47}	4.97×10^{47}
750		4.18×10^{-22}	5.74×10^{-21}	6.81×10^{-21}		1.69×10^{48}	2.38×10^{48}
SGR trigger 2471							
150		1.17×10^{-22}	2.62×10^{-21}	3.07×10^{-21}	8.7	1.41×10^{46}	1.94×10^{46}
450	400	2.69×10^{-22}	6.03×10^{-21}	7.17×10^{-21}		6.73×10^{47}	9.51×10^{47}
750		3.00×10^{-22}	6.72×10^{-21}	8.13×10^{-21}		2.32×10^{48}	3.40×10^{48}
150		4.18×10^{-22}	5.74×10^{-21}	6.73×10^{-21}		6.77×10^{46}	9.30×10^{46}
450	150	7.14×10^{-22}	9.79×10^{-21}	1.16×10^{-20}		1.77×10^{48}	2.51×10^{48}
750		9.27×10^{-22}	1.27×10^{-20}	1.54×10^{-20}		8.31×10^{48}	1.22×10^{49}
SGR trigger 2475							
150		7.58×10^{-23}	1.70×10^{-21}	1.99×10^{-21}	8.5	5.66×10^{45}	7.78×10^{45}
450	400	1.12×10^{-22}	2.51×10^{-21}	2.98×10^{-21}		1.11×10^{47}	1.57×10^{47}
750		1.64×10^{-22}	3.68×10^{-21}	4.46×10^{-21}		6.66×10^{47}	9.74×10^{47}
150		2.45×10^{-22}	3.36×10^{-21}	3.94×10^{-21}		2.21×10^{46}	3.04×10^{46}
450	150	3.05×10^{-22}	4.18×10^{-21}	4.97×10^{-21}		3.09×10^{47}	4.37×10^{47}
750		4.82×10^{-22}	6.61×10^{-21}	8.00×10^{-21}		2.15×10^{48}	3.14×10^{48}

TABLE 7.7. Upper limits for 50% CL for circularly polarized signals with $\iota = 0^\circ$ and $\psi = 0^\circ$.

f_0	τ	h_0	Distance	h_{rss}	h_{rss} cal err	Cal err percent
Hz	s		kpc	$s^{1/2}$	$s^{1/2}$	%
SGR trigger 2469						
150		9.38×10^{-23}	8.7	2.10×10^{-21}	2.41×10^{-21}	15.0
450	400	1.50×10^{-22}		3.37×10^{-21}	3.92×10^{-21}	16.0
750		1.94×10^{-22}		4.35×10^{-21}	5.17×10^{-21}	19.0
150		2.24×10^{-22}	8.7	3.08×10^{-21}	3.53×10^{-21}	15.0
450	150	3.25×10^{-22}		4.45×10^{-21}	5.18×10^{-21}	16.0
750		4.18×10^{-22}		5.74×10^{-21}	6.81×10^{-21}	19.0
SGR trigger 2471						
150		1.17×10^{-22}	8.7	2.62×10^{-21}	3.07×10^{-21}	17.0
450	400	2.69×10^{-22}		6.03×10^{-21}	7.17×10^{-21}	19.0
750		3.00×10^{-22}		6.72×10^{-21}	8.13×10^{-21}	21.0
150		4.18×10^{-22}	8.7	5.74×10^{-21}	6.73×10^{-21}	17.0
450	150	7.14×10^{-22}		9.79×10^{-21}	1.16×10^{-20}	19.0
750		9.27×10^{-22}		1.27×10^{-20}	1.54×10^{-20}	21.0
SGR trigger 2475						
150		7.58×10^{-23}	8.5	1.70×10^{-21}	1.99×10^{-21}	17.0
450	400	1.12×10^{-22}		2.51×10^{-21}	2.98×10^{-21}	19.0
750		1.64×10^{-22}		3.68×10^{-21}	4.46×10^{-21}	21.0
150		2.45×10^{-22}	8.5	3.36×10^{-21}	3.94×10^{-21}	17.0
450	150	3.05×10^{-22}		4.18×10^{-21}	4.97×10^{-21}	19.0
750		4.82×10^{-22}		6.61×10^{-21}	8.00×10^{-21}	21.0

TABLE 7.8. Upper limits for 50% CL for circularly polarized signals with $\iota = 0^\circ$ and $\psi = 0^\circ$ with percentage from calibration error.

f_0	τ	h_0	h_{rss}	h_{rss} cal err	Distance	E_{GW}	E_{GW} cal err
Hz	s		$s^{1/2}$	$s^{1/2}$	kpc	erg	erg
SGR trigger 2469 ($\iota = 120^\circ$)							
150	400	2.56×10^{-22}	5.72×10^{-21}	6.56×10^{-21}	8.7	6.73×10^{46}	8.85×10^{46}
750	400	1.50×10^{-21}	3.36×10^{-20}	3.99×10^{-20}	8.7	5.80×10^{49}	8.17×10^{49}
SGR trigger 2471 ($\iota = 103^\circ$)							
150	400	7.10×10^{-22}	1.59×10^{-20}	1.86×10^{-20}	8.7	5.19×10^{47}	7.14×10^{47}
750	400	2.35×10^{-21}	5.26×10^{-20}	6.37×10^{-20}	8.7	1.42×10^{50}	2.08×10^{50}
SGR trigger 2475 ($\iota = 120^\circ$)							
150	400	2.90×10^{-22}	6.50×10^{-21}	7.62×10^{-21}	8.5	8.30×10^{46}	1.14×10^{47}
750	400	1.83×10^{-21}	4.09×10^{-20}	4.95×10^{-20}	8.5	8.21×10^{49}	1.20×10^{50}

TABLE 7.9. Upper limits for 90% CL for signals with polarization described in Table 7.4.

f_0	τ	h_0	h_{rss}	h_{rss} cal err	Distance	E_{GW}	E_{GW} cal err
Hz	s		$s^{1/2}$	$s^{1/2}$	kpc	erg	erg
SGR trigger 2469 ($\iota = 120^\circ$)							
150	400	2.17×10^{-22}	4.87×10^{-21}	5.58×10^{-21}	8.7	4.88×10^{46}	6.41×10^{46}
750	400	1.03×10^{-21}	2.31×10^{-20}	2.74×10^{-20}	8.7	2.75×10^{49}	3.87×10^{49}
SGR trigger 2471 ($\iota = 103^\circ$)							
150	400	4.85×10^{-22}	1.09×10^{-20}	1.27×10^{-20}	8.7	2.43×10^{47}	3.34×10^{47}
750	400	1.66×10^{-21}	3.73×10^{-20}	4.51×10^{-20}	8.7	7.14×10^{49}	1.05×10^{50}
SGR trigger 2475 ($\iota = 120^\circ$)							
150	400	2.35×10^{-22}	5.27×10^{-21}	6.18×10^{-21}	8.5	5.45×10^{46}	7.50×10^{46}
750	400	8.80×10^{-22}	1.97×10^{-20}	2.38×10^{-20}	8.5	1.91×10^{49}	2.79×10^{49}

TABLE 7.10. Upper limits for 50% CL for signals with polarization described in Table 7.4.

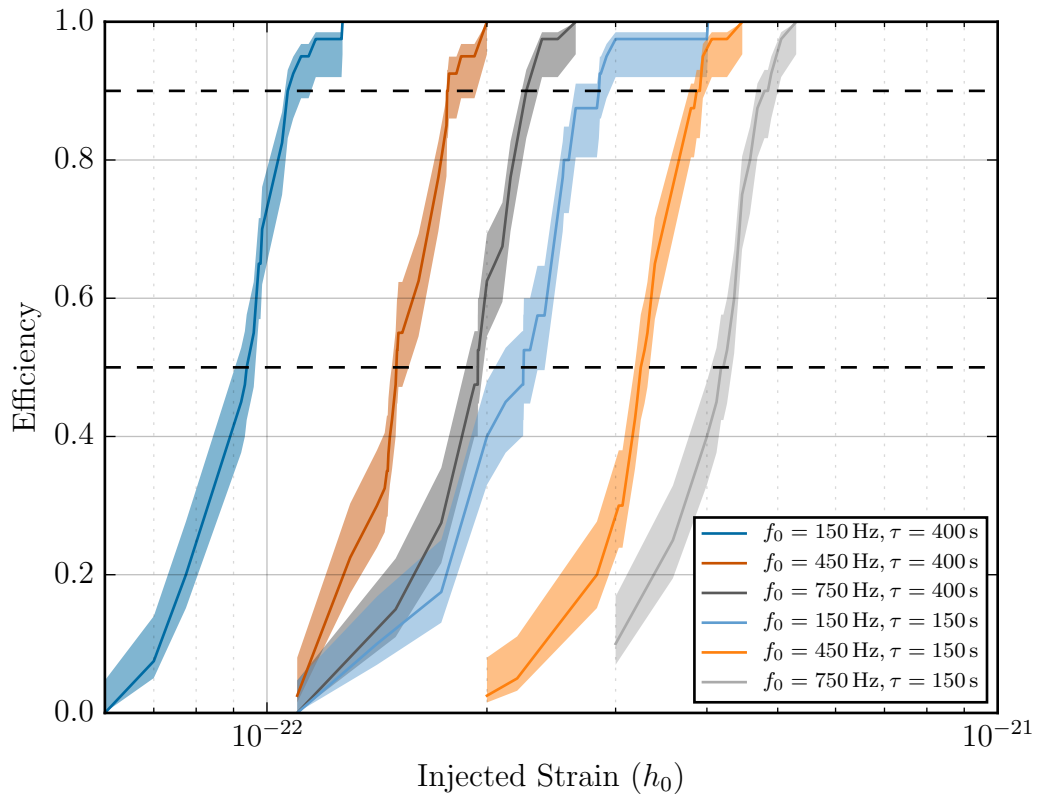


FIGURE 7.8. Detection efficiency vs injected strain h_0 for SGR trigger 2469. Waveforms are circularly polarized with $\iota = 0^\circ$ and $\psi = 0^\circ$.

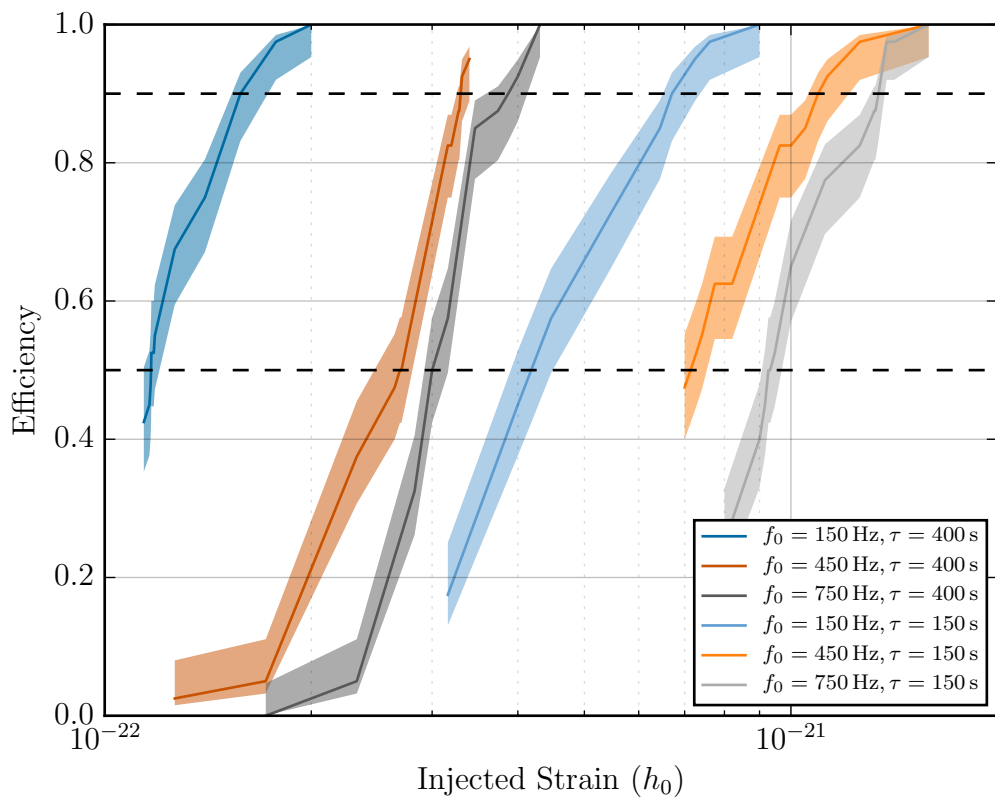


FIGURE 7.9. Plot of the detection efficiency vs injected strain h_0 for SGR trigger 2471. Waveforms are circularly polarized with $\iota = 0^\circ$ and $\psi = 0^\circ$.

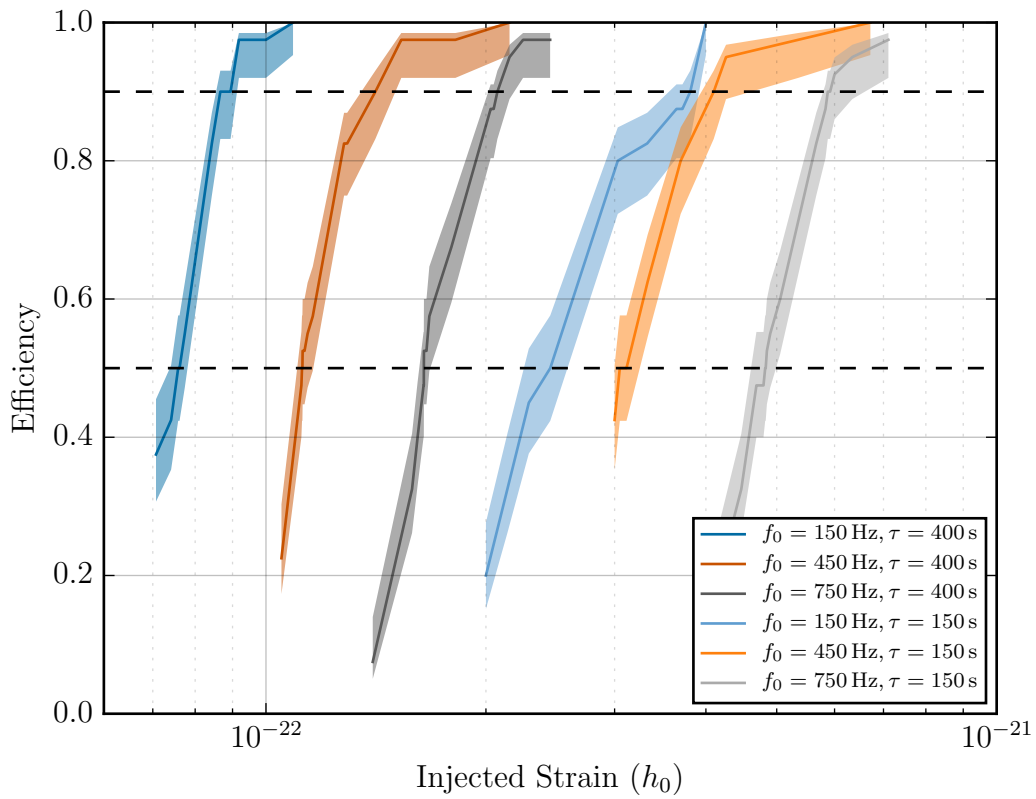


FIGURE 7.10. Plot of the detection efficiency vs injected strain h_0 for SGR trigger 2475. Waveforms are circularly polarized with $\iota = 0^\circ$ and $\psi = 0^\circ$.

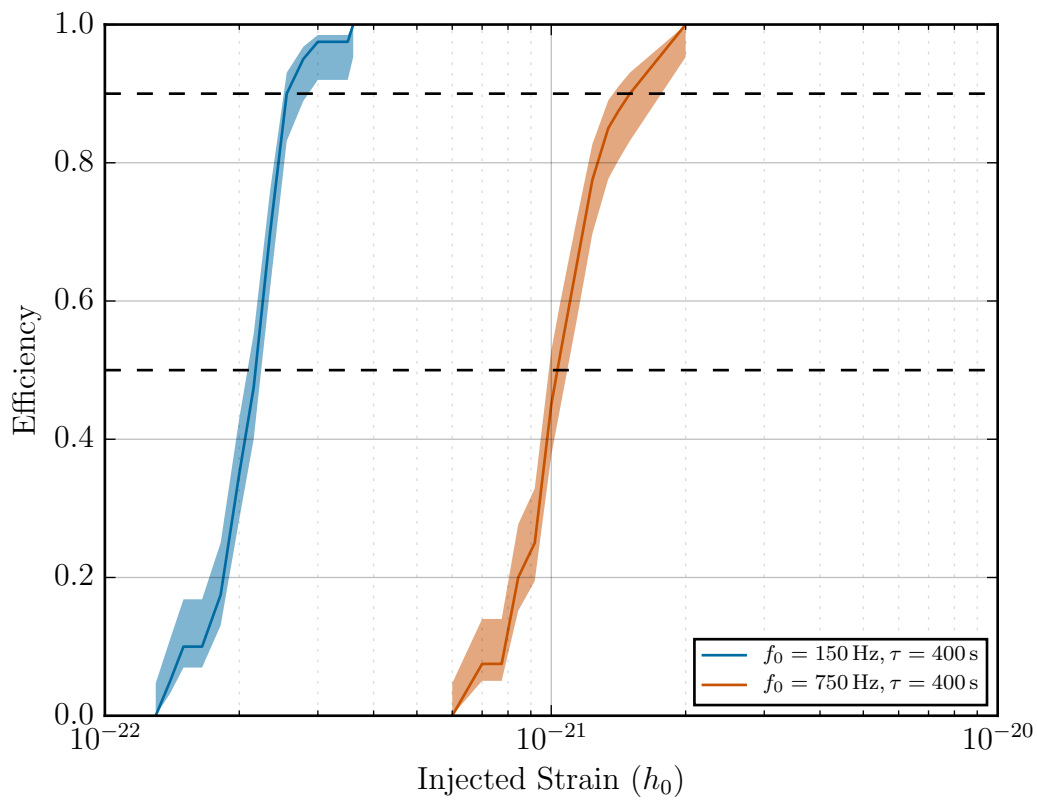


FIGURE 7.11. Detection efficiency vs injected strain h_0 for SGR trigger 2469. Waveforms calculated for $\iota = 120^\circ$ and $\psi = 45^\circ$.

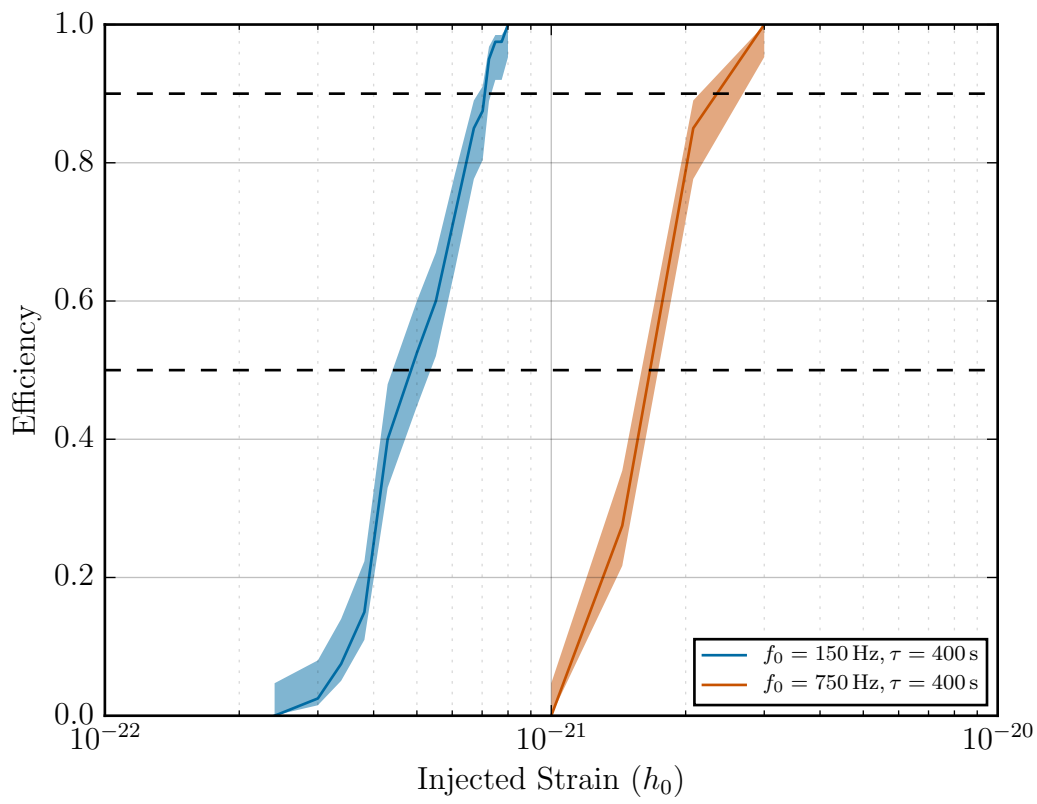


FIGURE 7.12. Plot of the detection efficiency vs injected strain h_0 for SGR trigger 2471. Waveforms calculated for $\iota = 103^\circ$ and $\psi = 45^\circ$.

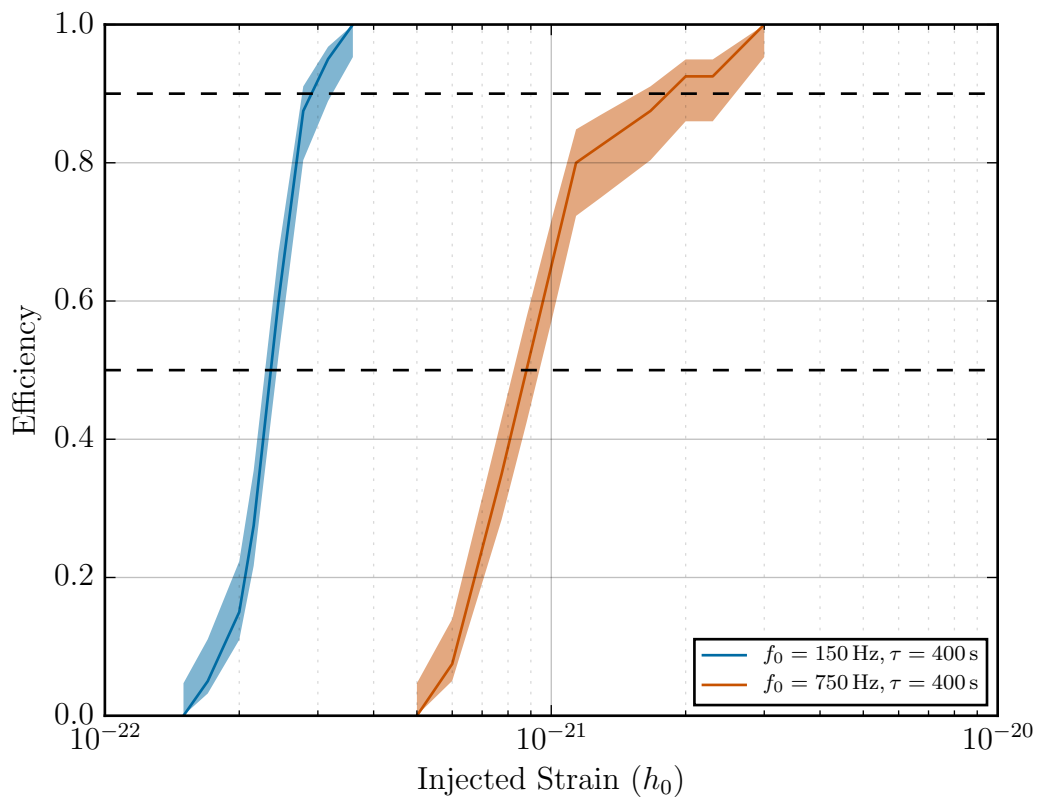


FIGURE 7.13. Plot of the detection efficiency vs injected strain h_0 for SGR trigger 2475. Waveforms calculated for $\iota = 120^\circ$ and $\psi = 45^\circ$.

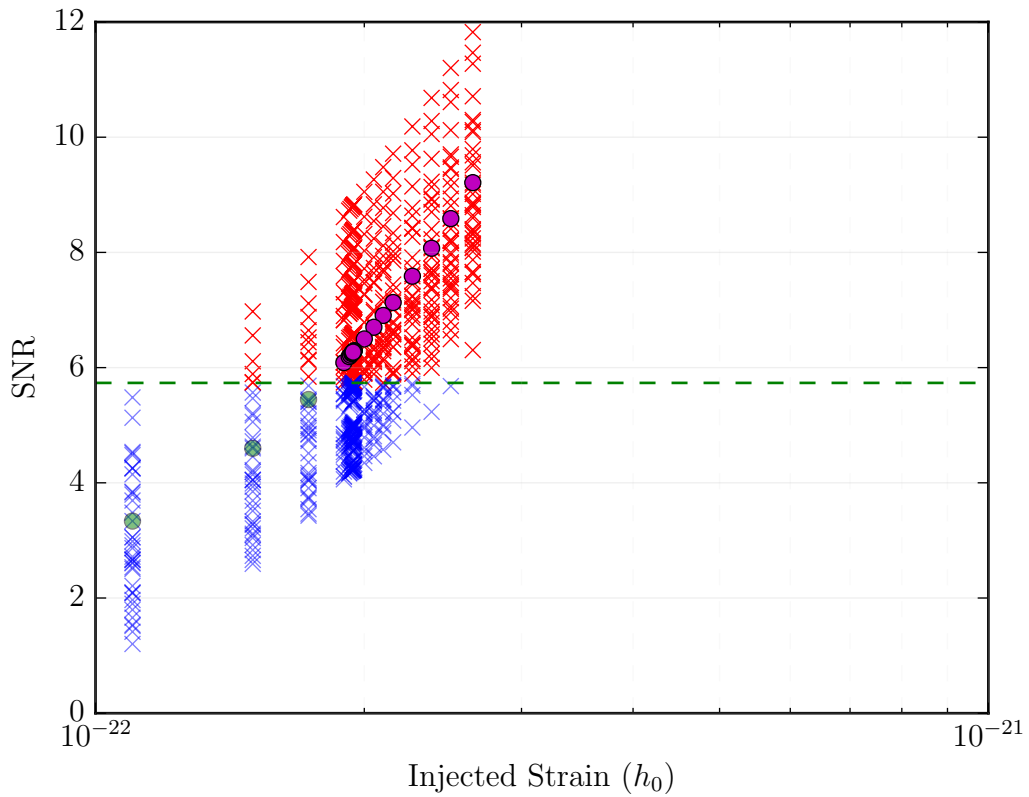


FIGURE 7.14. SNR response to injected strain h_0 for $f_0 = 750$ Hz, $\tau = 400$ s, circularly polarized signal for trigger 2469. The on-source job-pair is represented by a circle at different values of h_0 . The dashed green line is the on-source SNR used as the threshold for recovered injections.

7.3. Absolute Value SNR Modification

In the process of calculating the upper limits as detailed in Section 7.2.2, it was found that the search algorithm was not sensitive to all waveform polarizations. SGR triggers 2469 and 2475 were found to have a negative SNR response to linear injected signals of either plus or cross polarization. This is illustrated in Figure 7.15 for SGR trigger 2475; SGR trigger 2469 had a similar response. It is likely that this is due to the polarization filter used, as a previous study by Eric Thrane and Tanner Prestegard had found that the unpolarized polarization filter used by STAMP could cause a negative SNR for a fraction of the possible sky direction, inclination and polarization combinations (perhaps around 10%). SGR trigger 2471 had a positive SNR response to all tested polarizations, which included circular, plus and cross polarizations (see Figure 7.16).

The SNR response to polarization was tested by varying both the polarization angle ψ and the inclination angle ι of the chosen injection waveform. The waveform used was the half sine-Gaussian described in Section 7.2.1. Two values were used for the polarization angle ($\psi = 0^\circ$ and $\psi = 45^\circ$), and 79 values for ι were used for this test. For both $\psi = 0^\circ$ and $\psi = 45^\circ$, $\cos \iota$ was varied at evenly spaced intervals across 79 points over the interval $\cos \iota = [-1, 1]$. All three triggers returned positive SNRs for circularly polarized waveforms.

To mitigate the sensitivity loss due to the negative SNR response, the clustering algorithm was changed to calculate the absolute value of the SNR (previously it took the largest positive value, effectively ignoring all negative SNRs). This successfully returned sensitivity to the linear polarizations as illustrated for SGR trigger 2475 in Figure 7.17. It is notable that while this improved the range of polarizations the search was sensitive to, there are still some polarizations which remain undetectable.

It can be seen from Figure 7.15 that the SNR response becomes very small and crosses zero as it goes from positive SNR to negative and vice versa. Polarizations with a small SNR magnitude remain undetectable for realistic waveforms. Section 7.2 details the upper limits for a range of polarizations.

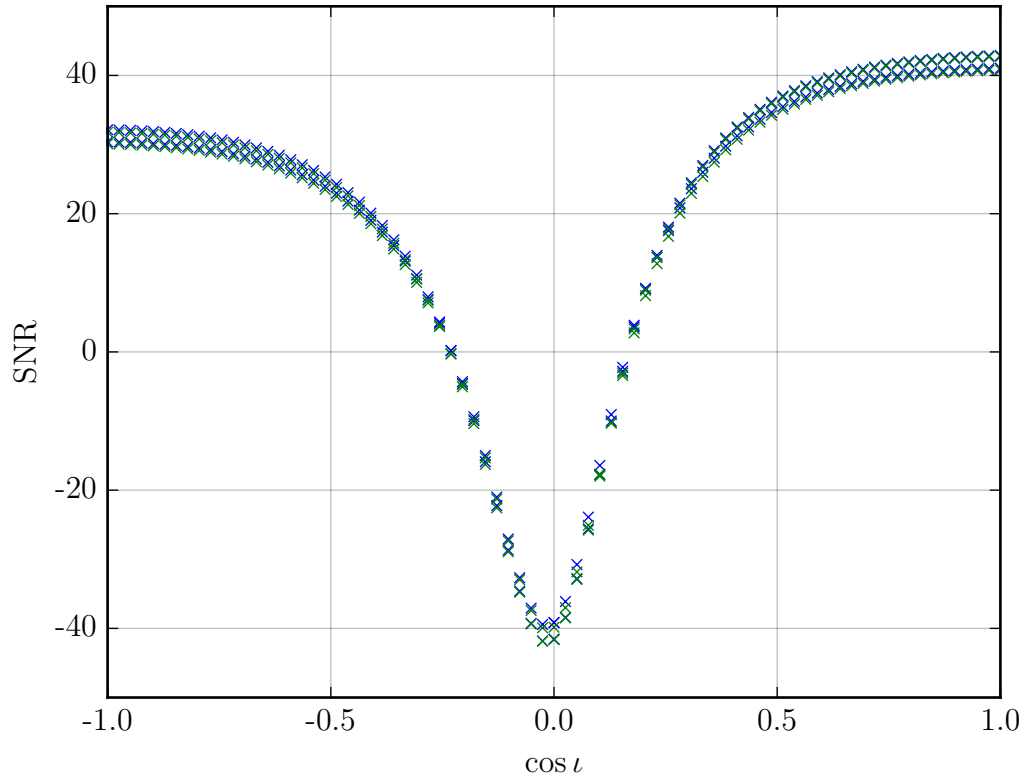


FIGURE 7.15. SNR vs $\cos \iota$ for SGR trigger 2475. The SNRs for the on-source and one off-source job pair are plotted for each color. The blue points vary at equal intervals across $\cos \iota$ for $\psi = 0^\circ$, which means when $\cos \iota = 0$ the waveform is linearly polarized in the plus polarization. The green points also vary across $\cos \iota$ but for $\psi = 45^\circ$, which makes $\cos \iota = 0$ a cross polarization waveform. There are 79 values of $\cos \iota$ plotted, ranging from circular polarization at $\cos \iota = 1$ to plus or cross polarization at $\cos \iota = 0$, back to circular polarization in the opposite rotation at $\cos \iota = -1$. SGR trigger 2475, like SGR 2469, has a negative SNR near $\cos \iota = 0$. It should be noted that this plot was made for an unrealistically large strain h_0 for the purposes of clearly observing the sign of the strain. The waveform used had $f_0 = 150$ Hz and $\tau = 400$ s.

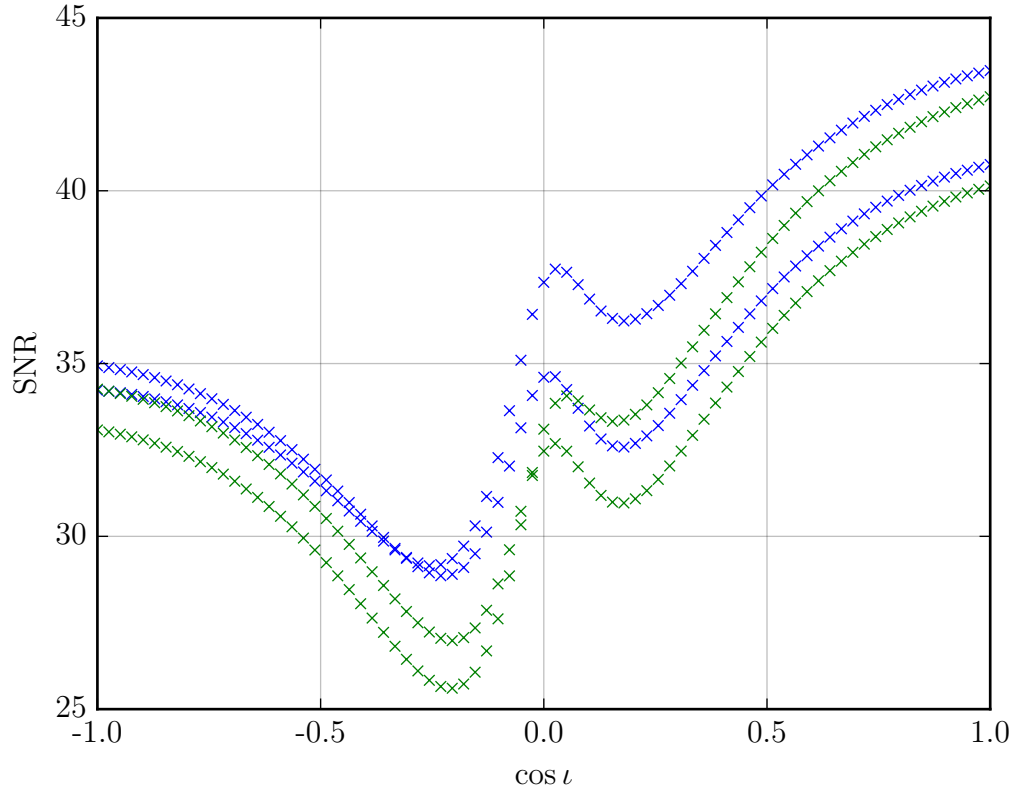


FIGURE 7.16. SNR vs $\cos \iota$ for SGR trigger 2471. The SNRs for the on-source and one off-source job pair are plotted for each color. The blue points vary at equal intervals across $\cos \iota$ for $\psi = 0^\circ$, which means when $\cos \iota = 0$ the waveform is linearly polarized in the plus polarization. The green points also vary across $\cos \iota$ but for $\psi = 45^\circ$, which makes $\cos \iota = 0$ a cross polarization waveform. There are 79 values of $\cos \iota$ plotted, ranging from circular polarization at $\cos \iota = 1$ to plus or cross polarization at $\cos \iota = 0$, back to circular polarization in the opposite rotation at $\cos \iota = -1$. It is notable that SGR trigger 2471 has a positive SNR for all polarizations. It should be noted that this plot was made for an unrealistically large strain h_0 for the purposes of clearly observing the sign of the strain. The waveform used had $f_0 = 150$ Hz and $\tau = 400$ s. The minimum SNR response occurs at approximately $\iota = 103^\circ$.

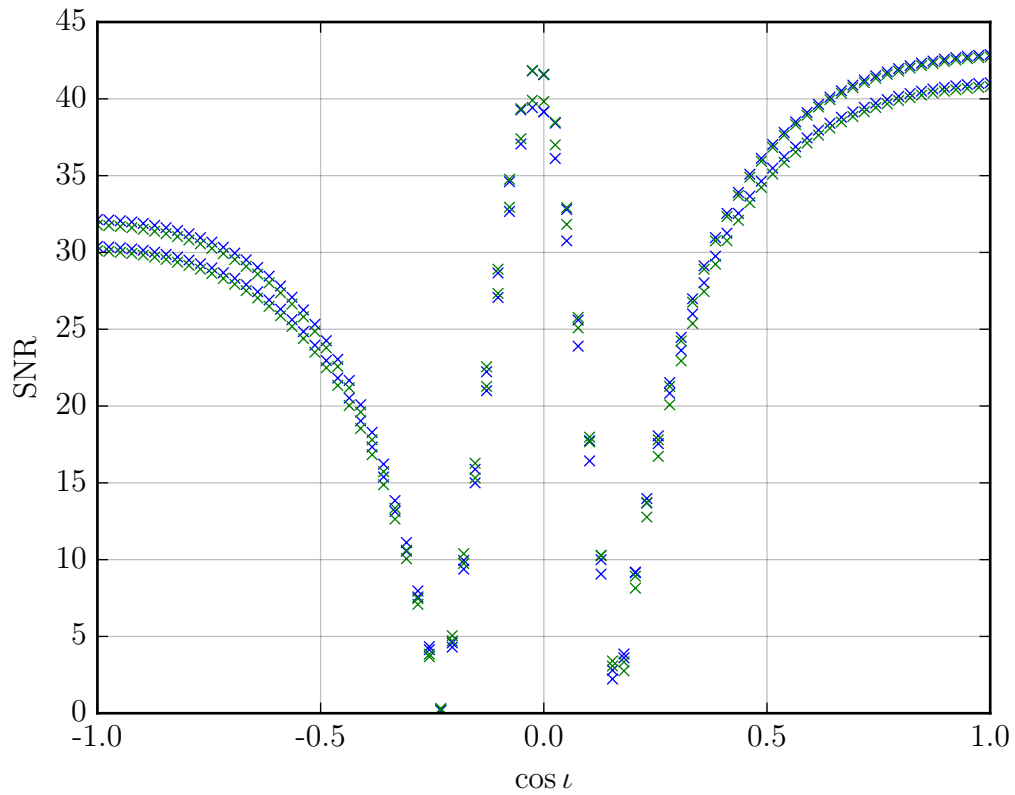


FIGURE 7.17. SNR vs $\cos \iota$ for SGR trigger 2475 with absolute value SNR modification. The SNR near $\cos \iota = 0$ is now positive. There are still two areas of low sensitivity where the SNR goes to zero, but sensitivity to the negative SNRs have been regained.

CHAPTER VIII

SUMMARY AND CONCLUSIONS

This analysis was a directed search for unmodeled long-duration transient GWs related to magnetar bursts. Magnetars are neutron stars with very strong magnetic fields, with inferred external fields of $\sim 10^{13}$ – 10^{15} gauss (up to ~ 1000 times stronger than the estimated magnetic fields in pulsars which have typical inferred values of $\sim 10^{12}$ gauss) [64, 72]. The search looked for evidence for GWs related to bursts that occurred during LIGO’s sixth science run, from July 2009 to October 2010, during which there were three magnetar bursts that occurred while both H1 and L1 were active and in science mode. No gravitational wave candidate was observed in this search. GW energy upper limits were estimated on the observed bursts.

The three bursts were from two source objects: SGR 1806-20 and 1E 1841-045, an SGR and AXP. SGRs are astronomical objects that emit intermittent bursts of gamma rays and X-rays. AXPs are astronomical objects with persistent X-ray emission, but lack the companion object that normally powers X-ray pulsars through accretion (hence the term anomalous). AXPs have been observed to emit bursts similar to those emitted by SGRs, leading observers to conclude that they are also magnetars [57].

SGR 1806-20 is a particularly interesting SGR. It was the first SGR ever discovered to emit bursts, emitting the first detected burst in January of 1979. It has the largest inferred magnetic field of any known object, with an estimated external field of 2×10^{15} gauss [62, 65, 66]. It also hit the earth with the highest radiation flux of any event detected from outside our solar system: the hyperflare of December 27, 2004, which was 100 times more energetic than the other giant flares observed [66].

Upper limits on possible GW amplitude and energy were placed for several variations of half sine-Gaussian waveforms for each of the three bursts in this search. The first two bursts were from SGR 1806-20 and the third burst was from 1E 1841-045. As discussed in detail in Chapter VII, the best upper limit $E_{\text{GW}} = 1.01 \times 10^{46}$ erg was placed on the burst from 1E 1841-045 (SGR trigger 2475) for a circularly polarized half sine-Gaussian with central frequency $f_0 = 150$ Hz and characteristic time $\tau = 400$ s. The best upper limit placed on bursts from SGR 1806-20 was on the first burst (SGR trigger 2469) using the same waveform with a gravitational wave energy upper limit $E_{\text{GW}} = 1.55 \times 10^{46}$ erg. The best upper limit on the other burst (SGR trigger 2471) was $E_{\text{GW}} = 3.52 \times 10^{46}$ erg using the same waveform.

There are several different astrophysical parameters with which the upper limits of this search can be compared. E_{GW} can be compared to the energy of the star's mass. Assuming a neutron star with mass $m = 1.4 M_\odot$ ($1 M_\odot = (1.98855 \pm 0.00025) \times 10^{30}$ kg $\approx 2 \times 10^{30}$ kg), the equivalent energy from the mass of the star would be:

$$E = mc^2 \tag{8.1}$$

$$E_{1.4M_\odot} = 1.4 \times (2 \times 10^{30} \text{ kg}) \times (3 \times 10^8 \text{ m/s})^2 = 2.52 \times 10^{47} \text{ kg m}^2/\text{s}^2 \tag{8.2}$$

$$E_{1.4M_\odot} = 2.52 \times 10^{47} (1000 \text{ g})(100 \text{ cm})^2/\text{s}^2 = 2.52 \times 10^{54} \text{ erg} \tag{8.3}$$

Assuming a mass of $1.4 M_\odot$ for both magnetars, the GW energy as a fraction of the energy in the star's mass ($E_{\text{GW}}/E_{1.4M_\odot}$) is 6.1×10^{-9} for the best upper limit of SGR 1806-20 (1.55×10^{46} erg) and 4.0×10^{-9} for the best upper limit of the search (1.01×10^{46} erg).

E_{GW} can also be compared to the magnetic field energy ($E_{\mathbf{B}}$). The energy in the magnetic field of magnetars is estimated to be on order of 10^{47} erg if the magnetic field is on order of 10^{15} gauss. This estimate comes from treating the interior magnetic field as a constant 10^{15} gauss field and integrating the calculated magnetic field energy density by the volume of the star, approximated with radius $R \approx 10$ km. The energy fraction $E_{\text{GW}}/E_{\mathbf{B}} = 0.101$ for the best upper limit of the search and $E_{\text{GW}}/E_{\mathbf{B}} = 0.155$ for the best upper limit of SGR 1806-20. This magnetic energy value could be thought of as a lower limit as it is thought that the internal magnetic field may be stronger than the external field [10]. For an internal field of order 10^{16} gauss (thought to be a plausible value [10]), E_{EM} would be on order of 10^{49} erg, providing a much larger energy reservoir to power GW emission.

E_{GW} can also be compared to the estimated magnetar burst energies from electromagnetic observations when available¹. Electromagnetic energy estimates were available for SGR burst 2471 and 2475, but we could not find estimates for SGR burst 2469 so we have marked it as unknown where referenced. SGR trigger 2471 had an estimated fluence of $7.88(\pm 0.39) \times 10^{-7}$ erg/cm² in the 8–1000 keV band (later estimated in a separate paper to be $8.44(\pm 0.546) \times 10^{-8}$ erg/cm² in the 8–200 keV band) and lasted ~ 100 ms [97, 98]. Assuming isotropic emission and using the estimated distance to SGR 1806-20 of 8.7 kpc, the larger fluence estimate corresponds to a burst energy of approximately 7.14×10^{39} erg. Comparing to the best E_{GW} upper limit for SGR trigger 2471 and ignoring the uncertainties, the ratio of the GW energy upper limit to the electromagnetic burst energy for this event is $E_{\text{GW}}/E_{\text{EM}} = 4.9 \times 10^6$.

¹The magnetar burst library at <http://staff.fnwi.uva.nl/a.l.watts/magnetar/mb.html> was used to find the paper containing the estimated burst electromagnetic energy for SGR burst 2475 [96].

SGR trigger 2475 was the first detected burst from 1E 1841-045, with duration of 32 ms and an estimated energy in the 15–100 keV band of $7.2_{-0.6}^{+0.4} \times 10^{36}$ erg [99]. Calculating the ratio of the GW energy upper limit to the electromagnetic burst energy for this event and ignoring the uncertainties gives $E_{\text{GW}}/E_{\text{EM}} = 1.4 \times 10^9$. Table 8.1 summarizes the best upper limit for each trigger and their comparisons to these different astrophysical parameters.

SGR Trigger	2469	2471	2475
Source Magnetar	SGR 1806-20	SGR 1806-20	1E 1841-045
E_{GW} Upper Limit (erg)	1.55×10^{46}	3.52×10^{46}	1.01×10^{46}
$E_{\text{GW}}/E_{1.4M_{\odot}}$	6.1×10^{-9}	1.4×10^{-8}	4.0×10^{-9}
$E_{\text{GW}}/E_{\vec{B} \approx 10^{15} \text{ gauss}}$	0.155	0.352	0.101
Observed E_{EM} (erg)	Unknown	7.14×10^{39}	$7.2_{-0.6}^{+0.4} \times 10^{36}$
$E_{\text{GW}}/\text{Observed } E_{\text{EM}}$	Unknown	4.9×10^6	1.4×10^9

TABLE 8.1. Summary of best upper limits and comparisons to possible energy sources. $E_{\vec{B} \approx 10^{15} \text{ gauss}}$ is approximated as 10^{47} erg.

These upper limits can also be compared to energy budgets for models of possible mechanisms behind bursts and giant flares. Ioka proposed a hydrodynamic deformation model where the magnetic field holds the star in a prolate shape and jumps between magnetic field configurations cause the shape of the star to become less prolate and release large amounts of energy as the star’s shape changes [75]. Corsi and Owen further expanded on this model showing it could apply for additional neutron star equations of state [10]. Both found that energies up to 10^{49} erg could be generated by changes in the magnetic field causing deformations in the shape of the star.

Corsi and Owen also discussed crust cracking, the mechanism thought to cause giant flares and some magnetar bursts [10]. They found crust cracking of normal neutron star crusts may provide up to 10^{46} erg. Furthermore, they discussed the energy

available from crust cracking if the star, or even just its core, was made up of quark matter. In such a case, they expect phases of quark-baryon or quark-meson matter to provide up to 10^{48} erg, and solid quark phases could provide up to $10^{49} - 10^{50}$ erg. LIGO can already probe below the upper limits of some of these energy budgets. If any of these mechanisms are responsible for magnetar bursts or giant flares, these energy limits could provide sufficient energy for detectable GW emission.

This search can be run for any magnetar bursts and giant flares that occur while aLIGO, an upgraded version of LIGO, is running. aLIGO is currently active and taking data, and once it reaches design sensitivity, it is expected to be 10 times as sensitive as initial LIGO. This would lead to energy limits 100 times lower than those set by LIGO. The upper limits of this search can be used to estimate the upper limits that may be reached with aLIGO. If this search had been run while aLIGO was at design sensitivity, the best upper limit of $E_{\text{GW}} = 1.01 \times 10^{46}$ erg could have been $E_{\text{GW}} = 1.01 \times 10^{44}$ erg. Additionally, there are multiple magnetars on order of 2 kpc away, and one as close as 1.6 kpc [65]. For a burst from a magnetar 1.6 kpc away occurring during aLIGO, the energy upper limit would have been roughly 3.59×10^{42} erg, the same order of magnitude as some stronger bursts.

This possible upper limit can be compared with the electromagnetic energy radiated during giant flares. If a giant flare with order $E_{\text{EM}} \approx 10^{44}$ erg energy occurred, the ratio of emitted electromagnetic energy to GW energy for this imagined upper limit would be $E_{\text{GW}}/E_{\text{EM}} \approx 3.59 \times 10^{-2}$. For an event such as the 2004 giant flare, this ratio would be approximately $E_{\text{GW}}/E_{\text{EM}} \approx 1.8 \times 10^{-4}$. With these energy ratios, GW with high $E_{\text{GW}}/E_{\text{EM}}$ would either be detected or ruled out. These possible aLIGO upper limits are summarized in Table 8.2.

Source Magnetar	1E 1841-045
E_{GW} Upper Limit	1.01×10^{46} erg
Estimated E_{GW} for aLIGO	1.01×10^{44} erg
$E_{\text{GW,aLIGO}}$ for 1.6 kpc	3.59×10^{42} erg
$E_{\text{GW,aLIGO,1.6kpc}}/E_{\text{EM}}$ (10^{44} erg)	3.59×10^{-2}
$E_{\text{GW,aLIGO,1.6kpc}}/E_{\text{EM}}$ (2×10^{46} erg)	1.8×10^{-4}

TABLE 8.2. Summary of best upper limit and equivalent aLIGO upper limit. Includes comparisons to electromagnetic energy levels of giant flares.

These estimates suggest running this search on data from aLIGO could probe significantly below the energy budgets discussed above. This could lead to either the detection of GWs related to magnetar bursts or the setting of stricter limits on the total amount of energy released during a magnetar burst or giant flare. These results could increase knowledge of the astrophysics of magnetars by placing constraints on the energy released through mechanisms such as crust cracking and hydrodynamic deformation, and may help constrain the possible equations of state of magnetars.

APPENDIX A

CONVENTIONS AND EQUATIONS

A.1. Conventions

Derivative: $\frac{d}{dx^\alpha}$ or D_α

Partial derivative: $\frac{\partial}{\partial x^\alpha}$ or ∂_α

Covariant derivative: ∇_α

D'Alembert operator: $\square = \partial^\mu \partial_\mu = \left(-\frac{\partial^2}{\partial t^2} + \nabla^2\right)$

Laplace operator: $\Delta = \nabla^2 = \partial^a \partial_a$

$$\text{Minkowski metric: } \eta_{\alpha\beta} = \begin{bmatrix} -1 & 0 & 0 & 0 \\ 0 & 1 & 0 & 0 \\ 0 & 0 & 1 & 0 \\ 0 & 0 & 0 & 1 \end{bmatrix}$$

A.2. Definitions

Covariant derivative:

$$\nabla_\beta V^\alpha = \frac{\partial V^\alpha}{\partial x^\beta} + V^\mu \Gamma_{\mu\beta}^\alpha$$

Christoffel symbol:

$$\Gamma_{\alpha\beta}^\mu = \frac{1}{2} g^{\mu\nu} (\partial_\beta g_{\nu\alpha} + \partial_\alpha g_{\nu\beta} - \partial_\nu g_{\alpha\beta})$$

Einstein Tensor (trace-reversed Ricci tensor):

$$G^{\alpha\beta} = G^{\beta\alpha} = R^{\alpha\beta} - \frac{1}{2} g^{\alpha\beta} R$$

Riemann curvature tensor:

$$R^\alpha{}_{\beta\mu\nu} = \partial_\mu \Gamma^\alpha{}_{\beta\nu} - \partial_\nu \Gamma^\alpha{}_{\beta\mu} + \Gamma^\alpha{}_{\sigma\mu} \Gamma^\sigma{}_{\beta\nu} - \Gamma^\alpha{}_{\sigma\nu} \Gamma^\sigma{}_{\beta\mu}$$

Ricci tensor:

$$R_{\alpha\beta} = R^\mu{}_{\alpha\mu\beta} = R_{\beta\alpha}$$

Ricci scalar:

$$R = g^{\mu\nu} R_{\mu\nu} = g^{\mu\nu} g^{\alpha\beta} R_{\alpha\mu\beta\nu}$$

A.3. Identities

$$\nabla_\beta G^{\alpha\beta} = 0$$

$$R_{\alpha\beta\mu\nu} = g_{\alpha\lambda} R^\lambda{}_{\beta\mu\nu} = \frac{1}{2} (\partial_\beta \partial_\mu g_{\alpha\nu} - \partial_\beta \partial_\nu g_{\alpha\mu} + \partial_\alpha \partial_\nu g_{\beta\mu} - \partial_\alpha \partial_\mu g_{\beta\nu})$$

$$R_{\alpha\beta\mu\nu} = -R_{\beta\alpha\mu\nu} = -R_{\alpha\beta\nu\mu} = R_{\mu\nu\alpha\beta}$$

$$R_{\alpha\beta\mu\nu} = -R_{\beta\alpha\mu\nu} = -R_{\alpha\beta\nu\mu} = R_{\mu\nu\alpha\beta}$$

A.4. Linearized Tensors

Christoffel symbol to first order in $h^{\mu\nu}$:

$$\Gamma^\mu{}_{\alpha\beta} = \frac{1}{2} g^{\mu\nu} (\partial_\beta g_{\nu\alpha} + \partial_\alpha g_{\nu\beta} - \partial_\nu g_{\alpha\beta})$$

$$\Gamma^\mu_{\alpha\beta} = \frac{1}{2}(\eta^{\mu\nu} + h^{\mu\nu})(\partial_\beta(\eta_{\nu\alpha} + h_{\nu\alpha}) + \partial_\alpha(\eta_{\nu\beta} + h_{\nu\beta}) - \partial_\nu(\eta_{\alpha\beta} + h_{\alpha\beta}))$$

$$\Gamma^\mu_{\alpha\beta} = \frac{1}{2}(\eta^{\mu\nu} + h^{\mu\nu})(0 + \partial_\beta h_{\nu\alpha} + 0 + \partial_\alpha h_{\nu\beta} - 0 - \partial_\nu h_{\alpha\beta})$$

To linear order in $h_{\mu\nu}$:

$$\Gamma^\mu_{\alpha\beta} = \frac{1}{2}\eta^{\mu\nu}(\partial_\beta h_{\nu\alpha} + \partial_\alpha h_{\nu\beta} - \partial_\nu h_{\alpha\beta})$$

Derivative of Christoffel symbol to linear order:

$$\partial_\gamma \Gamma^\mu_{\alpha\beta} = \partial_\gamma \left(\frac{1}{2}\eta^{\mu\nu}(\partial_\beta h_{\nu\alpha} + \partial_\alpha h_{\nu\beta} - \partial_\nu h_{\alpha\beta}) \right)$$

$$\partial_\gamma \Gamma^\mu_{\alpha\beta} = \frac{1}{2}\partial_\gamma \eta^{\mu\nu}(\partial_\beta h_{\nu\alpha} + \partial_\alpha h_{\nu\beta} - \partial_\nu h_{\alpha\beta}) + \frac{1}{2}\eta^{\mu\nu}\partial_\gamma(\partial_\beta h_{\nu\alpha} + \partial_\alpha h_{\nu\beta} - \partial_\nu h_{\alpha\beta})$$

$$\partial_\gamma \Gamma^\mu_{\alpha\beta} = 0 + \frac{1}{2}\eta^{\mu\nu}\partial_\gamma(\partial_\beta h_{\nu\alpha} + \partial_\alpha h_{\nu\beta} - \partial_\nu h_{\alpha\beta})$$

$$\partial_\gamma \Gamma^\mu_{\alpha\beta} = \frac{1}{2}\eta^{\mu\nu}(\partial_\gamma \partial_\beta h_{\nu\alpha} + \partial_\gamma \partial_\alpha h_{\nu\beta} - \partial_\gamma \partial_\nu h_{\alpha\beta})$$

Riemann tensor to first order in $h_{\mu\nu}$:

$$R^\alpha_{\beta\mu\nu} = \partial_\mu \Gamma^\alpha_{\beta\nu} - \partial_\nu \Gamma^\alpha_{\beta\mu} + \Gamma^\alpha_{\sigma\mu} \Gamma^\sigma_{\beta\nu} - \Gamma^\alpha_{\sigma\nu} \Gamma^\sigma_{\beta\mu}$$

Because the Christoffel symbol is linear in $h_{\mu\nu}$, we can drop terms that are higher than linear in the Christoffel symbol:

$$R^\alpha_{\beta\mu\nu} = \partial_\mu \Gamma^\alpha_{\beta\nu} - \partial_\nu \Gamma^\alpha_{\beta\mu}$$

$$R^\alpha_{\beta\mu\nu} = \frac{1}{2}\eta^{\alpha\gamma}(\partial_\mu \partial_\nu h_{\gamma\beta} + \partial_\mu \partial_\beta h_{\gamma\nu} - \partial_\mu \partial_\gamma h_{\beta\nu}) - \frac{1}{2}\eta^{\alpha\gamma}(\partial_\nu \partial_\mu h_{\gamma\beta} + \partial_\nu \partial_\beta h_{\gamma\mu} - \partial_\nu \partial_\gamma h_{\beta\mu})$$

$$R^\alpha{}_{\beta\mu\nu} = \frac{1}{2}\eta^{\alpha\gamma} (\partial_\mu\partial_\nu h_{\gamma\beta} + \partial_\mu\partial_\beta h_{\gamma\nu} - \partial_\mu\partial_\gamma h_{\beta\nu} - \partial_\nu\partial_\mu h_{\gamma\beta} - \partial_\nu\partial_\beta h_{\gamma\mu} + \partial_\nu\partial_\gamma h_{\beta\mu})$$

Riemann tensor to linear order in $h_{\mu\nu}$:

$$R^\alpha{}_{\beta\mu\nu} = \frac{1}{2}\eta^{\alpha\gamma} (\partial_\mu\partial_\beta h_{\gamma\nu} + \partial_\nu\partial_\gamma h_{\beta\mu} - \partial_\mu\partial_\gamma h_{\beta\nu} - \partial_\nu\partial_\beta h_{\gamma\mu})$$

And:

$$R_{\alpha\beta\mu\nu} = \frac{1}{2} (\partial_\mu\partial_\beta h_{\alpha\nu} + \partial_\nu\partial_\alpha h_{\beta\mu} - \partial_\mu\partial_\alpha h_{\beta\nu} - \partial_\nu\partial_\beta h_{\alpha\mu}) \quad (\text{A.1})$$

Ricci tensor to first order in $h_{\mu\nu}$:

$$R_{\beta\nu} = R^\mu{}_{\beta\mu\nu} = \frac{1}{2}\eta^{\mu\gamma} (\partial_\mu\partial_\beta h_{\gamma\nu} + \partial_\nu\partial_\gamma h_{\beta\mu} - \partial_\mu\partial_\gamma h_{\beta\nu} - \partial_\nu\partial_\beta h_{\gamma\mu})$$

$$R_{\beta\nu} = \frac{1}{2} (\partial^\gamma\partial_\beta h_{\gamma\nu} + \partial_\nu\partial^\gamma h_{\beta\gamma} - \partial^\gamma\partial_\gamma h_{\beta\nu} - \partial_\nu\partial_\beta h_{\gamma}{}^\gamma)$$

Ricci scalar to first order in $h_{\mu\nu}$:

$$R = g^{\mu\nu} R_{\mu\nu} = (\eta^{\mu\nu} + h^{\mu\nu}) R_{\mu\nu} \approx \eta^{\mu\nu} R_{\mu\nu}$$

$$R = \eta^{\beta\nu} \frac{1}{2} (\partial^\gamma\partial_\beta h_{\gamma\nu} + \partial_\nu\partial^\gamma h_{\beta\gamma} - \partial^\gamma\partial_\gamma h_{\beta\nu} - \partial_\nu\partial_\beta h_{\gamma}{}^\gamma)$$

$$R = \frac{1}{2} (\partial^\gamma\partial^\nu h_{\gamma\nu} + \partial^\beta\partial^\gamma h_{\beta\gamma} - \partial^\gamma\partial_\gamma h_{\beta}{}^\beta - \partial^\beta\partial_\beta h_{\gamma}{}^\gamma)$$

$$R = \partial^\gamma\partial^\nu h_{\gamma\nu} - \partial^\gamma\partial_\gamma h_{\nu}{}^\nu$$

Einstein Tensor (trace-reversed Ricci tensor) to first order:

$$G^{\alpha\mu} = G^{\mu\alpha} = R^{\alpha\mu} - \frac{1}{2}g^{\alpha\mu} R = \eta^{\alpha\beta}\eta^{\mu\nu} R_{\beta\nu} - \frac{1}{2}g^{\alpha\mu} R \approx \eta^{\alpha\beta}\eta^{\mu\nu} R_{\beta\nu} - \frac{1}{2}\eta^{\alpha\mu} R$$

$$G^{\alpha\mu} = \eta^{\alpha\beta}\eta^{\mu\nu}\frac{1}{2}(\partial^\gamma\partial_\beta h_{\gamma\nu} + \partial_\nu\partial^\gamma h_{\beta\gamma} - \partial^\gamma\partial_\gamma h_{\beta\nu} - \partial_\nu\partial_\beta h_{\gamma^\gamma}) \\ - \frac{1}{2}\eta^{\alpha\mu}(\partial^\gamma\partial^\nu h_{\gamma\nu} - \partial^\gamma\partial_\gamma h_{\nu^\nu})$$

$$G_{\beta\nu} = \frac{1}{2}(\partial^\gamma\partial_\beta h_{\gamma\nu} + \partial_\nu\partial^\gamma h_{\beta\gamma} - \partial^\gamma\partial_\gamma h_{\beta\nu} - \partial_\nu\partial_\beta h_{\gamma^\gamma}) - \frac{1}{2}\eta_{\beta\nu}(\partial^\gamma\partial^\mu h_{\gamma\mu} - \partial^\gamma\partial_\gamma h_{\mu^\mu})$$

Let the trace of $h_{\mu\nu}$ be denoted such that $h = h^\alpha{}_\alpha$. Using the “trace reverse” of $h_{\mu\nu}$:

$$\bar{h}_{\mu\nu} = h_{\mu\nu} - \frac{1}{2}\eta_{\mu\nu}h^\alpha{}_\alpha = h_{\mu\nu} - \frac{1}{2}\eta_{\mu\nu}h$$

$$G_{\beta\nu} = \frac{1}{2}\left(\partial^\gamma\partial_\beta\bar{h}_{\gamma\nu} + \frac{1}{2}\partial^\gamma\partial_\beta\eta_{\gamma\nu}h + \partial_\nu\partial^\gamma\bar{h}_{\beta\gamma} + \frac{1}{2}\partial_\nu\partial^\gamma\eta_{\beta\gamma}h - \partial^\gamma\partial_\gamma\bar{h}_{\beta\nu} - \frac{1}{2}\partial^\gamma\partial_\gamma\eta_{\beta\nu}h \right. \\ \left. - \partial_\nu\partial_\beta h\right) - \frac{1}{2}\eta_{\beta\nu}\left(\partial^\gamma\partial^\mu\bar{h}_{\gamma\mu} + \frac{1}{2}\partial^\gamma\partial^\mu\eta_{\gamma\mu}h - \partial^\gamma\partial_\gamma h\right)$$

$$2G_{\beta\nu} = \partial^\gamma\partial_\beta\bar{h}_{\gamma\nu} + \frac{1}{2}\partial^\gamma\partial_\beta\eta_{\gamma\nu}h + \partial_\nu\partial^\gamma\bar{h}_{\beta\gamma} + \frac{1}{2}\partial_\nu\partial^\gamma\eta_{\beta\gamma}h - \partial^\gamma\partial_\gamma\bar{h}_{\beta\nu} - \frac{1}{2}\partial^\gamma\partial_\gamma\eta_{\beta\nu}h \\ - \partial_\nu\partial_\beta h - \eta_{\beta\nu}\partial^\gamma\partial^\mu\bar{h}_{\gamma\mu} - \frac{1}{2}\eta_{\beta\nu}\partial^\gamma\partial^\mu\eta_{\gamma\mu}h + \eta_{\beta\nu}\partial^\gamma\partial_\gamma h$$

$$2G_{\beta\nu} = \partial^\gamma\partial_\beta\bar{h}_{\gamma\nu} + \frac{1}{2}\partial_\nu\partial_\beta h + \partial_\nu\partial^\gamma\bar{h}_{\beta\gamma} + \frac{1}{2}\partial_\nu\partial_\beta h - \partial^\gamma\partial_\gamma\bar{h}_{\beta\nu} - \frac{1}{2}\partial^\gamma\partial_\gamma\eta_{\beta\nu}h - \partial_\nu\partial_\beta h \\ - \eta_{\beta\nu}\partial^\gamma\partial^\mu\bar{h}_{\gamma\mu} - \frac{1}{2}\eta_{\beta\nu}\partial^\gamma\partial_\gamma h + \eta_{\beta\nu}\partial^\gamma\partial_\gamma h$$

$$2G_{\beta\nu} = \partial^\gamma\partial_\beta\bar{h}_{\gamma\nu} + \frac{1}{2}\partial_\nu\partial_\beta h + \partial_\nu\partial^\gamma\bar{h}_{\beta\gamma} + \frac{1}{2}\partial_\nu\partial_\beta h - \square\bar{h}_{\beta\nu} - \frac{1}{2}\square\eta_{\beta\nu}h - \partial_\nu\partial_\beta h \\ - \eta_{\beta\nu}\partial^\gamma\partial^\mu\bar{h}_{\gamma\mu} - \frac{1}{2}\eta_{\beta\nu}\square h + \eta_{\beta\nu}\square h$$

$$2G_{\beta\nu} = \partial^\gamma\partial_\beta\bar{h}_{\gamma\nu} + \frac{1}{2}\partial_\nu\partial_\beta h + \partial_\nu\partial^\gamma\bar{h}_{\beta\gamma} + \frac{1}{2}\partial_\nu\partial_\beta h - \square\bar{h}_{\beta\nu} - \partial_\nu\partial_\beta h - \eta_{\beta\nu}\partial^\gamma\partial^\mu\bar{h}_{\gamma\mu}$$

$$\begin{aligned}
2G_{\beta\nu} &= \partial^\gamma \partial_\beta \bar{h}_{\gamma\nu} + \partial_\nu \partial^\gamma \bar{h}_{\beta\gamma} - \square \bar{h}_{\beta\nu} - \eta_{\beta\nu} \partial^\gamma \partial^\mu \bar{h}_{\gamma\mu} \\
G_{\beta\nu} &= -\frac{1}{2} (\square \bar{h}_{\beta\nu} - \partial^\gamma \partial_\beta \bar{h}_{\gamma\nu} - \partial_\nu \partial^\gamma \bar{h}_{\beta\gamma} + \eta_{\beta\nu} \partial^\gamma \partial^\mu \bar{h}_{\gamma\mu})
\end{aligned} \tag{A.2}$$

It can be shown that a gauge can always be chosen such that:

$$\partial_\nu \bar{h}^{\mu\nu} = 0 \tag{A.3}$$

Plugging this into A.2 gives an Einstein Tensor linear in $h_{\mu\nu}$ of:

$$G_{\beta\nu} = -\frac{1}{2} \square \bar{h}_{\beta\nu} \tag{A.4}$$

Plugging A.4 into 2.14 gives the linear form of the Einstein equations (the so called weak-field Einstein equations):

$$\square \bar{h}^{\beta\nu} = -16\pi T^{\beta\nu} \tag{A.5}$$

APPENDIX B

DERIVATION OF UPPER LIMITS

This appendix details the derivation of the GW energy (E_{GW}) and h_{rss} of the waveform type used for injections in this research. E_{GW} and h_{rss} are calculated for a sine-Gaussian and the results are then used to calculate E_{GW} and h_{rss} for a half sine-Gaussian.

The equations in Section 2.4 can be generalized to include the inclination angle ι and the polarization angle ψ :

$$h_+ = \frac{h_0}{\sqrt{2}} \left(\frac{(1 + \cos^2 \iota)}{2} \cos(2\pi f_0 t + \phi) \cos 2\psi + (\cos \iota) \sin(2\pi f_0 t + \phi) \sin 2\psi \right) \quad (\text{B.1})$$

$$h_\times = \frac{h_0}{\sqrt{2}} \left(-\frac{(1 + \cos^2 \iota)}{2} \cos(2\pi f_0 t + \phi) \sin 2\psi + (\cos \iota) \sin(2\pi f_0 t + \phi) \cos 2\psi \right) \quad (\text{B.2})$$

To simplify calculations, let $\phi = 0$, giving:

$$h_+ = \frac{h_0}{\sqrt{2}} \left(\frac{(1 + \cos^2 \iota)}{2} \cos(2\pi f_0 t) \cos 2\psi + (\cos \iota) \sin(2\pi f_0 t) \sin 2\psi \right) \quad (\text{B.3})$$

$$h_\times = \frac{h_0}{\sqrt{2}} \left(-\frac{(1 + \cos^2 \iota)}{2} \cos(2\pi f_0 t) \sin 2\psi + (\cos \iota) \sin(2\pi f_0 t) \cos 2\psi \right) \quad (\text{B.4})$$

The factors dependent on ψ are often absorbed into the antenna factors. This can be thought of as working with the GWs in an intermediate reference frame. When this is done, it is convention in most literature to choose the frame such that $\psi = 0$. This gives the following:

$$h_+ = h_{+, \psi=0} = \frac{h_0}{\sqrt{2}} \frac{(1 + \cos^2 \iota)}{2} \cos(2\pi f_0 t) \quad (\text{B.5})$$

$$h_{\times} = h_{\times, \psi=0} = \frac{h_0}{\sqrt{2}} (\cos \iota) \sin(2\pi f_0 t) \quad (\text{B.6})$$

It is important to note that any intermediate frame could have been chosen.

If the waveform is a sine-Gaussian such as (7.1), (B.3) and (B.4) are multiplied by the Gaussian envelope $e^{-(t-t_0)^2/\tau^2}$ (with $t_0 = 0$ making the envelope e^{-t^2/τ^2}) and become:

$$h_+ = \frac{h_0}{\sqrt{2}} e^{-t^2/\tau^2} \left(\frac{(1 + \cos^2 \iota)}{2} \cos(2\pi f_0 t) \cos 2\psi + (\cos \iota) \sin(2\pi f_0 t) \sin 2\psi \right) \quad (\text{B.7})$$

$$h_{\times} = \frac{h_0}{\sqrt{2}} e^{-t^2/\tau^2} \left(-\frac{(1 + \cos^2 \iota)}{2} \cos(2\pi f_0 t) \sin 2\psi + (\cos \iota) \sin(2\pi f_0 t) \cos 2\psi \right) \quad (\text{B.8})$$

B.1. Calculating h_{rss}

(B.7) and (B.8) (and using $h_{+, \psi=0}$ and $h_{\times, \psi=0}$ for brevity) are plugged into (7.8):

$$\begin{aligned} h_{\text{rss}} &= \\ & \left(\int_{-\infty}^{\infty} \left[\left| \frac{h_0}{\sqrt{2}} e^{-t^2/\tau^2} \left(\frac{(1 + \cos^2 \iota)}{2} \cos(2\pi f_0 t) \cos 2\psi + (\cos \iota) \sin(2\pi f_0 t) \sin 2\psi \right) \right|^2 \right. \right. \\ & \left. \left. + \left| \frac{h_0}{\sqrt{2}} e^{-t^2/\tau^2} \left(-\frac{(1 + \cos^2 \iota)}{2} \cos(2\pi f_0 t) \sin 2\psi + (\cos \iota) \sin(2\pi f_0 t) \cos 2\psi \right) \right|^2 \right] dt \right)^{1/2} \\ &= \sqrt{\int_{-\infty}^{\infty} (|h_{+, \psi=0} \cos 2\psi + h_{\times, \psi=0} \sin 2\psi|^2 + |-h_{+, \psi=0} \sin 2\psi + h_{\times, \psi=0} \cos 2\psi|^2) dt} \end{aligned} \quad (\text{B.9})$$

$$h_{\text{rss}} = \left(\int_{-\infty}^{\infty} (h_{+, \psi=0}^2 \cos^2 2\psi + 2h_{+, \psi=0}h_{\times, \psi=0} \cos 2\psi \sin 2\psi + h_{\times, \psi=0}^2 \sin^2 2\psi + h_{+, \psi=0}^2 \sin^2 2\psi - 2h_{+, \psi=0}h_{\times, \psi=0} \sin 2\psi \cos 2\psi + h_{\times, \psi=0}^2 \cos^2 2\psi) dt \right)^{1/2} \quad (\text{B.10})$$

$$h_{\text{rss}} = \sqrt{\int_{-\infty}^{\infty} (h_{+, \psi=0}^2 \cos^2 2\psi + h_{\times, \psi=0}^2 \sin^2 2\psi + h_{+, \psi=0}^2 \sin^2 2\psi + h_{\times, \psi=0}^2 \cos^2 2\psi) dt} \quad (\text{B.11})$$

$$h_{\text{rss}} = \sqrt{\int_{-\infty}^{\infty} (h_{+, \psi=0}^2 (\sin^2 2\psi + \cos^2 2\psi) + h_{\times, \psi=0}^2 (\sin^2 2\psi + \cos^2 2\psi)) dt} \quad (\text{B.12})$$

$$h_{\text{rss}} = \sqrt{\int_{-\infty}^{\infty} (h_{+, \psi=0}^2 + h_{\times, \psi=0}^2) dt} \quad (\text{B.13})$$

$$h_{\text{rss}} = \frac{h_0}{\sqrt{2}} \sqrt{\int_{-\infty}^{\infty} e^{-2t^2/\tau^2} \left(\frac{(1 + \cos^2 \iota)^2}{4} \cos^2 (2\pi f_0 t) + (\cos^2 \iota) \sin^2 (2\pi f_0 t) \right) dt} \quad (\text{B.14})$$

Using the following half angle formulas:

$$\sin^2 x = \frac{1 - \cos 2x}{2} \quad (\text{B.15})$$

$$\cos^2 x = \frac{1 + \cos 2x}{2} \quad (\text{B.16})$$

(B.17) can be rewritten as:

$$h_{\text{rss}} = \frac{h_0}{\sqrt{2}} \sqrt{\int_{-\infty}^{\infty} e^{-2t^2/\tau^2} \left(\frac{(1 + \cos^2 \iota)^2}{4} \frac{1 + \cos (4\pi f_0 t)}{2} + \cos^2 \iota \frac{1 - \cos (4\pi f_0 t)}{2} \right) dt} \quad (\text{B.17})$$

$$h_{\text{rss}} = \frac{h_0}{2} \sqrt{\int_{-\infty}^{\infty} e^{-2t^2/\tau^2} \left(\frac{(1 + \cos^2 \iota)^2}{4} (1 + \cos (4\pi f_0 t)) + \cos^2 \iota (1 - \cos (4\pi f_0 t)) \right) dt} \quad (\text{B.18})$$

$$h_{\text{rss}} = \frac{h_0}{2} \sqrt{\int_{-\infty}^{\infty} e^{-2t^2/\tau^2} \left(\frac{(1 + \cos^2 \iota)^2}{4} + \cos^2 \iota + \left(\frac{(1 + \cos^2 \iota)^2}{4} - \cos^2 \iota \right) \cos(4\pi f_0 t) \right) dt} \quad (\text{B.19})$$

$$h_{\text{rss}} = \frac{h_0}{2} \left(\left(\frac{(1 + \cos^2 \iota)^2}{4} + \cos^2 \iota \right) \int_{-\infty}^{\infty} e^{-2t^2/\tau^2} dt + \left(\frac{(1 + \cos^2 \iota)^2}{4} - \cos^2 \iota \right) \int_{-\infty}^{\infty} e^{-2t^2/\tau^2} \cos(4\pi f_0 t) dt \right)^{1/2} \quad (\text{B.20})$$

Following [100], the following formulas can be found in [101] (formulas 3.321.3 and 3.896.4):

$$\int_0^{\infty} e^{-q^2 x^2} dx = \frac{\sqrt{\pi}}{2q} \quad (\text{B.21})$$

$$\int_0^{\infty} e^{-\beta x^2} \cos(bx) dx = \frac{1}{2} \sqrt{\pi/\beta} e^{-b^2/4\beta} \quad (\text{B.22})$$

(B.20) can be rewritten using the fact it has even integrals and then (B.21) and (B.22) can be used to solve the resulting equation:

$$h_{\text{rss}} = \frac{h_0}{2} \left(\left(\frac{(1 + \cos^2 \iota)^2}{4} + \cos^2 \iota \right) 2 \int_0^{\infty} e^{-2t^2/\tau^2} dt + \left(\frac{(1 + \cos^2 \iota)^2}{4} - \cos^2 \iota \right) 2 \int_0^{\infty} e^{-2t^2/\tau^2} \cos(4\pi f_0 t) dt \right)^{1/2} \quad (\text{B.23})$$

$$h_{\text{rss}} = \frac{h_0}{\sqrt{2}} \left(\left(\frac{(1 + \cos^2 \iota)^2}{4} + \cos^2 \iota \right) \int_0^\infty e^{-2t^2/\tau^2} dt + \left(\frac{(1 + \cos^2 \iota)^2}{4} - \cos^2 \iota \right) \int_0^\infty e^{-2t^2/\tau^2} \cos(4\pi f_0 t) dt \right)^{1/2} \quad (\text{B.24})$$

$$\int_0^\infty e^{-2t^2/\tau^2} dt = \frac{\sqrt{\pi}}{2\sqrt{2/\tau^2}} = \frac{\tau\sqrt{\pi}}{2\sqrt{2}} \quad (\text{B.25})$$

$$\int_0^\infty e^{-2t^2/\tau^2} \cos(4\pi f_0 t) dt = \frac{1}{2} \sqrt{\pi/(2/\tau^2)} e^{-(4\pi f_0)^2/4(2/\tau^2)} = \frac{\tau\sqrt{\pi}}{2\sqrt{2}} e^{-2\pi^2 f_0^2 \tau^2} \quad (\text{B.26})$$

$$h_{\text{rss}} = \frac{h_0}{\sqrt{2}} \sqrt{\left(\frac{(1 + \cos^2 \iota)^2}{4} + \cos^2 \iota \right) \frac{\tau\sqrt{\pi}}{2\sqrt{2}} + \left(\frac{(1 + \cos^2 \iota)^2}{4} - \cos^2 \iota \right) \frac{\tau\sqrt{\pi}}{2\sqrt{2}} e^{-2\pi^2 f_0^2 \tau^2}} \quad (\text{B.27})$$

$$h_{\text{rss}} = \frac{h_0}{\sqrt{2}} \sqrt{\frac{\tau\sqrt{\pi}}{2\sqrt{2}} \left(\left(\frac{(1 + \cos^2 \iota)^2}{4} + \cos^2 \iota \right) + \left(\frac{(1 + \cos^2 \iota)^2}{4} - \cos^2 \iota \right) e^{-2\pi^2 f_0^2 \tau^2} \right)} \quad (\text{B.28})$$

Substituting in Q gives:

$$h_{\text{rss}} = \frac{h_0}{\sqrt{2}} \sqrt{\frac{Q}{4\sqrt{\pi}f_0} \left(\left(\frac{(1 + \cos^2 \iota)^2}{4} + \cos^2 \iota \right) + \left(\frac{(1 + \cos^2 \iota)^2}{4} - \cos^2 \iota \right) e^{-Q^2} \right)} \quad (\text{B.29})$$

$$h_{\text{rss}} = \frac{h_0}{2\sqrt{2}\pi^{1/4}} \sqrt{\frac{Q}{f_0} \left(\left(\frac{(1 + \cos^2 \iota)^2}{4} + \cos^2 \iota \right) + \left(\frac{(1 + \cos^2 \iota)^2}{4} - \cos^2 \iota \right) e^{-Q^2} \right)} \quad (\text{B.30})$$

For high Q, (B.30) can be approximated as:

$$h_{\text{rss}}^{\text{HQ}} \approx \frac{h_0}{2\sqrt{2}\pi^{1/4}} \sqrt{\frac{Q}{f_0} \left(\frac{(1 + \cos^2 \iota)^2}{4} + \cos^2 \iota \right)} \quad (\text{B.31})$$

The magnitude of (B.30) ranges from a maximum at $\iota = 0^\circ$ to a minimum at $\iota = 90^\circ$:

$$h_{\text{rss},\iota=0^\circ} = \frac{h_0}{2\pi^{1/4}} \sqrt{\frac{Q}{f_0}} \quad (\text{B.32})$$

$$h_{\text{rss},\iota=90^\circ} = \frac{h_0}{4\sqrt{2}\pi^{1/4}} \sqrt{\frac{Q}{f_0}} \sqrt{1 + e^{-Q^2}} \quad (\text{B.33})$$

For high Q , (B.32) and (B.33) become:

$$h_{\text{rss},\iota=0^\circ}^{\text{HQ}} = \frac{h_0}{2\pi^{1/4}} \sqrt{\frac{Q}{f_0}} \quad (\text{B.34})$$

$$h_{\text{rss},\iota=90^\circ}^{\text{HQ}} \approx \frac{h_0}{4\sqrt{2}\pi^{1/4}} \sqrt{\frac{Q}{f_0}} \quad (\text{B.35})$$

Note that $h_{\text{rss},\iota=0^\circ}^{\text{HQ}} = \sqrt{8} h_{\text{rss},\iota=90^\circ}^{\text{HQ}}$. In terms of the energy upper limits, this means that energy upper limits set for a linearly polarized waveform would be expected to be roughly 8 times higher than for a circularly polarized waveform (and the h_{rss} limits would be expected to be $\sqrt{8}$ times higher). It is also interesting to note that $h_{\text{rss},\iota=0^\circ} = h_{\text{rss},\iota=0^\circ}^{\text{HQ}}$; in the case of $\iota = 0$, the e^{-Q^2} term drops out completely giving an exact answer that is the same regardless of the high Q approximation.

Rewriting (B.36), (B.37) and (B.38) in terms of τ gives:

$$h_{\text{rss}}^{\text{HQ}} \approx h_0 \tau^{1/2} \frac{\pi^{1/4}}{2(2^{1/4})} \sqrt{\frac{(1 + \cos^2 \iota)^2}{4} + \cos^2 \iota} \quad (\text{B.36})$$

$$h_{\text{rss},\iota=0^\circ}^{\text{HQ}} = h_0 \tau^{1/2} \frac{(2\pi)^{1/4}}{2} \quad (\text{B.37})$$

$$h_{\text{rss},\iota=90^\circ}^{\text{HQ}} \approx h_0 \tau^{1/2} \frac{(2\pi)^{1/4}}{4\sqrt{2}} \quad (\text{B.38})$$

B.2. Calculating E_{GW}

The fluence is “the GW energy flowing through a unit area at the detector integrated over the emission time” [79]:

$$F = \frac{c^3}{16\pi G} \int \left(\dot{h}_+^2(t) + \dot{h}_\times^2(t) \right) dt \quad (\text{B.39})$$

To get the total energy emitted, integrate (B.39) over a sphere surrounding the source with a radius r (r is the distance to the source):

$$E_{\text{GW}} = \frac{c^3}{16\pi G} \int_A \int_{-\infty}^{\infty} \left(\dot{h}_+^2(t) + \dot{h}_\times^2(t) \right) dt dA \quad (\text{B.40})$$

$$E_{\text{GW}} = \frac{c^3}{16\pi G} \int_{-\infty}^{\infty} \int_0^{2\pi} \int_0^\pi \left(\dot{h}_+^2(t) + \dot{h}_\times^2(t) \right) r^2 \sin \theta d\theta d\phi dt \quad (\text{B.41})$$

In order to make the area integral simpler to calculate, the coordinate system can be chosen such that $\iota = \theta$:

$$E_{\text{GW}} = \frac{c^3}{16\pi G} \int_{-\infty}^{\infty} \int_0^{2\pi} \int_0^\pi \left(\dot{h}_+^2(t) + \dot{h}_\times^2(t) \right) r^2 \sin \iota d\iota d\phi dt \quad (\text{B.42})$$

From the derivation of (B.13) from (7.8), the following has been shown:

$$h_{\text{rss}}^2 = \int_{-\infty}^{\infty} \left(h_+^2 + h_\times^2 \right) dt = \int_{-\infty}^{\infty} \left(h_{+, \psi=0}^2 + h_{\times, \psi=0}^2 \right) dt \quad (\text{B.43})$$

ψ has no time dependence, so:

$$\int_{-\infty}^{\infty} \left(\dot{h}_+^2 + \dot{h}_\times^2 \right) dt = \int_{-\infty}^{\infty} \left(\dot{h}_{+, \psi=0}^2 + \dot{h}_{\times, \psi=0}^2 \right) dt \quad (\text{B.44})$$

Using (B.44), (B.42) can be rewritten as:

$$E_{\text{GW}} = \frac{c^3}{16\pi G} \int_{-\infty}^{\infty} \int_0^{2\pi} \int_0^{\pi} \left(\dot{h}_{+, \psi=0}^2(t) + \dot{h}_{\times, \psi=0}^2(t) \right) r^2 \sin \iota \, d\iota \, d\phi \, dt \quad (\text{B.45})$$

The components of the time integral of (B.45) are:

$$\int_{-\infty}^{\infty} \dot{h}_{+, \psi=0}^2(t) \, dt = \int_{-\infty}^{\infty} \left(\frac{d}{dt} \frac{h_0}{\sqrt{2}} e^{-t^2/\tau^2} \frac{(1 + \cos^2 \iota)}{2} \cos(2\pi f_0 t) \right)^2 dt \quad (\text{B.46})$$

$$\int_{-\infty}^{\infty} \dot{h}_{\times, \psi=0}^2(t) \, dt = \int_{-\infty}^{\infty} \left(\frac{d}{dt} \frac{h_0}{\sqrt{2}} e^{-t^2/\tau^2} (\cos \iota) \sin(2\pi f_0 t) \right)^2 dt \quad (\text{B.47})$$

Taking the derivatives gives:

$$\begin{aligned} \int_{-\infty}^{\infty} \dot{h}_{+, \psi=0}^2(t) \, dt = \\ \frac{h_0^2}{2} \frac{(1 + \cos^2 \iota)^2}{4} \int_{-\infty}^{\infty} e^{-2t^2/\tau^2} \left(-\frac{2t}{\tau^2} \cos(2\pi f_0 t) - 2\pi f_0 \sin(2\pi f_0 t) \right)^2 dt \quad (\text{B.48}) \end{aligned}$$

$$\begin{aligned} \int_{-\infty}^{\infty} \dot{h}_{\times, \psi=0}^2(t) \, dt = \\ \frac{h_0^2}{2} (\cos^2 \iota) \int_{-\infty}^{\infty} e^{-2t^2/\tau^2} \left(-\frac{2t}{\tau^2} \sin(2\pi f_0 t) + 2\pi f_0 \cos(2\pi f_0 t) \right)^2 dt \quad (\text{B.49}) \end{aligned}$$

First $\int_{-\infty}^{\infty} \dot{h}_{+, \psi=0}^2(t) \, dt$ will be calculated:

$$\frac{h_0^2}{2} \frac{(1 + \cos^2 \iota)^2}{4} \int_{-\infty}^{\infty} e^{-2t^2/\tau^2} \left(-\frac{2t}{\tau^2} \cos(2\pi f_0 t) - 2\pi f_0 \sin(2\pi f_0 t) \right)^2 dt \quad (\text{B.50})$$

$$\frac{h_0^2 (1 + \cos^2 \iota)^2}{2} \frac{1}{4} \int_{-\infty}^{\infty} e^{-2t^2/\tau^2} \left(\frac{4t^2}{\tau^4} \cos^2(2\pi f_0 t) + 2 \frac{2t}{\tau^2} \cos(2\pi f_0 t) 2\pi f_0 \sin(2\pi f_0 t) + 4\pi^2 f_0^2 \sin^2(2\pi f_0 t) \right) dt \quad (\text{B.51})$$

$$\frac{h_0^2 (1 + \cos^2 \iota)^2}{2} \frac{1}{4} \left[\int_{-\infty}^{\infty} e^{-2t^2/\tau^2} \frac{4t^2}{\tau^4} \cos^2(2\pi f_0 t) dt + \int_{-\infty}^{\infty} e^{-2t^2/\tau^2} \frac{4t}{\tau^2} \cos(2\pi f_0 t) 2\pi f_0 \sin(2\pi f_0 t) dt + \int_{-\infty}^{\infty} e^{-2t^2/\tau^2} 4\pi^2 f_0^2 \sin^2(2\pi f_0 t) dt \right] \quad (\text{B.52})$$

In addition to the half angle formulas (B.15) and (B.16), using the double angle formula:

$$\sin 2x = 2 \sin x \cos x \quad (\text{B.53})$$

(B.52) can be rewritten as:

$$\frac{h_0^2 (1 + \cos^2 \iota)^2}{2} \frac{1}{4} \left[\int_{-\infty}^{\infty} e^{-2t^2/\tau^2} \frac{4t^2}{\tau^4} \frac{1 + \cos(4\pi f_0 t)}{2} dt + \int_{-\infty}^{\infty} e^{-2t^2/\tau^2} \frac{4t}{\tau^2} \pi f_0 \sin(4\pi f_0 t) dt + \int_{-\infty}^{\infty} e^{-2t^2/\tau^2} 4\pi^2 f_0^2 \frac{1 - \cos(4\pi f_0 t)}{2} dt \right] \quad (\text{B.54})$$

Each of these integrals is even, so (B.54) can be rewritten as:

$$\frac{h_0^2 (1 + \cos^2 \iota)^2}{2} \frac{1}{4} \left[\int_0^{\infty} e^{-2t^2/\tau^2} \frac{4t^2}{\tau^4} (1 + \cos(4\pi f_0 t)) dt + \int_0^{\infty} e^{-2t^2/\tau^2} \frac{8t}{\tau^2} \pi f_0 \sin(4\pi f_0 t) dt + \int_0^{\infty} e^{-2t^2/\tau^2} 4\pi^2 f_0^2 (1 - \cos(4\pi f_0 t)) dt \right] \quad (\text{B.55})$$

Again following [100], the following formulas can be found in [101] (formulas 3.952.1, 3.461.2 and 3.952.4):

$$\int_0^{\infty} x e^{-p^2 x^2} \sin ax \, dx = \frac{a\sqrt{\pi}}{4p^3} e^{-a^2/(4p^2)} \quad (\text{B.56})$$

$$\int_0^{\infty} x^{2n} e^{-px^2} \, dx = \frac{(2n-1)!! \sqrt{\pi}}{2(2p)^n \sqrt{p}} \quad (\text{B.57})$$

$$\int_0^{\infty} x^2 e^{-p^2 x^2} \cos ax \, dx = \sqrt{\pi} \frac{2p^2 - a^2}{8p^5} e^{-a^2/(4p^2)} \quad (\text{B.58})$$

Using and (B.56), (B.57) and (B.58) in addition to (B.21) and (B.22) gives:

$$\begin{aligned} & \frac{h_0^2 (1 + \cos^2 \iota)^2}{2} \frac{4}{4} \\ & \times \left[\frac{4}{\tau^4} \left(\frac{(2(1)-1)!! \sqrt{\pi}}{2(2(2/\tau^2))^1 \sqrt{2/\tau^2}} + \sqrt{\pi} \frac{2 \left(\sqrt{2/\tau^2}\right)^2 - (4\pi f_0)^2}{8 \left(\sqrt{2/\tau^2}\right)^5} e^{-(4\pi f_0)^2 / \left(4 \left(\sqrt{2/\tau^2}\right)^2\right)} \right) \right. \\ & \quad + \frac{8}{\tau^2} \pi f_0 \frac{(4\pi f_0) \sqrt{\pi}}{4 \left(\sqrt{2/\tau^2}\right)^3} e^{-(4\pi f_0)^2 / \left(4 \left(\sqrt{2/\tau^2}\right)^2\right)} \\ & \quad \left. + 4\pi^2 f_0^2 \left(\frac{\sqrt{\pi}}{2\sqrt{2/\tau^2}} - \frac{1}{2} \sqrt{\pi/(2/\tau^2)} e^{-(4\pi f_0)^2 / 4(2/\tau^2)} \right) \right] \quad (\text{B.59}) \end{aligned}$$

$$\begin{aligned} & \frac{h_0^2 (1 + \cos^2 \iota)^2}{2} \frac{4}{4} \left[\frac{4}{\tau^4} \left(\frac{1}{8/\tau^2} \frac{\sqrt{\pi}}{\sqrt{2/\tau^2}} + \sqrt{\pi} \frac{4/\tau^2 - 16\pi^2 f_0^2}{8(2/\tau^2)^2 \sqrt{2/\tau^2}} e^{-16\pi^2 f_0^2 / 4(2/\tau^2)} \right) \right. \\ & \quad + \frac{8}{\tau^2} \pi f_0 \frac{(4\pi f_0) \sqrt{\pi}}{4(2/\tau^2) \sqrt{2/\tau^2}} e^{-16\pi^2 f_0^2 / 4(2/\tau^2)} \\ & \quad \left. + 4\pi^2 f_0^2 \left(\frac{\sqrt{\pi}}{2\sqrt{2/\tau^2}} - \frac{1}{2} \frac{\sqrt{\pi}}{\sqrt{2/\tau^2}} e^{-16\pi^2 f_0^2 / 4(2/\tau^2)} \right) \right] \quad (\text{B.60}) \end{aligned}$$

$$\begin{aligned} \frac{h_0^2 (1 + \cos^2 \iota)^2}{2} \frac{\sqrt{\pi}}{4} \frac{1}{\sqrt{2/\tau^2}} \left[\frac{4}{\tau^4} \left(\frac{1}{8/\tau^2} + \frac{4/\tau^2 - 16\pi^2 f_0^2}{8(2/\tau^2)^2} e^{-2\pi^2 f_0^2 \tau^2} \right) \right. \\ \left. + \frac{8}{\tau^2} \pi f_0 \frac{(4\pi f_0)}{4(2/\tau^2)} e^{-2\pi^2 f_0^2 \tau^2} \right. \\ \left. + 4\pi^2 f_0^2 \frac{1}{2} \left(1 - e^{-2\pi^2 f_0^2 \tau^2} \right) \right] \quad (\text{B.61}) \end{aligned}$$

$$\begin{aligned} \frac{h_0^2 (1 + \cos^2 \iota)^2}{2} \frac{\sqrt{\pi}}{4} \frac{1}{\sqrt{2}} \tau \left[\frac{4}{\tau^4} \left(\frac{\tau^2}{8} + \frac{\tau^2 - 4\pi^2 f_0^2 \tau^4}{8} e^{-2\pi^2 f_0^2 \tau^2} \right) \right. \\ \left. + 4\pi^2 f_0^2 e^{-2\pi^2 f_0^2 \tau^2} + 2\pi^2 f_0^2 \left(1 - e^{-2\pi^2 f_0^2 \tau^2} \right) \right] \quad (\text{B.62}) \end{aligned}$$

$$h_0^2 \tau \frac{\sqrt{\pi}}{2\sqrt{2}} \frac{(1 + \cos^2 \iota)^2}{4} \left[\frac{1}{\tau^2} \left(\frac{1}{2} + \frac{1 - 4\pi^2 f_0^2 \tau^2}{2} e^{-2\pi^2 f_0^2 \tau^2} \right) + 2\pi^2 f_0^2 \left(1 + e^{-2\pi^2 f_0^2 \tau^2} \right) \right] \quad (\text{B.63})$$

$$h_0^2 \tau \frac{\sqrt{\pi}}{2\sqrt{2}} \frac{(1 + \cos^2 \iota)^2}{4} \left[\frac{1}{2\tau^2} + \left(\frac{1}{2\tau^2} - 2\pi^2 f_0^2 \right) e^{-2\pi^2 f_0^2 \tau^2} + 2\pi^2 f_0^2 \left(1 + e^{-2\pi^2 f_0^2 \tau^2} \right) \right] \quad (\text{B.64})$$

$$\begin{aligned} h_0^2 \tau \frac{\sqrt{\pi}}{2\sqrt{2}} \frac{(1 + \cos^2 \iota)^2}{4} \left[\frac{1}{2\tau^2} \left(1 + e^{-2\pi^2 f_0^2 \tau^2} \right) \right. \\ \left. - 2\pi^2 f_0^2 e^{-2\pi^2 f_0^2 \tau^2} + 2\pi^2 f_0^2 \left(1 + e^{-2\pi^2 f_0^2 \tau^2} \right) \right] \quad (\text{B.65}) \end{aligned}$$

$$h_0^2 \tau \frac{\sqrt{\pi}}{2\sqrt{2}} \frac{(1 + \cos^2 \iota)^2}{4} \left[\frac{1}{2\tau^2} \left(1 + e^{-2\pi^2 f_0^2 \tau^2} \right) + 2\pi^2 f_0^2 \right] \quad (\text{B.66})$$

$$\int_{-\infty}^{\infty} \dot{h}_{+, \psi=0}^2(t) dt = \frac{(1 + \cos^2 \iota)^2}{4} h_0^2 \tau \frac{\sqrt{\pi}}{4\sqrt{2}} \left[4\pi^2 f_0^2 + \frac{1}{\tau^2} \left(1 + e^{-2\pi^2 f_0^2 \tau^2} \right) \right] \quad (\text{B.67})$$

Substituting in Q:

$$\frac{(1 + \cos^2 \iota)^2}{4} h_0^2 \frac{Q}{\sqrt{2} \pi f_0} \frac{\sqrt{\pi}}{4\sqrt{2}} \left[4\pi^2 f_0^2 + \frac{2\pi^2 f_0^2}{Q^2} \left(1 + e^{-Q^2} \right) \right] \quad (\text{B.68})$$

$$\int_{-\infty}^{\infty} \dot{h}_{+, \psi=0}^2(t) dt = \frac{(1 + \cos^2 \iota)^2}{4} (4 \pi^2 f_0^2) \frac{h_0^2 Q}{8 \sqrt{\pi} f_0} \left[1 + \frac{1}{2Q^2} (1 + e^{-Q^2}) \right] \quad (\text{B.69})$$

Next $\int_{-\infty}^{\infty} \dot{h}_{\times, \psi=0}^2(t) dt$ will be calculated:

$$\frac{h_0^2}{2} (\cos^2 \iota) \int_{-\infty}^{\infty} e^{-2t^2/\tau^2} \left(-\frac{2t}{\tau^2} \sin(2\pi f_0 t) + 2\pi f_0 \cos(2\pi f_0 t) \right)^2 dt \quad (\text{B.70})$$

$$\begin{aligned} \frac{h_0^2}{2} \cos^2 \iota \int_{-\infty}^{\infty} e^{-2t^2/\tau^2} \left(\frac{4t^2}{\tau^4} \sin^2(2\pi f_0 t) - 2\frac{2t}{\tau^2} \sin(2\pi f_0 t) 2\pi f_0 \cos(2\pi f_0 t) \right. \\ \left. + 4\pi^2 f_0^2 \cos^2(2\pi f_0 t) \right) dt \quad (\text{B.71}) \end{aligned}$$

$$\begin{aligned} \frac{h_0^2}{2} \cos^2 \iota \int_{-\infty}^{\infty} e^{-2t^2/\tau^2} \left(\frac{2t^2}{\tau^4} (1 - \cos(4\pi f_0 t)) - \frac{4t}{\tau^2} \pi f_0 \sin(4\pi f_0 t) \right. \\ \left. + 2\pi^2 f_0^2 (1 + \cos(4\pi f_0 t)) \right) dt \quad (\text{B.72}) \end{aligned}$$

$$\begin{aligned} \frac{h_0^2}{2} \cos^2 \iota \int_0^{\infty} e^{-2t^2/\tau^2} \left(\frac{4t^2}{\tau^4} (1 - \cos(4\pi f_0 t)) - \frac{8t}{\tau^2} \pi f_0 \sin(4\pi f_0 t) \right. \\ \left. + 4\pi^2 f_0^2 (1 + \cos(4\pi f_0 t)) \right) dt \quad (\text{B.73}) \end{aligned}$$

$$\begin{aligned}
& \frac{h_0^2}{2} \cos^2 \iota \\
& \times \left[\frac{4}{\tau^4} \left(\frac{(2(1) - 1)!!}{2(2(2/\tau^2))^1} \frac{\sqrt{\pi}}{\sqrt{2/\tau^2}} - \sqrt{\pi} \frac{2 \left(\sqrt{2/\tau^2} \right)^2 - (4\pi f_0)^2}{8 \left(\sqrt{2/\tau^2} \right)^5} e^{-(4\pi f_0)^2 / (4(\sqrt{2/\tau^2})^2)} \right) \right. \\
& \quad - \frac{8}{\tau^2} \pi f_0 \frac{(4\pi f_0) \sqrt{\pi}}{4 \left(\sqrt{2/\tau^2} \right)^3} e^{-(4\pi f_0)^2 / (4(\sqrt{2/\tau^2})^2)} \\
& \quad \left. + 4\pi^2 f_0^2 \left(\frac{\sqrt{\pi}}{2\sqrt{2/\tau^2}} + \frac{1}{2} \sqrt{\pi / (2/\tau^2)} e^{-(4\pi f_0)^2 / 4(2/\tau^2)} \right) \right] \quad (\text{B.74})
\end{aligned}$$

$$\begin{aligned}
& \frac{h_0^2}{2} \cos^2 \iota \frac{\sqrt{\pi}}{\sqrt{2}} \tau \left[\frac{1}{\tau^2} \left(\frac{1}{2} - \frac{1 - 4\pi^2 f_0^2 \tau^2}{2} e^{-2\pi^2 f_0^2 \tau^2} \right) - 4\pi^2 f_0^2 e^{-2\pi^2 f_0^2 \tau^2} \right. \\
& \quad \left. + 2\pi^2 f_0^2 \left(1 + e^{-2\pi^2 f_0^2 \tau^2} \right) \right] \quad (\text{B.75})
\end{aligned}$$

$$h_0^2 \tau \frac{\sqrt{\pi}}{2\sqrt{2}} \cos^2 \iota \left[\frac{1}{2\tau^2} + \left(-\frac{1}{2\tau^2} + 2\pi^2 f_0^2 \right) e^{-2\pi^2 f_0^2 \tau^2} + 2\pi^2 f_0^2 \left(1 - e^{-2\pi^2 f_0^2 \tau^2} \right) \right] \quad (\text{B.76})$$

$$h_0^2 \tau \frac{\sqrt{\pi}}{2\sqrt{2}} \cos^2 \iota \left[\frac{1}{2\tau^2} + \left(-\frac{1}{2\tau^2} \right) e^{-2\pi^2 f_0^2 \tau^2} + 2\pi^2 f_0^2 \right] \quad (\text{B.77})$$

$$h_0^2 \tau \frac{\sqrt{\pi}}{2\sqrt{2}} \cos^2 \iota \left[2\pi^2 f_0^2 + \frac{1}{2\tau^2} \left(1 - e^{-2\pi^2 f_0^2 \tau^2} \right) \right] \quad (\text{B.78})$$

$$\int_{-\infty}^{\infty} \dot{h}_{\times, \psi=0}^2(t) dt = (\cos^2 \iota) h_0^2 \tau \frac{\sqrt{\pi}}{4\sqrt{2}} \left[4\pi^2 f_0^2 + \frac{1}{\tau^2} \left(1 - e^{-2\pi^2 f_0^2 \tau^2} \right) \right] \quad (\text{B.79})$$

Substituting in Q:

$$(\cos^2 \iota) h_0^2 \frac{Q\sqrt{\pi}}{(\sqrt{2}\pi f_0)4\sqrt{2}} \left[4\pi^2 f_0^2 + \frac{2\pi^2 f_0^2}{Q^2} \left(1 - e^{-Q^2} \right) \right] \quad (\text{B.80})$$

$$(\cos^2 \iota) h_0^2 \frac{Q}{8\sqrt{\pi}f_0} (4\pi^2 f_0^2) \left[1 + \frac{1}{2Q^2} \left(1 - e^{-Q^2} \right) \right] \quad (\text{B.81})$$

$$\int_{-\infty}^{\infty} \dot{h}_{\times, \psi=0}^2(t) dt = (\cos^2 \iota) (4 \pi^2 f_0^2) \frac{h_0^2 Q}{8 \sqrt{\pi} f_0} \left[1 + \frac{1}{2Q^2} (1 - e^{-Q^2}) \right] \quad (\text{B.82})$$

Substituting (B.69) and (B.82) in to the full time integral in (B.44):

$$\begin{aligned} \int_{-\infty}^{\infty} \left(\dot{h}_{+, \psi=0}^2(t) + \dot{h}_{\times, \psi=0}^2(t) \right) dt = \\ \frac{(1 + \cos^2 \iota)^2}{4} (4 \pi^2 f_0^2) \frac{h_0^2 Q}{8 \sqrt{\pi} f_0} \left[1 + \frac{1}{2Q^2} (1 + e^{-Q^2}) \right] \\ + (\cos^2 \iota) (4 \pi^2 f_0^2) \frac{h_0^2 Q}{8 \sqrt{\pi} f_0} \left[1 + \frac{1}{2Q^2} (1 - e^{-Q^2}) \right] \end{aligned} \quad (\text{B.83})$$

$$\begin{aligned} \frac{(1 + \cos^2 \iota)^2}{4} (4 \pi^2 f_0^2) \frac{h_0^2 Q}{8 \sqrt{\pi} f_0} \left[1 + \frac{1}{2Q^2} + \frac{1}{2Q^2} e^{-Q^2} \right] \\ + (\cos^2 \iota) (4 \pi^2 f_0^2) \frac{h_0^2 Q}{8 \sqrt{\pi} f_0} \left[1 + \frac{1}{2Q^2} - \frac{1}{2Q^2} e^{-Q^2} \right] \end{aligned} \quad (\text{B.84})$$

$$\begin{aligned} (4 \pi^2 f_0^2) \frac{h_0^2 Q}{8 \sqrt{\pi} f_0} \left[\left(\frac{(1 + \cos^2 \iota)^2}{4} + \cos^2 \iota \right) \left(1 + \frac{1}{2Q^2} \right) \right. \\ \left. + \left(\frac{(1 + \cos^2 \iota)^2}{4} - \cos^2 \iota \right) \frac{1}{2Q^2} e^{-Q^2} \right] \end{aligned} \quad (\text{B.85})$$

$$\begin{aligned} \int_{-\infty}^{\infty} \left(\dot{h}_{+, \psi=0}^2(t) + \dot{h}_{\times, \psi=0}^2(t) \right) dt = (4 \pi^2 f_0^2) \frac{h_0^2 Q}{8 \sqrt{\pi} f_0} \left[\left(\frac{(1 + \cos^2 \iota)^2}{4} + \cos^2 \iota \right) \right. \\ \left. + \frac{1}{2Q^2} \left\{ \left(\frac{(1 + \cos^2 \iota)^2}{4} + \cos^2 \iota \right) + \left(\frac{(1 + \cos^2 \iota)^2}{4} - \cos^2 \iota \right) e^{-Q^2} \right\} \right] \end{aligned} \quad (\text{B.86})$$

Substituting (B.30) and (B.31) in to (B.86) gives:

$$\int_{-\infty}^{\infty} \left(\dot{h}_{+, \psi=0}^2(t) + \dot{h}_{\times, \psi=0}^2(t) \right) dt = 4 \pi^2 f_0^2 \left[(h_{\text{rss}}^{\text{HQ}})^2 + \frac{1}{2Q^2} h_{\text{rss}}^2 \right] \quad (\text{B.87})$$

Returning to (B.45), the angular integrals can now be taken care of. First, the integral over ϕ . There is no ϕ dependence in h , so this is just:

$$\int_0^{2\pi} (1) d\phi = 2\pi \quad (\text{B.88})$$

Both h_{rss} and $h_{\text{rss}}^{\text{HQ}}$ have ι dependence, so (B.87) will be inside the integral over ι . The dependencies are of two forms: $\frac{(1+\cos^2 \iota)^2}{4}$ and $\cos^2 \iota$. Therefore the integrals over ι that must be solved are of the following forms:

$$\int \frac{(1 + \cos^2 \iota)^2}{4} \sin \iota d\iota = -\frac{1}{4} \left(\frac{1}{5} \cos^5 \iota + \frac{2 \cos^3 \iota}{3} + \cos \iota \right) \quad (\text{B.89})$$

$$\int (\cos^2 \iota) \sin \iota d\iota = -\frac{1}{3} \cos^3 \iota \quad (\text{B.90})$$

When integrated from 0 to π these become:

$$\int_0^\pi \frac{(1 + \cos^2 \iota)^2}{4} \sin \iota d\iota = \frac{1}{4} \left(\frac{1}{5} + \frac{2}{3} + 1 \right) - \frac{1}{4} \left(-\frac{1}{5} - \frac{2}{3} - 1 \right) = 2 \left(\frac{1}{4} \right) \left(\frac{28}{15} \right) = \frac{14}{15} \quad (\text{B.91})$$

$$\int_0^\pi (\cos^2 \iota) \sin \iota d\iota = \frac{1}{3} - \frac{-1}{3} = \frac{2}{3} \quad (\text{B.92})$$

Both $\frac{(1+\cos^2 \iota)^2}{4}$ and $\cos^2 \iota$ appear together in (B.86). The integrals over ι of these appearances can be calculated using B.91 and (B.92):

$$\int_0^\pi \left(\frac{(1 + \cos^2 \iota)^2}{4} + \cos^2 \iota \right) d\iota = \frac{14}{15} + \frac{2}{3} = \frac{24}{15} = \frac{8}{5} \quad (\text{B.93})$$

$$\int_0^\pi \left(\frac{(1 + \cos^2 \iota)^2}{4} - \cos^2 \iota \right) d\iota = \frac{14}{15} - \frac{2}{3} = \frac{4}{15} \quad (\text{B.94})$$

Now E_{GW} can be calculated. First (B.86) and (B.88) are plugged into (B.45):

$$E_{\text{GW}} = \frac{c^3}{16\pi G} \int_{-\infty}^{\infty} \int_0^{2\pi} \int_0^{\pi} \left(\dot{h}_{+, \psi=0}^2(t) + \dot{h}_{\times, \psi=0}^2(t) \right) r^2 \sin \iota \, d\iota \, d\phi \, dt =$$

$$\frac{2\pi c^3 r^2}{16\pi G} \int_0^{\pi} \int_{-\infty}^{\infty} \left(\dot{h}_{+, \psi=0}^2(t) + \dot{h}_{\times, \psi=0}^2(t) \right) dt \sin \iota \, d\iota \quad (\text{B.95})$$

$$= \frac{c^3 r^2}{8G} \int_0^{\pi} (4\pi^2 f_0^2) \frac{h_0^2 Q}{8\sqrt{\pi} f_0} \left[\left(\frac{(1 + \cos^2 \iota)^2}{4} + \cos^2 \iota \right) \right.$$

$$\left. + \frac{1}{2Q^2} \left\{ \left(\frac{(1 + \cos^2 \iota)^2}{4} + \cos^2 \iota \right) + \left(\frac{(1 + \cos^2 \iota)^2}{4} - \cos^2 \iota \right) e^{-Q^2} \right\} \right] \sin \iota \, d\iota \quad (\text{B.96})$$

$$= (4\pi^2 f_0^2) \frac{c^3 r^2}{8G} \frac{h_0^2 Q}{8\sqrt{\pi} f_0} \int_0^{\pi} \left[\left(\frac{(1 + \cos^2 \iota)^2}{4} + \cos^2 \iota \right) \right.$$

$$\left. + \frac{1}{2Q^2} \left\{ \left(\frac{(1 + \cos^2 \iota)^2}{4} + \cos^2 \iota \right) + \left(\frac{(1 + \cos^2 \iota)^2}{4} - \cos^2 \iota \right) e^{-Q^2} \right\} \right] \sin \iota \, d\iota \quad (\text{B.97})$$

$$= (4\pi^2 f_0^2) \frac{c^3 r^2}{8G} \frac{h_0^2 Q}{8\sqrt{\pi} f_0} \left[\left(\frac{8}{5} \right) + \frac{1}{2Q^2} \left\{ \left(\frac{8}{5} \right) + \left(\frac{4}{15} \right) e^{-Q^2} \right\} \right] \quad (\text{B.98})$$

$$= \frac{8}{5} (4\pi^2 f_0^2) \frac{c^3 r^2}{8G} \frac{h_0^2 Q}{8\sqrt{\pi} f_0} \left[1 + \frac{1}{2Q^2} \left(1 + \frac{1}{6} e^{-Q^2} \right) \right] \quad (\text{B.99})$$

$$E_{\text{GW}} = h_0^2 r^2 Q f_0 \frac{c^3 \pi^{3/2}}{10G} \left[1 + \frac{1}{2Q^2} \left(1 + \frac{1}{6} e^{-Q^2} \right) \right] \quad (\text{B.100})$$

For high Q , (B.100) can be approximated as:

$$E_{\text{GW}}^{\text{HQ}} \approx \frac{c^3 \pi^{3/2}}{10G} h_0^2 r^2 Q f_0 \quad (\text{B.101})$$

In terms of τ , E_{GW} becomes:

$$E_{\text{GW}} = h_0^2 r^2 \sqrt{2} \pi f_0 \tau f_0 \frac{c^3 \pi^{3/2}}{10 G} \left[1 + \frac{1}{2 (\sqrt{2} \pi f_0 \tau)^2} \left(1 + \frac{1}{6} e^{-(\sqrt{2} \pi f_0 \tau)^2} \right) \right] \quad (\text{B.102})$$

$$E_{\text{GW}} = h_0^2 r^2 f_0^2 \tau \frac{c^3 \pi^{5/2}}{5 \sqrt{2} G} \left[1 + \frac{1}{4 \pi^2 f_0^2 \tau^2} \left(1 + \frac{1}{6} e^{-2 \pi^2 f_0^2 \tau^2} \right) \right] \quad (\text{B.103})$$

In terms of τ , $E_{\text{GW}}^{\text{HQ}}$ becomes:

$$E_{\text{GW}}^{\text{HQ}} \approx \frac{c^3 \pi^{3/2}}{10 G} h_0^2 r^2 \sqrt{2} \pi f_0 \tau f_0 \quad (\text{B.104})$$

$$E_{\text{GW}}^{\text{HQ}} \approx \frac{c^3 \pi^{5/2}}{5 \sqrt{2} G} h_0^2 r^2 f_0^2 \tau \quad (\text{B.105})$$

B.3. E_{GW} and h_{rss} for a Half Sine-Gaussian

E_{GW} and h_{rss} have been calculated above for a sine-Gaussian waveform. However, the waveforms used in this analysis are half sine-Gaussians. A half sine-Gaussian will have half the energy of a sine-Gaussian, and h_{rss} will be a factor of $\sqrt{2}$ less than for a sine-Gaussian. For a half sine-Gaussian, (B.30) and (B.31) become:

$$h_{\text{rss}} = \frac{h_0}{4\pi^{1/4}} \sqrt{\frac{Q}{f_0}} \sqrt{\left(\frac{(1 + \cos^2 \iota)^2}{4} + \cos^2 \iota \right) + \left(\frac{(1 + \cos^2 \iota)^2}{4} - \cos^2 \iota \right) e^{-Q^2}} \quad (\text{B.106})$$

$$h_{\text{rss}}^{\text{HQ}} \approx \frac{h_0}{4\pi^{1/4}} \sqrt{\frac{Q}{f_0}} \sqrt{\left(\frac{(1 + \cos^2 \iota)^2}{4} + \cos^2 \iota \right)} \quad (\text{B.107})$$

For a half sine-Gaussian, (B.100) and (B.101) become:

$$E_{\text{GW}} = h_0^2 r^2 Q f_0 \frac{c^3 \pi^{3/2}}{20 G} \left[1 + \frac{1}{2 Q^2} \left(1 + \frac{1}{6} e^{-Q^2} \right) \right] \quad (\text{B.108})$$

$$E_{\text{GW}}^{\text{HQ}} \approx \frac{c^3 \pi^{3/2}}{20G} h_0^2 r^2 Q f_0 \quad (\text{B.109})$$

B.4. Comparing to Fluence

As a consistency check, the relationship between the energy, fluence and distance can be found and compared to the same relation as stated in [79]. $E_{\text{GW}}^{\text{HQ}}$ for a sine-Gaussian will be rewritten in terms of the fluence for a circularly polarized waveform ($\iota = 0$). Using (B.44) and (B.87), the fluence in (B.39) can be rewritten as:

$$F = \frac{c^3}{16\pi G} \int \left(\dot{h}_+^2(t) + \dot{h}_\times^2(t) \right) dt = \frac{c^3}{16\pi G} 4\pi^2 f_0^2 \left[\left(h_{\text{rss}}^{\text{HQ}} \right)^2 + \frac{1}{2Q^2} h_{\text{rss}}^2 \right] \quad (\text{B.110})$$

$$F = \frac{\pi c^3 f_0^2}{4G} \left[\left(h_{\text{rss}}^{\text{HQ}} \right)^2 + \frac{1}{2Q^2} h_{\text{rss}}^2 \right] \quad (\text{B.111})$$

For $\iota = 0$, the fluence is:

$$F_{\iota=0^\circ} = \frac{\pi c^3 f_0^2}{4G} \left(\frac{h_0^2 Q}{4\sqrt{\pi} f_0} \right) \left[1 + \frac{1}{2Q^2} \right] \quad (\text{B.112})$$

$$F_{\iota=0^\circ} = \frac{\sqrt{\pi} c^3}{16G} h_0^2 Q f_0 \left[1 + \frac{1}{2Q^2} \right] \quad (\text{B.113})$$

For high Q , the fluence can be approximated as:

$$F^{\text{HQ}} \approx \frac{\pi c^3 f_0^2}{4G} \left(h_{\text{rss}}^{\text{HQ}} \right)^2 \quad (\text{B.114})$$

And for $\iota = 0$, using either (B.113) or (B.114), F^{HQ} can be approximated as:

$$F_{\iota=0^\circ}^{\text{HQ}} \approx \frac{\pi c^3 f_0^2}{4G} \left(\frac{h_0^2 Q}{4\sqrt{\pi} f_0} \right) \quad (\text{B.115})$$

$$F_{\iota=0^\circ}^{\text{HQ}} \approx \frac{\sqrt{\pi} c^3}{16G} h_0^2 Q f_0 \quad (\text{B.116})$$

$E_{\text{GW}}^{\text{HQ}}$ can now be represented in terms of $F_{\iota=0^\circ}^{\text{HQ}}$:

$$E_{\text{GW}}^{\text{HQ}} \approx \frac{c^3 \pi^{3/2}}{10 G} h_0^2 r^2 Q f_0 = \frac{8 \pi r^2 \sqrt{\pi} c^3}{5 \cdot 16 G} h_0^2 Q f_0 = \frac{8 \pi r^2}{5} F_{\iota=0^\circ}^{\text{HQ}} \quad (\text{B.117})$$

$$E_{\text{GW}}^{\text{HQ}} \approx \frac{2}{5} 4 \pi r^2 F_{\iota=0^\circ}^{\text{HQ}} \quad (\text{B.118})$$

(B.118) can be rearranged into:

$$\frac{5}{2} \frac{E_{\text{GW}}^{\text{HQ}}}{4 \pi F_{\iota=0^\circ}^{\text{HQ}}} \approx r^2 \quad (\text{B.119})$$

$$r \approx \left(\frac{5}{2} \frac{E_{\text{GW}}^{\text{HQ}}}{4 \pi F_{\iota=0^\circ}^{\text{HQ}}} \right)^{1/2} \quad (\text{B.120})$$

(B.120) agrees with Equation 6 in [79].

B.5. Comparing to Isotropic Sine-Gaussian Emission

As an additional consistency check, the energy limits calculated in this appendix can be compared to those calculated in [100]. The waveform considered now is a sine-Gaussian with plus polarization and is isotropic in magnitude. (B.7) and (B.8) now become:

$$h_{+, \psi=0} = h_0 e^{-t^2/\tau^2} \sin(2 \pi f_0 t) \sin 2\psi \quad (\text{B.121})$$

$$h_{\times, \psi=0} = 0 \quad (\text{B.122})$$

The amplitude in h_+ is now h_0 instead of $h_0/\sqrt{2}$ because the entire energy of the waveform is now in the plus polarization. (B.45) would now become:

$$E_{\text{GW}} = \frac{c^3}{16 \pi G} \int_{-\infty}^{\infty} \int_0^{2\pi} \int_0^\pi \dot{h}_{+, \psi=0}^2(t) r^2 \sin \iota \, d\iota \, d\phi \, dt \quad (\text{B.123})$$

$$E_{\text{GW}} = \frac{c^3 r^2}{4G} \int_{-\infty}^{\infty} \dot{h}_{+, \psi=0}^2(t) dt \quad (\text{B.124})$$

$$E_{\text{GW}} = \frac{c^3 r^2}{4G} \int_{-\infty}^{\infty} \left[\frac{d}{dt} \left(h_0 \sin 2\pi f_0 t e^{-t^2/\tau^2} \right) \right]^2 dt \quad (\text{B.125})$$

Using (B.47) and (B.82) and making the replacements of $h_0/\sqrt{2} \rightarrow h_0$ and $\cos \iota \rightarrow 1$, the integral in (B.125) can be calculated:

$$\int_{-\infty}^{\infty} \left[\frac{d}{dt} \left(h_0 \sin 2\pi f_0 t e^{-t^2/\tau^2} \right) \right]^2 dt = (4\pi^2 f_0^2) \frac{h_0^2 Q}{4\sqrt{\pi} f_0} \left[1 + \frac{1}{2Q^2} (1 - e^{-Q^2}) \right] \quad (\text{B.126})$$

(B.126) is the same as equation 29 in [100].

As a last step, $E_{\text{GW}}^{\text{HQ}}$ can be found:

$$E_{\text{GW}} = \frac{c^3 r^2}{4G} (4\pi^2 f_0^2) \frac{h_0^2 Q}{4\sqrt{\pi} f_0} \left[1 + \frac{1}{2Q^2} (1 - e^{-Q^2}) \right] \quad (\text{B.127})$$

$$E_{\text{GW}}^{\text{HQ}} \approx \frac{c^3 r^2}{4G} (4\pi^2 f_0^2) \frac{h_0^2 Q}{4\sqrt{\pi} f_0} \quad (\text{B.128})$$

(B.128) agrees with equation 12 in [100].

APPENDIX C

CALIBRATION ERROR

L1	Overall scaling = $1.02(1 + 0.13 - 0.01)$				
	Timing error = $[-10, +45]\mu s$				
	Static frequency dependence recommendation				
	Epoch		[40, 70] Hz	[70, 2000] Hz	[2000, 5000] Hz
	S6a	$ h(f) $	10%	14%	20%
$ h(t) $		$\sqrt{10^2 + 3^2} = 10\%$	$\sqrt{14^2 + 3^2} = 14\%$	$\sqrt{20^2 + 3^2} = 20\%$	
$\angle h(f)$		7 deg	9 deg	6 deg	
$\angle h(t)$		$\sqrt{7^2 + 4^2} = 8$ deg	$\sqrt{9^2 + 4^2} = 10$ deg	$\sqrt{6^2 + 12^2} = 13$ deg	
S6b	$ h(f) $	5%	18%	19%	
	$ h(t) $	$\sqrt{5^2 + 7^2} = 9\%$	$\sqrt{18^2 + 7^2} = 19\%$	$\sqrt{19^2 + 4^2} = 19\%$	
	$\angle h(f)$	4 deg	7 deg	5 deg	
	$\angle h(t)$	$\sqrt{4^2 + 3.5^2} = 5$ deg	$\sqrt{7^2 + 3.5^2} = 8$ deg	$\sqrt{5^2 + 2^2} = 5$ deg	
H1	Overall scaling = $1.014(1 + 0.025 - 0.004)$				
	Timing error = $[0, +30]\mu s$				
	Static frequency dependence recommendation				
	Epoch		[40, 70] Hz	[70, 2000] Hz	[2000, 5000] Hz
	S6a	$ h(f) $	13%	8%	40%
$ h(t) $		$\sqrt{13^2 + 4^2} = 14\%$	$\sqrt{8^2 + 4^2} = 9\%$	$\sqrt{40^2 + 6^2} = 40\%$	
$\angle h(f)$		7 deg	5 deg	27 deg	
$\angle h(t)$		$\sqrt{7^2 + 2^2} = 7$ deg	$\sqrt{5^2 + 2^2} = 5$ deg	$\sqrt{27^2 + 4.5^2} = 27$ deg	
S6b	$ h(f) $	11%	16%	40%	
	$ h(t) $	$\sqrt{11^2 + 3^2} = 11\%$	$\sqrt{16^2 + 3^2} = 16\%$	$\sqrt{40^2 + 6.5^2} = 41\%$	
	$\angle h(f)$	6 deg	5 deg	27 deg	
	$\angle h(t)$	$\sqrt{6^2 + 2^2} = 6$ deg	$\sqrt{5^2 + 2^2} = 5$ deg	$\sqrt{27^2 + 5^2} = 28$ deg	

TABLE C.1. Recommended calibration error for S6. Reproduced from [102].

Calibration error affects the strain Fourier transform $\tilde{h}_I(f)$ with timing error (τ_I), phase error ($\delta_I(f)$) and amplitude error ($\lambda_I(f)$) [103]:

$$\tilde{h}_I(f) \rightarrow e^{2\pi i f \tau_I} e^{i\delta_I(f)} \lambda_I(f) \tilde{h}_I(f) \quad (\text{C.1})$$

L1	Overall scaling = $1.02(1 + 0.13 - 0.01)$				
	Timing error = $[-10, +45]\mu s$				
	Static frequency dependence recommendation				
	Epoch		[40, 70] Hz	[70, 2000] Hz	[2000, 5000] Hz
	S6a	$ h(f) $ $ h(t) $ $\angle h(f)$ $\angle h(t)$	10% $\sqrt{10^2 + 3^2} = 10\%$ 7 deg $\sqrt{7^2 + 4^2} = 8$ deg	14% $\sqrt{14^2 + 3^2} = 14\%$ 9 deg $\sqrt{9^2 + 4^2} = 10$ deg	20% $\sqrt{20^2 + 3^2} = 20\%$ 6 deg $\sqrt{6^2 + 12^2} = 13$ deg
S6b	$ h(f) $ $ h(t) $ $\angle h(f)$ $\angle h(t)$	5% $\sqrt{5^2 + 7^2} = 9\%$ 4 deg $\sqrt{4^2 + 3.5^2} = 5$ deg	18% $\sqrt{18^2 + 7^2} = 19\%$ 7 deg $\sqrt{7^2 + 3.5^2} = 8$ deg	19% $\sqrt{19^2 + 4^2} = 19\%$ 5 deg $\sqrt{5^2 + 2^2} = 5$ deg	
H1	Overall scaling = $1.014(1 + 0.025 - 0.004)$				
	Timing error = $[0, +30]\mu s$				
	Static frequency dependence recommendation				
	Epoch		[40, 70] Hz	[70, 2000] Hz	[2000, 3000] + [4000, 5000] Hz
	S6a	$ h(f) $ $ h(t) $ $\angle h(f)$ $\angle h(t)$	13% $\sqrt{13^2 + 4^2} = 14\%$ 7 deg $\sqrt{7^2 + 2^2} = 7$ deg	8% $\sqrt{8^2 + 4^2} = 9\%$ 5 deg $\sqrt{5^2 + 2^2} = 5$ deg	11% $\sqrt{11^2 + 6^2} = 13\%$ 8 deg $\sqrt{8^2 + 4.5^2} = 9$ deg
S6b	$ h(f) $ $ h(t) $ $\angle h(f)$ $\angle h(t)$	11% $\sqrt{11^2 + 3^2} = 11\%$ 6 deg $\sqrt{6^2 + 2^2} = 6$ deg	16% $\sqrt{16^2 + 3^2} = 16\%$ 5 deg $\sqrt{5^2 + 2^2} = 5$ deg	15% $\sqrt{15^2 + 6.5^2} = 16\%$ 8 deg $\sqrt{8^2 + 5^2} = 9$ deg	

TABLE C.2. Recommended calibration error for S6. Derived from data in [102] excluding the band [3000, 4000] Hz in H1.

From [102], the calibration error in the frequency response function can be represented as:

$$R(f) = A_0(1 + \delta A_+ - \delta A_-) \text{abs}(\eta_R^0(f)) \exp[i(\Delta\phi_R(f) - 2\pi f\tau_R)] \eta_\gamma(f) R_M(f) \quad (\text{C.2})$$

R is the “true” response and R_M is the model response [102]. A_0 and δA_\pm are the overall scaling error. τ is the timing error, η_γ is the time evolution error and η_R^0 is the rest of the frequency dependent scaling error. $\Delta\phi_R$ is the phase error of η_R^0 .

Phase error including timing error:

$$\text{Phase Error} = \delta_I(f)$$

$$\text{Timing Error} = 2\pi i f \tau_I = \delta_{I\text{timing}}(f)$$

$$\delta_{I\text{tot}}(f) = \sqrt{\delta_I(f)^2 + \delta_{I\text{timing}}(f)^2}$$

While normally useful, given (C.1) instead use:

$$\delta_{I\text{tot}}(f) = \delta_I(f) + \delta_{I\text{timing}}(f)$$

$$|\tilde{h}_1(f)||\tilde{h}_2(f)| \rightarrow |\tilde{h}_1(f)||\tilde{h}_2(f)| \cos(\delta_{2\text{tot}}(f) - \delta_{1\text{tot}}(f))$$

Include the calibration error in the amplitude:

$$\lambda_I(f) = A_0(1 + \delta A_+ - \delta A_-) |\eta_R^0(f)| \eta_\gamma(f)$$

$$\begin{aligned} |\tilde{h}_1(f)||\tilde{h}_2(f)| \rightarrow |\tilde{h}_1(f)||\tilde{h}_2(f)| (A_0(1 + \delta A_+ - \delta A_-) |\eta_R^0(f)| \eta_\gamma(f))^2 \\ \times \cos(\delta_{2\text{tot}}(f) - \delta_{1\text{tot}}(f)) \end{aligned}$$

The time evolution error is much smaller than the “static frequency dependence error”, and is thus neglected [102]. Let $|\Delta h(f)|$ be the frequency dependent error not including the timing error:

$$|\Delta h(f)| = |\eta_R^0(f)| \eta_\gamma(f) \approx |\eta_R^0(f)|$$

Which gives:

$$\begin{aligned} |\tilde{h}_1(f)||\tilde{h}_2(f)| \rightarrow |\tilde{h}_1(f)||\tilde{h}_2(f)| A_1 A_2 (1 + \delta A_{+1} - \delta A_{-1})(1 + \delta A_{+2} - \delta A_{2-}) \\ \times |\Delta h(f)_1| |\Delta h(f)_2| \cos(\delta_{2\text{tot}}(f) - \delta_{1\text{tot}}(f)) \quad (\text{C.3}) \end{aligned}$$

$$\begin{aligned}
|\Delta\tilde{h}_1(f)||\Delta\tilde{h}_2(f)| &\rightarrow A_1A_2(1 + \delta A_{+1} - \delta A_{-1})(1 + \delta A_{+2} - \delta A_{2-}) \\
&\times |\Delta h(f)_1| |\Delta h(f)_2| \cos(\delta_{2\text{tot}}(f) - \delta_{1\text{tot}}(f)) \quad (\text{C.4})
\end{aligned}$$

For the timing plus phase error ($\delta\tau_{\text{max}} = 45\mu\text{s}$):

$$\Delta\delta_{\text{max}}(f) = 2\pi f 45\mu\text{s} + \delta_1(f) + \delta_2(f)$$

Approximating with the time dependent version for the entire band, the frequency dependence drops out except for the timing error part:

$$\Delta\delta_{\text{max}}(t) = 2\pi f 45\mu\text{s} + \delta_1(t) + \delta_2(t)$$

Amplitude calibration error:

$$\lambda_I(f) = A_0(1 + \delta A_+ - \delta A_-) |\Delta h(f)|$$

$$\lambda_I(t) = A_0(1 + \delta A_+ - \delta A_-) |\Delta h(t)|$$

$$\lambda_I(t) = A_0 \left(1 + \sqrt{\delta A_+^2 + |\Delta h(t)|^2} - \sqrt{\delta A_-^2 + |\Delta h(t)|^2} \right)$$

$$\begin{aligned}
\lambda_1(t)\lambda_2(t) &= A_1A_2 \left(1 + \sqrt{\delta A_{+1}^2 + \delta A_{+2}^2 + |\Delta h_1(t)|^2 + |\Delta h_2(t)|^2} \right. \\
&\quad \left. - \sqrt{\delta A_{-1}^2 + \delta A_{-2}^2 + |\Delta h_1(t)|^2 + |\Delta h_2(t)|^2} \right) \quad (\text{C.5})
\end{aligned}$$

The calibration error of two measured strain values from two detectors multiplied together ($h_{0\text{measured } 1}h_{0\text{measured } 2} = h_{0\text{m } 1}h_{0\text{m } 2}$) can be represented as:

$$h_{01}h_{02} \cos(\delta_{2\text{tot}}(f) - \delta_{1\text{tot}}(f)) = h_{0\text{m } 1}h_{0\text{m } 2}\lambda_1(t)\lambda_2(t)$$

Worst case with $\Delta\delta_{\text{max}}(f)$ and δA_+ :

$$h_{01}h_{02} \cos(2\pi f 45\mu\text{s} + \delta_1(t) + \delta_2(t)) = h_{0\text{m } 1}h_{0\text{m } 2}A_1A_2 \left(1 + \sqrt{\delta A_{+1}^2 + \delta A_{+2}^2 + |\Delta h_1(t)|^2 + |\Delta h_2(t)|^2} \right) \quad (\text{C.6})$$

$$\frac{h_{01}h_{02}}{h_{0\text{m } 1}h_{0\text{m } 2}} = A_1A_2 \frac{1 + \sqrt{\delta A_{+1}^2 + \delta A_{+2}^2 + |\Delta h_1(t)|^2 + |\Delta h_2(t)|^2}}{\cos(2\pi f 45\mu\text{s} + \delta_1(t) + \delta_2(t))} \quad (\text{C.7})$$

Best case with $\Delta\delta(f) = 0$ and δA_- :

$$h_{01}h_{02} = h_{0\text{m } 1}h_{0\text{m } 2}A_1A_2 \left(1 - \sqrt{\delta A_{-1}^2 + \delta A_{-2}^2 + |\Delta h_1(t)|^2 + |\Delta h_2(t)|^2} \right) \quad (\text{C.8})$$

$$\frac{h_{01}h_{02}}{h_{0\text{m } 1}h_{0\text{m } 2}} = A_1A_2 \left(1 - \sqrt{\delta A_{-1}^2 + \delta A_{-2}^2 + |\Delta h_1(t)|^2 + |\Delta h_2(t)|^2} \right) \quad (\text{C.9})$$

REFERENCES CITED

- [1] A. Einstein. Fundamental ideas and problems of the theory of relativity. *Nobel Lectures*, Physics 1901-1921, 1967. http://www.nobelprize.org/nobel_prizes/physics/laureates/1921/einstein-lecture.html.
- [2] A. Einstein. Die feldgleichungen der gravitation (the field equations of gravitation). In *Königlich Preußische Akademie der Wissenschaften. Sitzungsberichte der Physikalisch-mathematischen Klasse*, pages 844–847, Berlin, 1915. http://www.itp.kit.edu/~sahlmann/pdfs/field_equations.pdf.
- [3] K. S. Thorne. Gravitational radiation. In S. W. Hawking and W. Israel, editors, *300 Years of Gravitation*. Cambridge University Press, Cambridge, 1987.
- [4] A. Einstein. Näherungsweise integration der feldgleichungen der gravitation (approximative integration of the field equations of gravitation). In *Königlich Preußische Akademie der Wissenschaften. Sitzungsberichte der Physikalisch-mathematischen Klasse*, pages 688–696, Berlin, 1916.
- [5] The Nobel Prize in Physics 1993. http://www.nobelprize.org/nobel_prizes/physics/laureates/1993/. Accessed: 23 Feb 2014.
- [6] J. M. Weisberg, D. J. Nice, and J. H. Taylor. Timing measurements of the relativistic binary pulsar PSR B1913+16. *The Astrophysical Journal*, 722:1030, 2010. DOI: <http://dx.doi.org/10.1088/0004-637X/722/2/1030>.
- [7] B. P. Abbott et al. Observation of gravitational waves from a binary black hole merger. *Physical Review Letters*, 116:061102, 2016.
- [8] K. Riles. Gravitational waves: Sources, detectors and searches. *Progress in Particle and Nuclear Physics*, 68:1–54, 2013.
- [9] S. Mereghetti, J. A. Pons, and A. Melatos. Magnetars: Properties, origin and evolution. *Space Science Reviews*, 191(1):315–338, 2015.
- [10] A. Corsi and B. J. Owen. Maximum gravitational-wave energy emissible in magnetar flares. *Physical Review D*, 83:104014, 2011.
- [11] S. M. Carroll. *Spacetime and Geometry: An Introduction to General Relativity*. Addison Wesley, San Francisco, California, USA, 2004.
- [12] B. F. Schutz. *A First Course in General Relativity*. Cambridge University Press, New York, USA, second edition, 2009.

- [13] A. Einstein. Kosmologische betrachtungen zur allgemeinen relativitätstheorie (cosmological considerations in the general theory of relativity). *Preussische Akademie der Wissenschaften. Sitzungsberichte*, pages 142–152, 1917.
- [14] E. Hubble. A relation between distance and radial velocity among extra-galactic nebulae. *Proceedings of the National Academy of Sciences*, 15:168–173, 1929.
- [15] S. M. Carroll. The cosmological constant. *Living Reviews in Relativity*, 4(1), 2001. URL (cited on 3/7/2016): <http://www.livingreviews.org/lrr-2001-1>.
- [16] T. T. Fricke et al. DC readout experiment in Enhanced LIGO. *Classical and Quantum Gravity*, 29:065005, 2012.
- [17] J. R. Smith for the LIGO Scientific Collaboration. The path to the Enhanced and Advanced LIGO gravitational-wave detectors. *Classical and Quantum Gravity*, 26:114013, 2009.
- [18] R. Adhikari, P. Fritschel, and S. Waldman. Enhanced LIGO. LIGO Document LIGO-T060156-01-I, 2006.
- [19] J. Aasi et al. Characterization of the ligo detectors during their sixth science run. *Classical and Quantum Gravity*, 32:115012, 2015.
- [20] A. A. Michelson. The relative motion of the Earth and the luminiferous ether. *American Journal of Science*, 22:120–129, 1881.
- [21] A. A. Michelson and E. W. Morley. On the relative motion of the Earth and the luminiferous ether. *American Journal of Science*, 34:333–345, 1887.
- [22] R. Weiss. Electromagnetically coupled broadband gravitational antenna. *Quarterly Progress Report, Research Laboratory of Electronics, MIT*, 105:54, 1972.
- [23] B. P. Abbott et al. LIGO: the Laser Interferometer Gravitational-Wave Observatory. *Reports on Progress in Physics*, 72:076901, 2009.
- [24] E. D. Black and R. N. Gutenkunst. An introduction to signal extraction in interferometric gravitational-wave detectors. LIGO Document LIGO-P020029-01, 2002.
- [25] J. Abadie et al. Calibration of the LIGO gravitational wave detectors in the fifth science run. *Nuclear Instruments and Methods in Physics Research Section A: Accelerators, Spectrometers, Detectors and Associated Equipment*, 624:223–240, 2010.
- [26] The LIGO Scientific Collaboration et al. Advanced LIGO. *Classical and Quantum Gravity*, 32:074001, 2015.

- [27] S. Hild et al. DC-readout of a signal-recycled gravitational wave detector. *Classical and Quantum Gravity*, 26:055012, 2009.
- [28] S. Ballmer et al. Thermal compensation system description. Technical Report LIGO-T050064-00-R, 2005.
- [29] R. DeRosa et al. Global feed-forward vibration isolation in a km scale interferometer. *Classical and Quantum Gravity*, 29:215008, 2012.
- [30] R. Abbott et al. Seismic isolation enhancements for initial and Advanced LIGO. *Classical and Quantum Gravity*, 21:S915, 2004.
- [31] A. Effler et al. Environmental influences on the LIGO gravitational wave detectors during the 6th science run. *Classical and Quantum Gravity*, 32:035017, 2015.
- [32] J. Aasi et al. Search for gravitational waves from binary black hole inspiral, merger, and ringdown in LIGO-Virgo data from 2009–2010. *Physical Review D*, 87:022002, 2013.
- [33] A. Buonanno et al. Approaching faithful templates for nonspinning binary black holes using the effective-one-body approach. *Physical Review D*, 76:104049, 2007.
- [34] J. Abadie et al. Search for gravitational waves from binary black hole inspiral, merger, and ringdown. *Physical Review D*, 83:122005, 2011.
- [35] J. Abadie et al. Search for gravitational waves from low mass compact binary coalescence in LIGO’s sixth science run and Virgo’s science runs 2 and 3. *Physical Review D*, 85:082002, 2012.
- [36] C. Cutler and K. S. Thorne. An overview of gravitational wave sources. In N. Bishop and S. D. Maharaj, editors, *General Relativity and Gravitation, Proceedings of the 16th International Conference*, pages 72–111. World Scientific, 2002.
- [37] J. Aasi et al. Prospects for localization of gravitational wave transients by the Advanced LIGO and Advanced Virgo observatories. LIGO Document LIGO-P1200087, 2013.
- [38] J. Abadie et al. All-sky search for gravitational-wave bursts in the second joint LIGO-Virgo run. *Physical Review D*, 85:122007, 2012.
- [39] W. G. Anderson, P. R. Brady, J. D. E. Creighton, and É. É. Flanagan. Excess power statistic for detection of burst sources of gravitational radiation. *Physical Review D*, 63:042003, 2001.
- [40] J. Aasi et al. Narrow-band search of continuous gravitational-wave signals from Crab and Vela pulsars in Virgo VSR4 data. *Physical Review D*, 91:022004, 2015.

- [41] J. Aasi et al. Application of a Hough search for continuous gravitational waves on data from the fifth LIGO science run. *Classical and Quantum Gravity*, 31:085014, 2014.
- [42] J. Aasi et al. Gravitational waves from known pulsars: Results from the initial detector era. *The Astrophysical Journal*, 785:119, 2014.
- [43] J. Aasi et al. First all-sky search for continuous gravitational waves from unknown sources in binary systems. *Physical Review D*, 90:062010, 2014.
- [44] P. Jaranowski, A. Królak, and B. F. Schutz. Data analysis of gravitational-wave signals from spinning neutron stars: The signal and its detection. *Physical Review D*, 58:063001, 1998.
- [45] J. Aasi et al. Directed search for gravitational waves from Scorpius X-1 with initial LIGO data. *Physical Review D*, 91:062008, 2015.
- [46] J. Aasi et al. Improved upper limits on the stochastic gravitational-wave background from 2009–2010 LIGO and Virgo data. *Physical Review Letters*, 113:231101, 2014.
- [47] J. Abadie et al. Upper limits on a stochastic gravitational-wave background using LIGO and Virgo interferometers at 600–1000 Hz. *Physical Review D*, 85:122001, 2012.
- [48] J. Aasi et al. Searching for stochastic gravitational waves using data from the two colocated LIGO Hanford detectors. *Physical Review D*, 91:022003, 2015.
- [49] R. Schofield. Why LIGO’s range is limited by ground motion: the likely source of upconversion. LIGO Document G1000923, 2010.
- [50] R. Weiss. Various reports of experiments conducted on the Barkhausen noise research. LIGO Document T080355, 2008.
- [51] M. Ito. <http://zebu.uoregon.edu/~mito/S5/080527/080527.html>.
- [52] R. Quitzow-James. Upconversion in H1 and L1 during S6. LIGO Document G1100223, 2011.
- [53] J. McIver. LIGO burst data quality flags - S6D version 4. https://wiki.ligo.org/DetChar/S6D_DQflags_v4.
- [54] R. Quitzow-James and R. Schofield. Range prediction based on upconversion noise. http://ilog.ligo-wa.caltech.edu/ilog/pub/ilog.cgi?group=detector&date_to_view=09/10/2010&anchor_to_scroll_to=2010:09:10:19:09:22-Quitzow.

- [55] R. Quitzow-James. The likely source of low-frequency low-snr glitches. LIGO Document G1101034, 2011.
- [56] R. Quitzow-James. H1 upconversion flags for S6.
<https://wiki.ligo.org/DetChar/S6UpconversionFlags>.
- [57] S. Mereghetti. The strongest cosmic magnets: soft gamma-ray repeaters and anomalous x-ray pulsars. *The Astronomy and Astrophysics Review*, 15:225–287, 2008.
- [58] B. Abbott et al. Search for gravitational wave radiation associated with the pulsating tail of the SGR 1806 – 20 hyperflare of 27 December 2004 using LIGO. *Physical Review D*, 76:062003, 2007.
- [59] J. Abadie et al. Search for gravitational wave bursts from six magnetars. *The Astrophysical Journal Letters*, 734:L35, 2011.
- [60] R. C. Duncan. ‘Magnetars’, soft gamma repeaters & very strong magnetic fields.
<http://solomon.as.utexas.edu/magnetar.html>.
- [61] J. G. Laros et al. The soft γ -ray burst GB790107. *Nature*, 322:152–153, 1986.
- [62] R. Turolla, S. Zane, and A. L. Watts. Magnetars: the physics behind observations. a review. *Reports on Progress in Physics*, 78:116901, 2015.
- [63] I. Caballero and J. Wilms. X-ray pulsars: a review. *Memorie della Societa Astronomica Italiana*, 83:230, 2012.
- [64] S. Mereghetti. Pulsars and magnetars. *Brazilian Journal of Physics*, 43:356–368, 2013.
- [65] <http://www.physics.mcgill.ca/~pulsar/magnetar/main.html>.
- [66] K. Hurley et al. An exceptionally bright flare from SGR 1806-20 and the origins of short-duration *gamma*-ray bursts. *Nature*, 434:1098–1103, 2005.
- [67] T. E. Strohmayer and A. L. Watts. The 2004 hyperflare from SGR 1806-20: Further evidence for global torsional vibrations. *The Astrophysical Journal*, 653:593, 2006.
- [68] B. Abbott et al. Implications for the origin of GRB 070201 from LIGO observations. *The Astrophysical Journal*, 681:1419, 2008.
- [69] J. Abadie et al. Implications for the origin of GRB 051103 from LIGO observations. *The Astrophysical Journal*, 755:2, 2012.
- [70] R. C. Duncan. Global seismic oscillations in soft gamma repeaters. *The Astrophysical Journal Letters*, 498:L45, 1998.

- [71] R. C. Duncan and C. Thompson. Formation of very strongly magnetized neutron stars: Implications for gamma-ray bursts. *The Astrophysical Journal*, 392:L9–L13, 1992.
- [72] D. R. Lorimer. Binary and millisecond pulsars. *Living Reviews in Relativity*, 11(8), 2008. URL (cited on 3/4/2016): <http://www.livingreviews.org/lrr-2008-8>.
- [73] C. Thompson and R. C. Duncan. The soft gamma repeaters as very strongly magnetized neutron stars - i. radiative mechanism for outbursts. *Monthly Notices of the Royal Astronomical Society*, 275:255–300, 1995.
- [74] C. J. Horowitz and K. Kadau. Breaking strain of neutron star crust and gravitational waves. *Physical Review Letters*, 102:191102, 2009.
- [75] K. Ioka. Magnetic deformation of magnetars for the giant flares of the soft gamma-ray repeaters. *Monthly Notices of the Royal Astronomical Society*, 327:639–662, 2001.
- [76] P. D. Lasky, B. Zink, and K. D. Kokkotas. Gravitational waves and hydromagnetic instabilities in rotating magnetized neutron stars. 2012. <http://arxiv.org/abs/1203.3590>.
- [77] Y. Levin and M. van Hoven. On the excitation of f modes and torsional modes by magnetar giant flares. *Monthly Notices of the Royal Astronomical Society*, 418:659–663, 2011.
- [78] K. Glampedakis and D. I. Jones. Three evolutionary paths for magnetar oscillations. *Monthly Notices of the Royal Astronomical Society*, 439:1522–1535, 2014.
- [79] J. Aasi et al. Search for long-lived gravitational-wave transients coincident with long gamma-ray bursts. *Physical Review D*, 88:122004, 2013.
- [80] <http://www.ssl.berkeley.edu/ipn3/sgrlist.txt>.
- [81] E. Thrane et al. Long gravitational-wave transients and associated detection strategies for a network of terrestrial interferometers. *Physical Review D*, 83:083004, 2011.
- [82] E. Thrane and M. Coughlin. Searching for gravitational-wave transients with a qualitative signal model: Seedless clustering strategies. *Physical Review D*, 88:083010, 2013.
- [83] B. P. Abbott et al. All-sky search for long-duration gravitational wave transients with initial LIGO. *Physical Review D*, 93:042005, 2016.
- [84] <http://heasarc.gsfc.nasa.gov/W3Browse/fermi/fermigtrig.html>.

- [85] S. A. Olausen and V. M. Kaspi. The McGill magnetar catalog. *The Astrophysical Journal Supplement Series*, 212:6, 2014.
- [86] G. Israel et al. Discovery and monitoring of the likely IR counterpart of SGR 1806-20 during the 2004 γ -ray burst-active state. *Astronomy & Astrophysics*, 438:L1–L4, 2005.
- [87] S. P. Tendulkar et al. Proper motions and origins of SGR 1806-20 and SGR 1900+14. *The Astrophysical Journal*, 761:76, 2012.
- [88] S. Wachter et al. Precise localization of the soft gamma repeater SGR 1627-41 and the anomalous x-ray pulsar AXP 1E1841-045 with Chandra. *The Astrophysical Journal*, 615:887, 2004.
- [89] V. Testa et al. Adaptive optics, near-infrared observations of magnetars. *Astronomy & Astrophysics*, 482:607, 2008.
- [90] S. P. Tendulkar. Near IR astrometry of magnetars. In J. van Leeuwen, editor, *Proceedings IAU Symposium No. 291, Neutron Stars and Pulsars: Challenges and Opportunities after 80 years*, page 514. Cambridge University Press, 2013.
- [91] B. Sathyaprakash et al. Scientific benefits of moving one of LIGO Hanford detectors to India. LIGO Document T1200219, 2012.
- [92] <https://wiki.ligo.org/viewauth/Main/Notchlist>.
- [93] J. Abadie et al. Sensitivity achieved by the LIGO and Virgo gravitational wave detectors during LIGO’s sixth and Virgo’s second and third science runs. LIGO Document T1100338, 2013.
- [94] D. Huppenkothen et al. Quasi-periodic oscillations in short recurring bursts of the soft gamma repeater J1550-5418. *The Astrophysical Journal*, 787:128, 2014.
- [95] D. Huppenkothen, L. M. Heil, A. L. Watts, and E. Göğüş. Quasi-periodic oscillations in short recurring bursts of magnetars SGR 1806-20 and SGR 1900+14 observed with RXTE. *The Astrophysical Journal*, 795:114, 2014.
- [96] A. L. Watts. Magnetar burst library. <http://staff.fnwi.uva.nl/a.l.watts/magnetar/mb.html>.
- [97] P. N. Bhat, D. Palmer, C. Kouveliotou, and S. Barthelmy. Fermi/GBM and Swift/BAT detection of a burst from SGR 1806-20. *GCN Circular*, 10549, 2010.
- [98] A. C. Collazzi et al. The five year Fermi/GBM magnetar burst catalog. *The Astrophysical Journal Supplement Series*, 218:11, 2015.

- [99] H. S. Kumar and S. Safi-Harb. Swift study of the first soft γ -ray repeater like burst from AXP 1E 1841-045 in SNR Kes 73. *The Astrophysical Journal Letters*, 725:L191, 2010.
- [100] K. Riles. Notes on relating sine-Gaussian waveforms to astrophysical source strengths. Technical Report LIGO-T040055-00-Z, 2004.
- [101] I. S. Gradshteyn and I. M. Ryzhik. *Table of Integrals, Series, and Products*. Academic Press, 1980.
- [102] I. Bartos et al. Frequency domain calibration error budget. Technical Report LIGO-T1100071, 2011.
- [103] E. Thrane. Calibration requirements for stochastic searches in the advanced detector era. Technical Report LIGO-T1200562, 2014.